Direct Frequency Comb Spectroscopy and High-Resolution Coherent Control
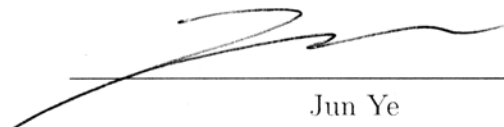
by

Matthew C. Stowe

M.S., Rensselaer Polytechnic Institute, 2001

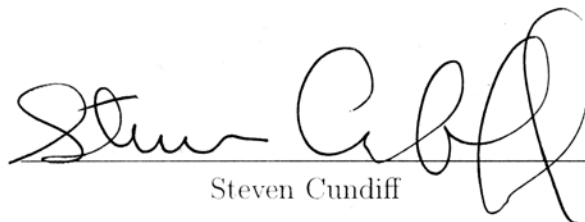B.S., Rensselaer Polytechnic Institute, 1999

A thesis submitted to the

Faculty of the Graduate School of the

University of Colorado in partial fulfillment

of the requirements for the degree of

Doctor of Philosophy

Department of Physics

2008

This thesis entitled:
Direct Frequency Comb Spectroscopy and High-Resolution Coherent Control
written by Matthew C. Stowe
has been approved for the Department of Physics

_____
Jun Ye

_____
Steven Cundiff

Date _April 28, 2008_

The final copy of this thesis has been examined by the signatories, and we find
that both the content and the form meet acceptable presentation standards of
scholarly work in the above mentioned discipline.

Stowe, Matthew C. (Ph.D., Physics)

Direct Frequency Comb Spectroscopy and High-Resolution Coherent Control

Thesis directed by Professor Adjoint Jun Ye

We present the first experiments demonstrating absolute frequency measurements of one- and two-photon transitions using direct frequency comb spectroscopy (DFCS). In particular we phase stabilized the inter-pulse period and optical phases of the pulses emitted from a mode-locked Ti:Sapphire laser, creating a broad-bandwidth optical frequency comb. By referencing the optical comb directly to the cesium microwave frequency standard, we were able to measure absolute transition frequencies over greater than a 50 nm bandwidth, utilizing the phase coherence between wavelengths spanning from 741 nm to 795 nm.

As an initial demonstration of DFCS we studied transitions from the 5S to 5P, 5D, and 7S states in ^{87}Rb. To reduce Doppler broadening the atoms were laser cooled in a magneto-optical trap. We present an overview of several systematic error sources that perturb the natural transition frequencies, magnitudes, and linewidths. These include radiation pressure from the probe beam, AC-Stark shifts, Zeeman shifts, power-broadening, and incoherent optical pumping. After careful study and suppression of these systematic error sources, we measured transition linewidths as narrow as $\sim$1.1 MHz FWHM and $\geq$10 kHz linecenter uncertainties. Our measurements of the 5S to 7S two-photon transition frequency demonstrated the ability to determine the comb mode order numbers when the initial transition frequency is not known to better than the comb mode frequency spacing.

By modifying the spectral phase of the pulses we demonstrated high-resolution coherent control. Our first coherent control experiment utilized a grating based

pulse stretcher/compressor to apply a large, $\pm 250,000$ fs^2, chirp to the pulses. We measured the two-photon transition rate as a function of linear frequency chirp. The results illustrate the differences between similar classic coherent experiments done with a single femtosecond pulse and ours conducted with multiple pulses. Furthermore, we show that it is possible to reduce the two-photon transition rate by tuning the comb such that the two-photon amplitudes from all comb mode pairs destructively interfere.

One of the unique features of DFCS is the large bandwidth over which atomic coherence may be established. We tuned the comb frequencies to not only be two-photon resonant, but also resonant with two different intermediate states separated by 7 THz. In this experiment we demonstrate the phase sensitive excitation of a closed-loop four-level system in a diamond configuration. Using a spatial light modulator based pulse shaper, we adjusted the relative phase of the two different two-photon transition pathways. We measured a sinusoidally varying two-photon transition rate as a function of the pulse shaper phase, with a fringe visibility of up to 69%. As a final example of high-resolution coherent control, we adjusted the spectral phase of the pulses to force constructive interference between the two-photon amplitudes that arise from the many thousands of mode pairs detuned from an intermediate state. This resulted in an increase of the two-photon transition rate by approximately 250%.

Dedication

To my dear wife, Lin.

Acknowledgements

I have taken a rather long and varied road from first earning my Bachelors degree in Physics at Rensselaer to finally my PhD at JILA. Along the way I have worked with many different people. Certainty my experience working with these people has contributed to my knowledge, and especially shaped my approach to physics.

In particular I'd like to thank Ralph Nightengale for his patient mentoring during my time at General Dynamics. I can only hope his phenomenal ability to break a problem down neatly and logically has rubbed off on me. Working at the Jet Propulsion Laboratory was an especially enjoyable and educational experience. In particular working in the group of Jon Dowling was always intellectually stimulating. I'd especially like to thank Dmitry Strekalov for teaching me about quantum optics, and Bill Klipstein for allowing me the opportunity to work on laser frequency stabilization. It was working on frequency stabilization of a YAG laser to Iodine with Bill that prompted my interest in joining Juns group.

Here at JILA I had the pleasure of working on a very interesting atomic physics project. Thanks to my advisor Jun Ye for providing me this opportunity and guidance. He has established a very nice laboratory environment with great people, resources, and projects. There are probably few laboratories in the world with such varied expertise. Between all the projects in Juns group, it really is possible to learn about the A, M, and O in AMO physics. I also enjoyed the many

lunch time talks, not just for the pizza, but to learn about a variety of physics experiments.

Everyone in the lab has an excellent sense of humor, which helped make it a great place to work. I'm indebted to Mike Thorpe, Thomas Schibli, and Seth Foreman for listening to me talk about my project ad nauseum, and returning the favor by telling me about theirs. I'd also like to thank Andrew Ludlow, Marty Boyd, Gretchen Cambell, Tom Loftus, Eric Hudson, Dillan Yost, Brian Sawyer, Darren Hudson, Kevin Holman, Lisheng Chen, and Thomas Zanon. I've had interesting and entertaining conversations with all of these people and learned something new from each person.

There have been several people involved with the direct frequency comb spectroscopy during my stay at JILA. First, I would like to thank Adela Marian who began the project. I'd like to thank Avi Pe'er, not only for assistance constructing a pulse shaper, but for the many helpful conversations. Thanks also to Flavio Cruz, Milan Maric, John Lawall, Ennio Arimondo, and Daniel Felinto. All of whom contributed to the success of this project during their visits to JILA.

Finally, infinite thanks to my family for their support through my ups and downs on this long road. If I think back to the things that led me to pursue science they were all provided by my family. Thanks to my brother Mike for buying a VIC-20 and getting me interested in computers. Thanks to my parents Tom and Sandi, for the many opportunities you've provided, love, understanding, patience, and support. Special thanks to my wife, Lin, for the sacrifices you made along the way for us both. You have always been there for me with your love and support. Fortunately, I love you all enough to not make you read my thesis!

Contents

Chapter

Tables

Table

Figures

Figure

Chapter 1

Introduction

In the last decade it became possible to stabilize the optical phases of the pulses from a mode-locked laser [1]. This technological achievement, together with the stabilization of the pulse repetition rate, led to the optical frequency comb. An optical frequency comb is a set of equally spaced discrete frequency modes generally spanning 1 to 100 THz with an inter-mode spacing of 100 MHz to 1 GHz. Perhaps the most revolutionary aspect of this new technology is that it provides a phase coherent link between microwave and optical frequencies [2]. Whereas previous frequency chains used for the same purpose required immense resources [3], the frequency comb is a rather simple device providing a vastly more elegant solution.

The impact of the optical frequency comb in the last decade on the field of high-precision spectroscopy has been significant [4, 5]. It has enabled the absolute frequency measurement of atomic [6] and molecular transitions [7]. In these measurements the optical comb served as a frequency ruler with which the absolute frequency of the cw-laser used for spectroscopy was determined. Similarly the comb can be used to make an optical clock. By locking a comb mode to a cw-laser, which in turn is locked to an optical transition, the repetition frequency may be counted electronically to serve as a clock. This has been demonstrated on a single trapped Hg^+ ion [8] and in molecular Iodine [9] as couple of examples.

Recently a fractional frequency uncertainty of 1 part in 10^{16} was measured using a neutral Strontium lattice clock [10]. In this measurement the optical comb served a second purpose, it allowed for a phase coherent comparison in the optical domain between the Sr transition frequency and a remote Ca clock optical transition.

We present some of the first experiments demonstrating direct frequency comb spectroscopy (DFCS). In the previously mentioned applications of optical frequency combs the atoms or molecules were excited by a cw-laser, the comb was only used to measure the absolute frequency of the cw-laser. Direct frequency comb spectroscopy uses the comb itself to excite the atomic transitions. One of the major advantages of using the comb directly to excite the atoms is the broadbandwidth of the comb spectrum. For example, in our experiments we measure one- and two-photon transitions using wavelengths from 795 nm to 741 nm from our single Ti:Sapphire laser.

Figure (1.1) shows the time- and frequency-domain pictures of direct frequency comb spectroscopy. The time-domain picture is very similar to Ramsey spectroscopy extended to multiple phase coherent pulses. For a two-level atom initially in the ground state the first pulse excites some population, which also creates an atomic coherence. Between pulses the atomic coherence acquires phase at natural frequency. Depending on the inter-pulse delay and optical phase the second pulse will either excite more population or de-excite population. In Fig. (1.1) the left panels correspond to a comb tuned on-resonance with the two-level transition, and in the right panels the comb is off-resonance. The middle panels show the excited state populations after each pulse. After the first pulse there is an equal amount of population excited regardless of the comb detuning. This is because the resonance condition is established by the interference between two or more pulses. When the comb is on-resonance the population grows quadratically versus the number of excited pulses. Strictly speaking, the quadratic scaling is

only for small excited population and without any dephasing processes. When the comb is tuned off-resonance the population excited by the first pulse is de-excited back to the ground state. Notice in the bottom panels the spectrum after two pulses is modulated sinusoidally, with peaks separated by the inter-pulse period. After more than two pulses the peaks become $sinc^2$ functions with a width inversely proportional to the total duration of the pulse train. In the limit of an infinite number of pulses the peaks are given by delta functions, this is the origin of term frequency comb. The general idea behind using multiple pulses for high-resolution spectroscopy is that the resolution is no longer limited by the spectral width of a single pulse, but rather the total coherent excitation time. In principle the total coherent excitation time is only limited by the natural lifetime of the atomic transition under study.

This idea of using multiple phase-coherent pulses for high-resolution spectroscopy was first proposed in 1976 by Hänsch [11]. In his proposal the atomic sample was to be placed inside an optical resonator in which the short pulses pass through the atoms multiple times. By tuning the resonator length the inter-pulse delay could be adjusted for resonance with a specific atomic transition. Shortly after this proposal two experimental demonstrations were conducted. In 1977 Salour and Cohen-Tannoudji conducted Doppler-free two-photon spectroscopy of the 3S to 4D transition in sodium using two phase coherent 5 ns pulses [12, 13]. Peaks in the 4D excitation were observed as a function of the inter-pulse delay, which was adjusted by an optical delay line. At the same time Teets, Eckstein, and Hänsch used multiple phase coherent pulses to measure the 3S to 5S two-photon transition [14]. In their experiment the atoms were excited by multiple passes of a single 6 ns pulses bouncing between the end mirrors of a variable length Fabry-Perot cavity. This principle was then applied in 1978 by Eckstein, Ferguson, and Hänsch to measure the 4d fine-structure splitting in sodium to be 1028 MHz [15].
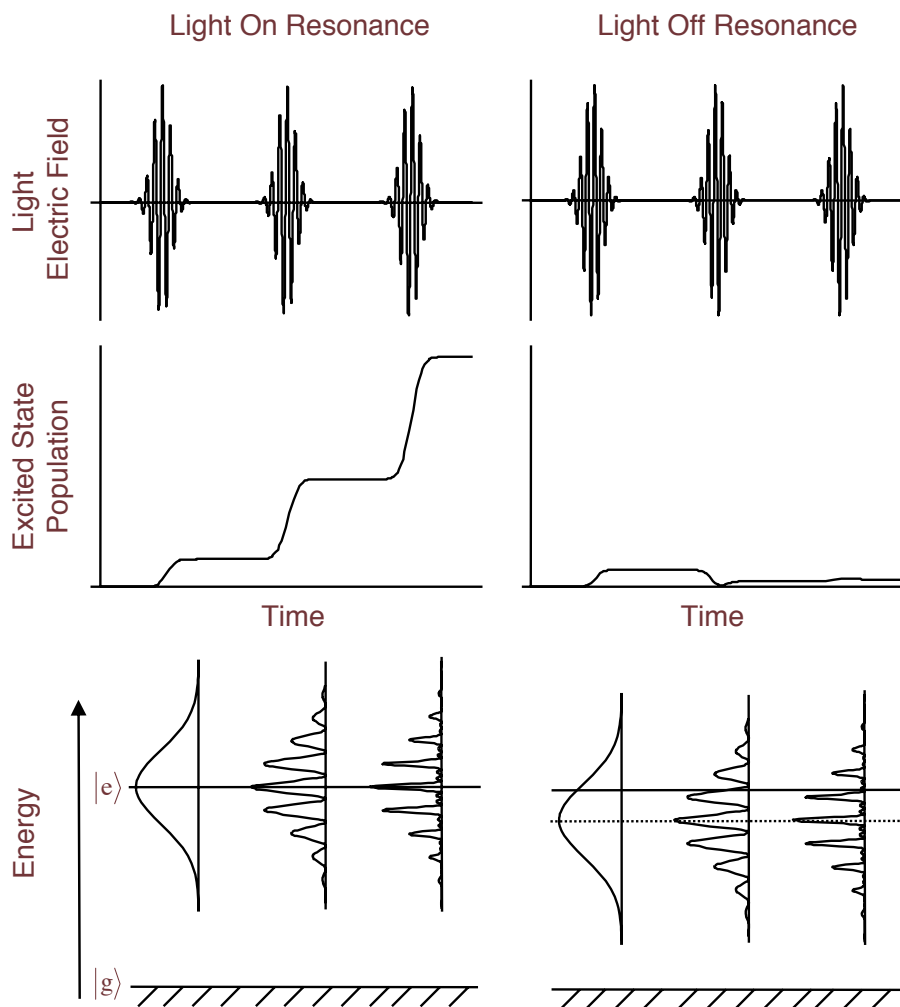
Figure 1.1: Time and frequency domain pictures of excitation of a two-level system by a series of pulses. The top two panels show the time domain picture of the pulses, the only difference between the left and right side is the optical phase of the pulses. In the case of the left panels, there is a comb mode on resonance. For the right panels there is no comb mode resonant. The middle panels show the excitation in terms of population for the two-level atom. Notice that the first pulse has the same effect for both on and off-resonance. In the case of the on-resonance pulse train the second pulse adds to the population. For the off-resonance case the second pulse de-excites the population. In the bottom panels we show the positions of the spectral peaks after 1,2,3 pulses in relation to the atomic transition frequency.

Perhaps the most closely related experiment to our own was conducted in 1996 by Snadden *et. al.* [16]. They used a cavity stabilized mode-locked Ti:Sapphire laser to conduct two-photon spectroscopy of Rb atoms in a magneto-optical trap. In particular they measured the 5S to 5D and 7S transitions and improved the estimate of the 7S hyperfine constants for both ^{86}Rb and ^{85}Rb. One very important difference between all the above experiments and our own is that they only conduct relative measurements. In other words only frequency splittings between closely spaced levels are determined. This is due to the fact that they only stabilize the frequency difference between comb modes, not the absolute frequency of the modes. We will discuss this important point further in section (2.1.1).

Figure (1.2) shows the two possible configurations for two-photon transitions. So far all of the experimental demonstrations discussed excited a ladder type configuration, Fig. (1.2)(**a**). The total two-photon transition frequency is given by the sum of two comb mode frequencies. So to determine the absolute transition frequency, the absolute frequency of each mode must be known. Due to the equal spacing of comb modes if any pair of comb modes is two photon resonant, then all modes are part of a two-photon resonant pair. In this figure we give an example where the two-photon transition is twice the frequency of the Nth comb modes. Therefore, the $N-1$ and $N+1$ modes also form a two-photon resonant pair. The second configuration is shown in (**b**), this is known as a Raman transition. In this case a photon from one mode is absorbed and a second photon is stimulated to emit into a second mode. The two-photon resonance condition is only a function of the difference in frequency between two modes. So the absolute frequency of this type of transition may be determined from only the spacing between comb modes.

In 1981 Mlynek *et. al.* conducted high-resolution spectroscopy of a Raman transition in sodium using a mode-locked laser [17]. They achieved very narrow ~ 1
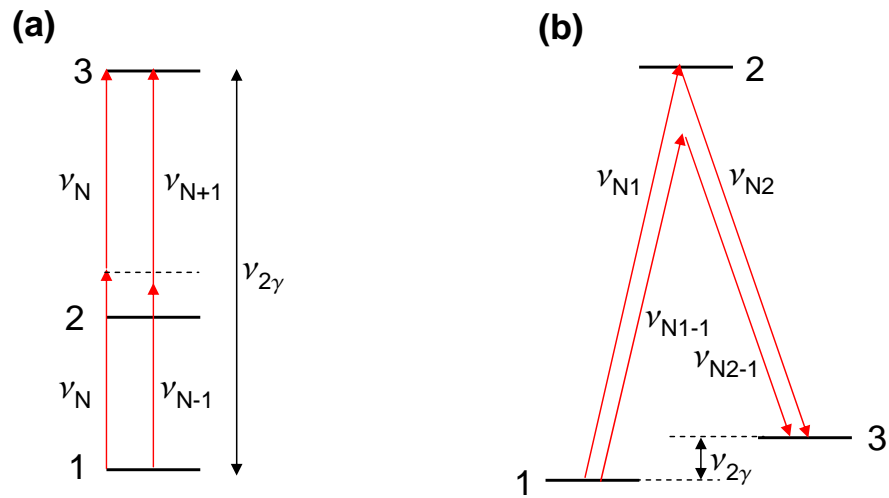
Figure 1.2: (**a**) Ladder type two-photon transitions in which the total transition frequency is the sum of two comb mode frequencies. (**b**) Raman type two-photon transition in which the total transition frequency is the difference between two comb mode frequencies. Due to the equal spacing of comb modes if any two modes are two-photon resonant then all modes in the spectrum are part of a two-photon resonant pair.

kHz FWHM two-photon transition linewidths, much narrower than the bandwidth of the laser used for excitation. This was possible due to the fact the two-photon transition frequency in a Raman transition is only a function of the inter-mode frequency spacing. A particularly interesting use of multiple pulses to excite a Raman transition was conducted in 1991 by Weiner *et. al.* [18]. They generated a phase coherent pulse train with a repetition rate of the order 1 THz. This was done by passing a single femtosecond duration pulse through a pulse shaper with a sinusoidally varying phase mask. One property of this type of phase mask is that the single femtosecond pulse becomes a short burst of weaker pulses with an inter-pulse spacing given by the period of the sinusoidal phase mask. They conducted selective excitation of Raman transitions in a molecule by adjusting the inter-pulse period.

The direct frequency comb spectroscopy that we present in this thesis represents a distinct evolution of these previous experiments. In all of the previously mentioned experiments the absolute frequency of the comb modes was not known and subject to drift. This placed a limit on the types of measurements that were possible to either Raman transitions or only measuring the difference between two ladder type transitions. We not only stabilize the inter-mode spacing of the comb but also the absolute frequency of each mode to a cesium reference. This allowed us to demonstrate high-resolution spectroscopy of ladder type two-photon transitions and measure the absolute transitions frequencies. In chapter (4) we present an explanation of several sources of systematic error and the DFCS results for both one- and -two-photon transitions.

Not only can the frequencies of the comb modes be adjusted, but the phases as well. Recall that for a two-photon transition all modes in the comb may contribute to the excitation. By adjusting the phases of the comb modes, it is possible to control the two-photon excitation rate using the interference between

multiple two-photon transition pathways. Coherent control is the ability to control the excitation of a particular quantum state by changing the phases of multiple, interfering, transition pathways. In chapter (5) we demonstrate coherent control of the excitation to a particular hyperfine level by applying linear frequency chirp to our pulses. This is an example of quantum interference between many thousands of two-photon transition amplitudes arising from different optical pathways. Due to the multi-level structure of Rb, it is also possible to have quantum interference between transitions via different intermediate states. In chapter (6) we tuned the comb to be resonant with a particular 5D hyperfine state, via two different intermediate states. This experiment utilized four resonant comb modes in a diamond type excitation configuration. By adjusting the phase of the comb modes near-resonant with one of the intermediate states we controlled the two-photon transition rate. Much like an optical interferometer we recovered a sinusoidally varying excited state population with a fringe visibility of 69%.

Chapter 2

Experimental Apparatus

In this chapter we briefly present the basic apparatus used in our experiments. The two main components are the Ti:Sapphire laser with its stabilization subsystem, and the rubidium MOT. There are many resources for more in-depth explanations of both the laser system, frequency comb stabilization, and construction of a MOT. For our coherent control experiments we provide more detailed explanations of the different pulse shaping apparatus in sections (5.2,6.1).

2.1   Ti:Sapphire Laser

The foundation for all of the experiments presented in this thesis is the optical frequency comb [19]. In this section the design and frequency stabilization of our Ti:Sapphire laser will be explained. Our optical frequency comb is generated from a mode-locked Ti:Sapphire laser. The Ti:Sapphire crystal is pumped with 5.5 Watts of 532 nm light from a Coherent Verdi laser. It uses passive mode-locking based on the nonlinear refractive index of the Ti:Sapphire crystal itself. This design is referred to as Kerr lens mode-locking (KLM) because of the role of the Kerr nonlinearity.

Mode-locking is when many thousands of the longitudinal modes of the laser are not only lasing but are in phase at some spatial location so a pulse is formed. The large gain bandwidth of the Ti:Sapphire crystal and intra-cavity

dispersion compensation allowed us to operate with a FWHM spectrum from 30 nm to 65 nm, depending on the experiment. With such a large bandwidth of longitudinal modes oscillating in-phase the peak field intensity in the laser can be very large, particularly in the crystal. Due to the Kerr effect the radial intensity profile causes a radial index gradient; much like a gradient index lens this causes focusing. However, for the low peak field of cw-lasing there is no Kerr lens effect. By offsetting the cavity focusing mirrors to account for the extra Kerr lensing the laser preferentially lases with high peak fields. Typically we operate the laser such that the power output is at least 20% higher mode-locked versus cw.

In our cavity design we use a prism pair to compensate for the dispersion of the Ti:Sapphire crystal. Although it is possible to operate in a soliton mode, we typically do not have the signature sech^2 spectrum of a soliton. Instead the spectrum usually has a tail to the IR, see for example Fig. (6.4). The typical output power is about 450 mW mode-locked at a repetition rate of $\sim$100 MHz and center wavelength of 778 nm. About 30% of the output power is used for the interferometer to stabilize the offset frequency, see subsection (2.1.3). Before detailing the laser stabilization we explain the properties and relevant parameters of an optical frequency comb.

2.1.1   Optical Frequency Comb

An optical frequency comb is simply an electric field composed of many equally spaced discrete frequencies (comb modes), typically in the visible to infrared regions of the spectrum. The beauty of the optical frequency comb is the ease with which the comb mode frequencies can be referenced to a microwave reference such as a cesium. This allows typically >100,000 separate comb modes each with an absolute optical frequency referenced to a convenient frequency standard.

The frequency spectrum of an ideal (noise and drift free) mode-locked laser

is an optical frequency comb. In practice, there are noise sources that affect the time between pulses and optical phase of the pulses on short and long time scales. So the trick to producing a useful frequency comb is to reduce or counteract the noise sources. In this section, we focus mainly on counteracting the slow noise sources, especially slow drift, with a bandwidth of up to $\sim$5 kHz. Other techniques for reducing the linewidth of the comb by locking to a stable optical laser or cavity can be found in reference [20].

Each comb mode frequency is uniquely specified by an integer mode order number and the two comb degrees of freedom [21]. Strictly speaking a comb has many more degrees of freedom when one considers the phase of each mode. In our coherent control experiments, we extend the usual picture of the comb to include the phases of each mode. However, if the spectral phase of each pulse in the pulse train remains the same, the comb mode frequencies are unaffected.

Figure (2.1) shows the electric field for a few ultrashort pulses in time domain (**a**) and the frequency spectrum corresponding to an infinite train of such pulses (**b**). Each pulse in time domain has the same envelope, shown as the dashed line, under which is the carrier electric field. Notice that the peak of the electric field for the first pulse is aligned with the peak of the envelope. However, in the second pulse the carrier electric field is slightly shifted from the envelope peak by an amount $\Delta\phi_{ceo}$. The carrier-envelope offset phase is defined for each pulse as ϕ_{ceo}, the change of this phase from pulse to pulse is $\Delta\phi_{ceo}$.

The second important parameter is the inter-pulse period labeled τ_{rep}, its inverse is the repetition frequency f_{rep}. In frequency domain the comb mode frequencies are defined by f_{rep} and f_{ceo}, the two comb degrees of freedom. The spacing between modes is f_{rep} and the offset of any mode frequency from an integer multiple of f_{rep} is f_{ceo}. In terms of the rate of change of the carrier-envelope phase $f_{ceo}=f_{rep}\Delta\phi_{ceo}/(2\pi)$. Note that for the remainder of this thesis the repetition

frequency is abbreviated to f_r, and f_{ceo} to simply f_o. With this definition of comb degrees of freedom the frequency of a comb mode with order number N is $\nu_N = N \times f_r + f_o$.

We will return to the origin of the carrier-envelope offset phase in the context of locking f_o. However, given the time domain picture of the pulses one can already understand the effect $\Delta\phi_{ceo}$ has on the frequency spectrum. Consider the interference between the first two pulses. If we take time equal to zero at the peak of the first pulse, it has a Fourier transform given by the spectral envelope with a constant zero phase. The second pulse is identical to the first except it is temporally delayed by $(1/f_r)$ and has a phase offset of $\Delta\phi_{ceo}$. Its Fourier transform has the same amplitude spectrum with a spectral phase given by,

$$\phi(\omega) = \omega \times \frac{1}{f_r} - \Delta\phi_{ceo}. \tag{2.1}$$

We chose a negative phase offset to be consistent with our definition of f_o, it does not change the frequency spectrum. The interference between these two pulses will have maxima at every frequency for which $\phi(\omega) = 2\pi N$. Solving the above equation, we get $\nu_N = N f_r + \Delta\phi_{ceo} f_r/(2\pi)$ as expected. Note that the frequency of any comb mode can be defined with either positive or negative f_o, we use both signs in our definition of comb frequencies so the magnitude is always less than $f_r/2$.

2.1.2   Repetition Rate Stabilization

The repetition rate of the laser is servoed by adjusting the cavity length directly. The output coupler is mounted on a fast ring PZT such that the beam passes through the center. Considering our laser center wavelength is about 778 nm and f_r is 100 MHz the comb order numbers N are of the order 4×10^6. So it is necessary to stabilize f_r very well because any phase noise in the repetition
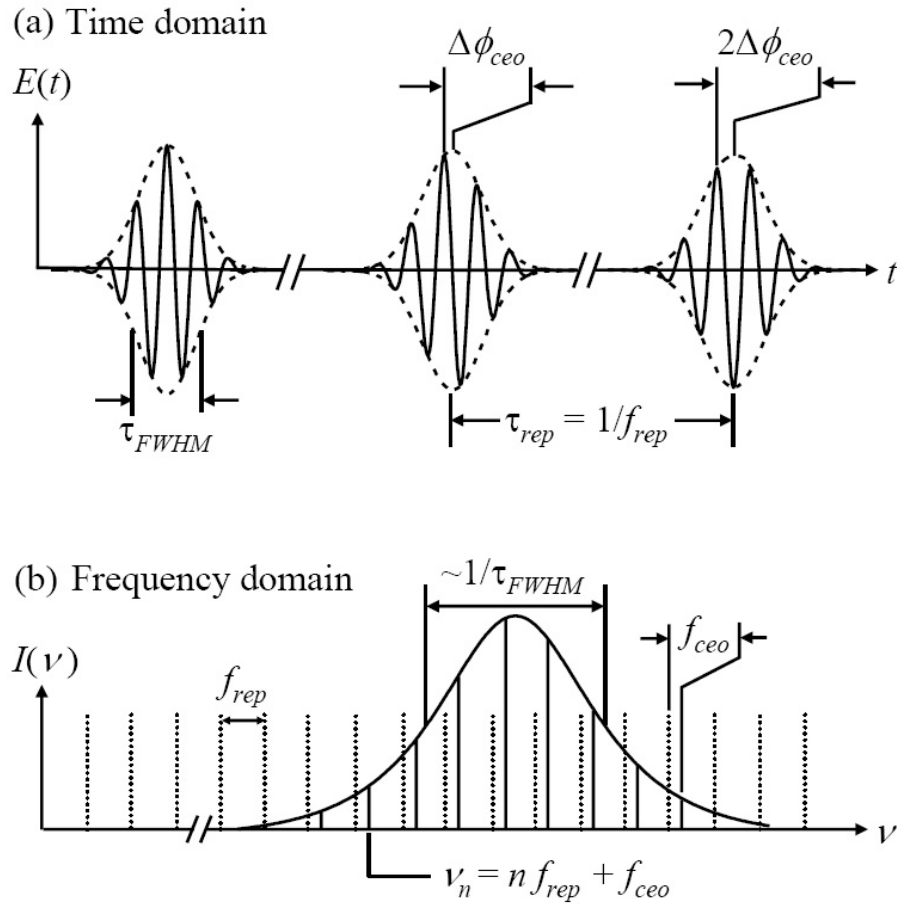
Figure 2.1: (**a**) Time domain picture of a pulse train with the relevant degrees of freedom labeled. $\Delta\phi_{ceo}$ is the phase offset of the electric field from the peak of the envelope, notice the first pulse has no offset phase. The time between pulses is τ_{rep} and is the inverse of the pulse repetition frequency f_r. (**b**) Frequency domain spectrum (amplitude only) of the comb corresponding to an infinite number of pulses. f_r sets the frequency spacing between modes and f_{ceo} is the offset frequency of every mode from an integer multiple of f_r. f_{ceo} is given by $\Delta\phi_{ceo} \times f_r/(2\pi)$ and the Nth comb mode has an optical frequency given by $N \times f_r + f_{ceo}$.

frequency is multiplied to the optical domain by N. To achieve better phase sensitivity, we lock to the 10th harmonic of f_r rather than the fundamental.

A small fraction of the output power is reflected off of a Brewster window to a fast >1 GHz photodiode. The majority of this signal is then bandpass filtered and amplified before it is mixed with the local oscillator. Some of the power is sent to a cesium referenced counter that counts the 100 MHz repetition rate for our adjustments of the comb mode absolute frequencies. Our local oscillator signal for locking f_r is primarily from the 1 GHz output from a Wenzel crystal oscillator. To allow for easy tuning of f_r the 1 GHz Wenzel signal is mixed with the signal from a direct-digital synthesizer (DDS). We only operated the frequency of the DDS at about 10 MHz or less. So for example, if we desired a f_r of 99 MHz, we locked the laser to the 990 MHz sideband produced by mixing the Wenzel with the DDS at 10 MHz. Although our typical f_r locking was done no more than ±0.5 MHz from 100 MHz. The error signal produced from mixing the measured f_r harmonic and the local oscillator was then amplified and filtered using a JILA loop-filter. The output of which was further amplified with a 1 kV PZT driver to servo the high-voltage PZT and thus change the cavity length.

Clearly this is just an overview of basic f_r locking. Reducing the laser linewidth was not of great importance for our particular spectroscopy applications. We have locked the laser directly to a Iodine stabilized NPRO:YAG laser with a short time linewidth of $\sim$5 kHz at 1 ms. However, this did not improve our measured two-photon transition linewidths. Primarily because the transition is power-broadened to just over the spectral resolution limit of our laser linewidth, see section (4.2) for a details. Tremendously better comb linewidths (<1 Hz) may be obtained by locking the laser directly in the optical regime to a cavity stabilized diode laser [22].

2.1.3   Offset Frequency Stabilization

We used a technique called self-referencing to measure the f_o of our frequency comb [23]. This technique gets its name from the fact the f_o signal is generated from the comb itself, rather than from a heterodyne beat with a separate laser. A typical implementation of self-referencing requires an octave spanning pulse spectrum. Our implementation uses an f-2f interferometer. The principle is simple, if the pulse spectrum has two colors that are spaced in frequency by one octave the long wavelength color may be doubled and mixed with the short wavelength color, producing a f_o beat note. More specifically, suppose we have two frequencies in the broadened pulse spectrum,

$$\nu_N = N \times f_r + f_o$$
$$\nu_{2N} = 2N \times f_r + f_o. \tag{2.2}$$

If we double the frequency at ν_N, the heterodyne beat frequency between the doubled light and ν_{2N} is,

$$
\begin{aligned}
2\nu_N - \nu_{2N} &= 2(N \times f_r + f_o) - (2N \times f_r + f_o) \\
&= f_o. \tag{2.3}
\end{aligned}
$$

So the trick is to generate a phase coherent pulse spectrum that spans one octave.

It was the development of dispersion modified micro-structured fiber [24, 25] that enabled the first experimental demonstrations of self-referencing [1, 26]. Micro-structure fiber, also called photonic crystal fiber, exhibits two important features for efficiently producing an octave spanning bandwidth. Micro-structure fiber gets its name from the regular pattern of air holes that extend the length of the fiber and surrounding the core, forming a photonic band gap to confine the light. By tuning the waveguide dispersion of the fiber the net dispersion can be made zero near the desired input pulse wavelength. Typically such a fiber has a

core diameter of about 1.7 μm for a zero dispersion point at 800 nm. Confining the pulse to such a small area can generate extremely large peak intensities, which due to the zero dispersion property may persist through the fiber with minimal pulse stretching. This combination of high intensity over a long interaction length allows for efficient four-wave mixing. In practice we generate the necessary octave of spectrum using 7-10 cm of fiber with about 150 mW of power.

An alternative approach to generating an octave spanning spectrum is from the Ti:Sapphire laser itself. With a careful, and perhaps lucky, set of laser optics and high intra-cavity power people have demonstrated f_o detection using the spectrum directly from the Ti:Sapphire laser [22, 27]. Another technique only requires 2/3 of an octave spectrum. The f_o beat is formed by doubling the high frequency portion of the comb and mixing it with the tripled light from the low frequency portion [28].

The design of our f-2f interferometer is based on a prism pair to separate the two wavelengths we use for our beat note, 532 nm and 1064 nm. After the output of the fiber the continuum is spectrally dispersed using two prisms. There are two retro-reflection mirrors in the dispersed beams such that the two wavelengths are reflected from different mirror. One of the mirrors is on a translation stage to compensate for the different group delays of 532 nm and 1064 nm, so that they overlap temporally. After a second pass through the prism pair the two wavelengths are combined, ideally into one spatial mode. Both wavelengths are focused through a 1 mm BBO crystal to double the 1064 nm portion of the spectrum to 532 nm. To filter out all but the desired wavelength the beam is sent through a 10 nm FWHM optical interference filter centered at 532 nm. Due to the fact the doubled 1064 nm and original 532 nm are orthogonal polarization after the BBO crystal we project the two polarizations modes onto a common axis using a polarizer. The resulting heterodyne beat frequency is then measured on

a photodiode.

The output of the photodiode is low-pass filtered at 50 MHz to attenuate the significant amount of RF power at f_r, which would saturate our amplifiers. The filtered signal is then amplified to about -5 to 0 dBm. A directional coupler is used to divert a small amount of the f_o beat to an RF spectrum analyzer to monitor the beat note. Usually we operate with no less than 35 dB signal to noise in a 100 kHz resolution bandwidth, the best we've obtained is about 55 dB above the noise floor.

Most of the f_o signal is then sent to a digital phase detector and divided down by 64. We divided down the signal from a typical f_o of 18 MHz to about $\sim$280 kHz. This was done to make phase locking easier, phase excursions from noise are reduced by 64 so it's easier to retain locking, although less sensitive. The phase stability is not as essential for f_o as it is for f_r, simply because f_o is only multiplied by unity in the comb mode frequency equation.

To understand how to servo the laser and thus control f_o we must first understand the origin of the phase, ϕ_{ce}. Recall that ϕ_{ce} is defined between the pulse envelope, which travels at the group velocity v_g, and the underlying electric field, which travels at the phase velocity v_p. In the laser cavity, the difference of v_g and v_p results in a generally nonzero $\Delta\phi_{ce}$ given by $\Delta\phi_{ce} = l_c\ \omega_c(\frac{1}{v_g} - \frac{1}{v_p})$, where l_c is the cavity round trip length and ω_c is the carrier frequency.

With this knowledge in mind it is clear that tuning the dispersion of the cavity will also change f_o. This was accomplished by tilting the end mirror of our cavity, at which point the spectrum is spatially dispersed via the intra-cavity prisms. The resulting wavelength dependent extra path length changes the group velocity. Experimentally this was done by mounting the end mirror after the intracavity prism pair on a split PZT that was driven differentially such that the mirror tilts in response to the error signal [19]. The error signal generated

by mixing the measured $f_o/64$ with a local oscillator provided by a DDS was amplified and filtered like the f_r lock. To drive the split PZT this error signal from the loop-filter was again amplified to ± 0-150 V with a PZT voltage driver. There are two outputs from the PZT voltage driver of equal and opposite voltages. So that one half of the split PZT contracts when the other expands, causing the end mirror to tilt. Alternatively, one can change the dispersion of the laser cavity via control of the pump power [29]. This has the advantage of a much larger servo bandwidth of $\sim$100 kHz.

2.2 Magneto-Optical Trap

All of our experiments were conducted on a laser cooled and trapped sample of ^{87}Rb using a magneto-optical trap (MOT). Many experiments using cold atoms are conducted with a MOT, in particular using rubidium atoms [30]. There has been a great deal of literature published on the experimental techniques and the-oretical treatments of laser cooling. A basic laboratory guide to making a MOT can be found in reference [31]. Informative references on the classical and quantum theory of Doppler cooling may be found in references [32, 33]. The scaling laws applicable to a MOT have been studied and presented in reference [34] and similarly for the dynamics of the trapped atom cloud [35].

In our experiments we used a Rb vapor cell MOT [36], as opposed to a trap loaded using an atomic beam. Experimentally this is simpler than using an atomic beam, although typically less atoms are trapped. The atoms are sourced from Rb getters, Ni-Cr alloy metal containing a salt of Rb atoms [37]. Inside the glass chamber there are three getters, each can be supplied current separately, so that when one is depleted another may be used. Typically we operate a single getter at a current of 3.5 Amps, however, in one experiment this was lowered to 2.75 Amps to reduce the amount of hot background atoms, see section (6.2).

We used grating stabilized laser diodes for the trap and repump light, with wavelengths of about ∼780 nm. Both lasers were built by Dr. Adela Marian, who started the DFCS experiments. I will not detail the design of the lasers in this section, refer to her thesis [37] for some more detail and reference [38]. Instead I will provide more of a hands on explanation of the diode laser system.

Both the lasers have two feedback mechanisms. The grating is mounted on a fast disk PZT, and the diode laser current may be servoed as well. For coarse adjustments of the laser wavelength the baseplates are cooled via Peltier TECs below room temperature, however the current control is unipolar so they may not be heated. Another coarse wavelength adjustment is the grating horizontal control, which is usually adjusted by hand, but there is a PZT as well for fine tuning. Finally for optimizing the grating feedback there is the vertical grating adjustment, also controllable via PZT.

A typical alignment procedure is as follows. Initial coarse adjustments to set the diode laser operating at the desired wavelength is done using a wavemeter and the horizontal adjustment of the grating feedback. If in the tuning of the grating the laser mode hops over the desired operating wavelength the baseplate temperature should be adjusted, tuning the cavity length. Once this is done it should be possible to tune the laser wavelength near the desired wavelength using only the grating horizontal adjustment. The laser current may need to be adjusted somewhat coarsely ± 10 mA to obtain the exact wavelength. The usual current settings are ∼75 mA for the trap laser and -65 mA for the repump. At this point the grating feedback should be optimized using the vertical grating adjustment. After careful adjustment of the vertical tilt the laser threshold current should be ∼24 mA, indicated by a clear jump in laser output power. With a voltage sweep driving the fast PZT the saturated absorption spectrum is monitored on a scope. Using both the fast PZT voltage offset and laser current we search for the sub-

Doppler features. Adjustment of the laser current is usually necessary so that the full set of hyperfine lines can be swept over without encountering a mode hop.

The trap and repump laser frequencies were stabilized using saturated absorption spectroscopy [39]. Figure (2.2) provides an example of the measured sub-Doppler transmission lines using saturated absorption spectroscopy. With a laser wavelength of about 780 nm, we measured four sets of lines from $5S_{1/2}$ to $5P_{3/2}$. In our spectrometer vapor cells there are two isotopes, ^{87}Rb and ^{85}Rb. For each isotope there are two sets of lines separated by the ground state hyperfine splitting, about 6.8 GHz for ^{87}Rb. We chose to lock our lasers to ^{87}Rb, and thus optically cool only that isotope. Each line is labeled by its hyperfine quantum number in Fig. (2.2).

Notice that there are several extra unlabeled transitions, these are referred to as cross-over transitions and they occur at the average frequency of two hyperfine transitions. This is due to the Doppler width of the atoms in the vapor cell. Basically each cross-over line corresponds to saturating a velocity group of atoms with a Doppler shift equal to half the spacing between two hyperfine levels. For example, we lock the repump laser to the F=2-F=3 cross-over transition. The hyperfine spacing between F=2 and F=3 is 156.9 MHz, so the repump laser output is 78.45 MHz detuned from either hyperfine level for atoms at rest in the lab frame.

We used a few different types of saturated absorption spectrometers over the course of our experiments. The repump laser was always frequency modulated at about 4.6 MHz via direct current modulation. So in this case both the pump and probe beams for the repump laser spectrometer are frequency modulated. For the trap laser we either used off-set locking or frequency modulated the pump beam. A side-lock was achieved simply by providing a stable voltage offset to the F=3 transition shown in Fig. (2.2). By adjusting the magnitude of the voltage offset the detuning of the trap laser from the resonance can be tuned. the drawback
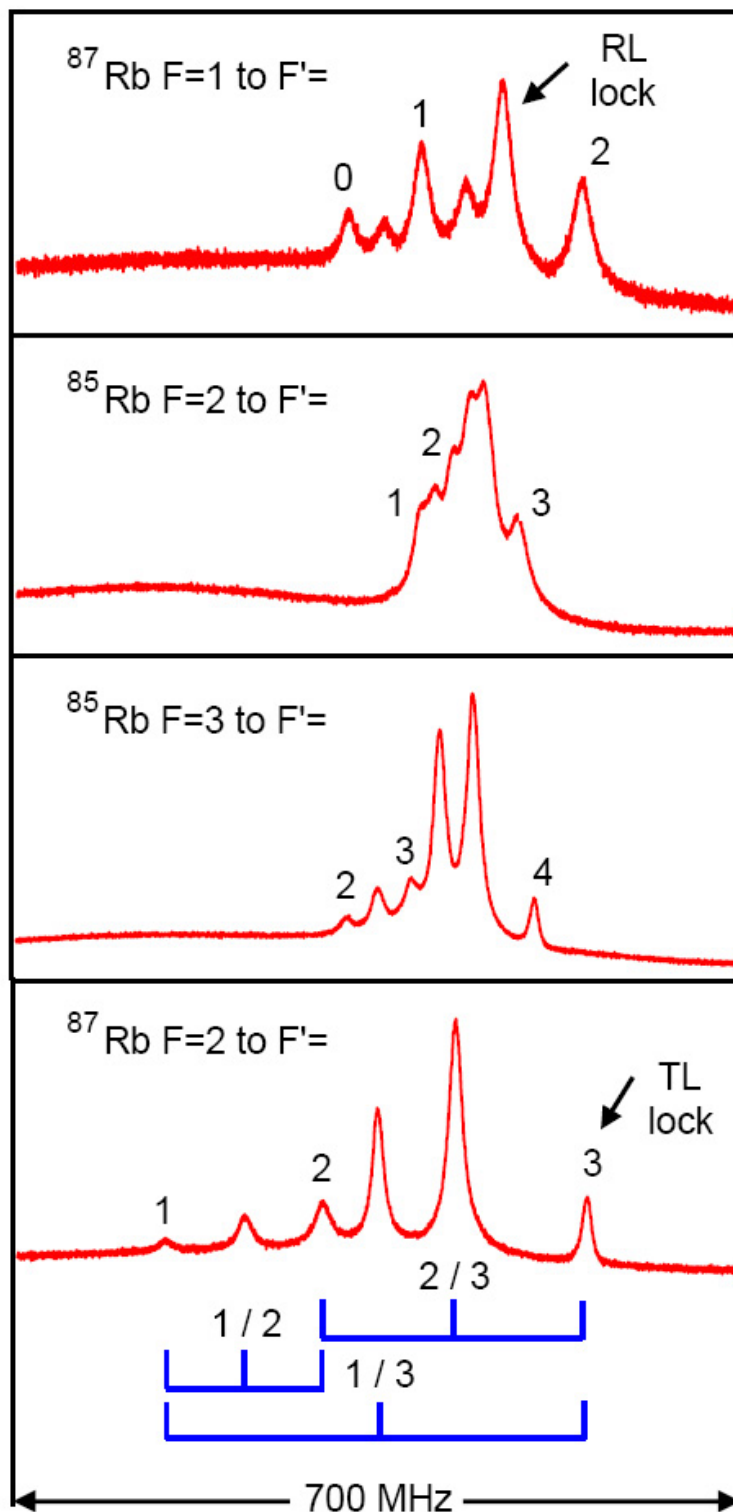
Figure 2.2: Examples of the four sets of lines measured as transmission peaks using saturated absorption spectroscopy. In our experiments we always lock to the ^{87}Rb isotope lines. The spectra correspond to the $5S_{1/2}$ to $5P_{3/2}$ hyperfine transitions, there are two sets for each isotope. Unlabeled peaks are from crossover transitions, as explained in the text. The blue bars in the bottom panel indicate the cross-over transitions and the corresponding pair of hyperfine transitions.

of this type of locking is that for a given voltage offset changes in signal size can alter the detuning. For a more stable detuning we used the frequency modulation technique, however, in this case the modulation was done using an EOM [40, 41]. In the case of FM spectroscopy the measured signal is demodulated, with the appropriate local oscillator phase, the resulting lineshape is the first derivative of those shown in Fig. (2.2). So there is a zero crossing at the peak of the transmission through the cell, this provides a more stable reference.

To act as a shutter and shift the repump laser to the resonant F=2 transition, an AOM operating at 78.45 MHz was used in the beam path of the repump laser. We used the -1 order to shift to F=2 resonance. Similarly for the trap laser we used two AOMs. The first AOM is operated with low RF power at a frequency of about 88 MHz and the +1 order beam is sent to the spectrometer. When the laser is subsequently locked to the atoms its frequency is pushed below that of the F=3 transition by 88 MHz. The light transmitted through the first AOM is then passed through a second, operated with the maximum +1 order diffraction efficiency. By setting the frequency of this AOM to 80 MHz the resulting +1 order beam is detuned 8 MHz below the F=2 to F=3 cooling transition.

In the context of each experiment we explain the specific MOT operation timings. However, in general we cooled the atoms for only about 7 ms every 10 ms using standard Doppler cooling. In our spectroscopy experiments a subsequent polarization-gradient cooling (PGC) period is used to cool the atoms further to sub-Doppler temperatures [42, 43]. With careful nulling of the magnetic field at the atom sample temperatures of 20 μK may be reached using PGC of ^{87}Rb. The procedure for nulling the field is explained in section (4.2.4). During the PGC cycle the trapping magnetic field was turned off and the trap laser was attenuated and far-detuned ($\sim$40 MHz) below the resonant F=2 to F=3 transition. There is no central trapping force in PGC, however, there is a viscous force [44]. So the

expansion of the atom cloud is slowed using the PGC cycle.

The description provided in this section is only meant to be an overview. In actual practice the characteristics of the cooling and trapping were not routinely measured, such as MOT diameters and number. Instead the alignment of the trapping beams, magnitude of the trap magnetic field, and trap laser detuning were optimized by monitoring our two-photon signal. Although for reference some of the initial MOT characterization was done with a getter current of 3.5 A, a trap laser detuning of 10 MHz, and a magnetic field current of 4.5 A. In this case the measured atom number was $\sim 5 \times 10^6$ in a diameter of ~ 0.5 mm [37].

Chapter 3

Theory

In this chapter we present two of the primary approaches used to solve for the interaction of an optical comb with a multi-level atom. The different models are best suited for understanding different aspects of our experiments. In the limit of weak excitation, we used a model based on second-order perturbation theory to calculate the two-photon transition amplitude. At higher fields we used a non-perturbative approach based on the numerical solution of the Liouville equation for the density matrix that includes optical pumping due to spontaneous decay. When the primary interest is in the population distribution of all the hyperfine states in the 5S, 5P, and 5D manifolds we used a fourth-order perturbation model based on the Liouville equation. The following two sections provide a detailed derivation of the two main models used and the particular situations for which they are most suited.

There has also been a significant amount of literature published studying different aspects of pulsed field interactions with atoms. Most of the work done consisted of theoretical studies of the interaction of a two-level atom with high intensity ultra-short pulses. In the context of an ultrashort pulse interacting with a two-level atom, effects beyond the common rotating-wave approximation have been investigated [45, 46, 47]. Deviations from the classical area theorem have been predicted for intense ultrashort optical pulses [48]. Using the exact solution

to the Liouville equation, including the counter-rotating terms, we have checked that our experimental parameters are not in the range of those studied in the cited works. Analytic expressions have been obtained for the interaction of a two-level atom with a train of phase coherent pulses as well [49, 50]. One of the reasons we present the models in this chapter is because the exact analytic solution for a simplified system of three-levels and two-modes is complicated. However, we do recommend the work of Brewer and Hahn [51] for an approximate solution and Vitanov for a complete solution [52], and also Carroll and Hioe [53].

3.1   Second-Order Perturbation Theory

In this section, we provide a derivation of the equation for the excited state amplitude in a three-level system under excitation by two-modes. The equation is derived using second-order perturbation theory with phenomenological decay included via a modified Hamiltonian. The focus is only on the derivation of the relevant equation and the approximations made in this section. We use this equation in subsequent chapters were the primary interest is in the phase of the two-photon amplitudes corresponding to many different transition pathways. One of the limitations of this approach is that it does not predict the Stark shift of the excited state or power-broadening effects. Furthermore, the equation is only applicable for the steady excited state population. We will address the modeling of these non-perturbative and transient effects in the context of the Liouville equation for the density matrix of the system in section (3.2).

The derivation we present follows most closely that found in the text by Rodney Loudon, The quantum theory of light [54]. There are two key differences, our derivation includes two time varying electric fields, and phenomenological relaxation. Our goal is to derive the value of $c_3(t)$, the excited state amplitude, valid to second order in the interaction Hamiltonian for the system shown in Fig.

(3.1).

(3.1).
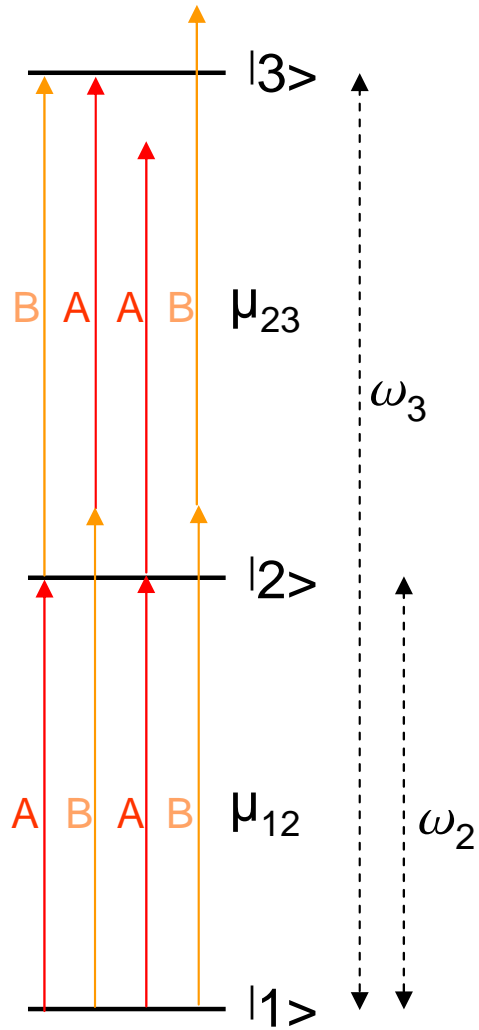
Figure 3.1: Three-level cascade system with two dipole allowed transitions excited by two modes labeled A and B. For completeness we show all four possible configurations of excitation, each gives rise to a two-photon amplitude. There is only one configuration that is resonant with the intermediate and final states, the amplitude due to this configuration is dominant.

We start with the Hamiltonian for the system modified to include relaxation,

$$\hat{H}(t) = \hat{H}_o + \hat{H}_I(t), \tag{3.1}$$

with,

$$\hat{H}_o = (\hbar\omega_2 - i\gamma_2/2)|2\rangle\langle 2| + (\hbar\omega_3 - i\gamma_3/2)|3\rangle\langle 3|$$

$$\hat{H}_I(t) = -\mu_{12}\tilde{E}(t)|2\rangle\langle 1| - \mu_{23}\tilde{E}(t)|3\rangle\langle 2| + H.C., \tag{3.2}$$

where we have defined,

$$\tilde{E}(t) = \frac{1}{2}(E_A e^{-i\omega_A t} + E_B e^{-i\omega_B t}). \tag{3.3}$$

The relaxation is given in terms of the scattering rates for each excited state such that $\gamma_i = 2\pi\Delta\nu_i$ where $\Delta\nu_i$ is the natural linewidth of state i in Hertz. Of course electric fields are real quantities, so the relevant experimental field is given by, $E(t) = \tilde{E}(t) + \tilde{E}^*(t)$, where the magnitude of the fields are E_A and E_B.

The amplitude $c_3(t)$ is given exactly by the expression,

$$\langle 3|e^{-i\hat{H}(t)/\hbar}|1\rangle, \tag{3.4}$$

for an atom initially in the ground state. We wish to find the leading order contribution to this expectation value relevant for three-level system. Within the dipole approximation the ground state is only coupled to the excited state by a two-photon interaction. Although we typically excite the 5S to 5D transition in [87]Rb we are ignoring the weak quadrupole transition. So the leading order term for two-photon absorption will be second order in the interaction Hamiltonian, and thus $\tilde{E}(t)$.

At this point we introduce a differential equation that is commonly used to find an arbitrary order solution in perturbation theory. It can be easily verified by carrying through the differentiation that,

$$e^{i\hat{H}_o t/\hbar}\hat{H}_I e^{-i\hat{H}t/\hbar} = i\hbar\frac{d}{dt}\left[e^{i\hat{H}_o t/\hbar}e^{-i\hat{H}t/\hbar}\right]. \tag{3.5}$$

To put the previous equation into a useful form we integrate both sides and after some rearranging arrive at,

$$e^{-i\hat{H}t/\hbar} = e^{-i\hat{H}_o t/\hbar}\left[e^{i\hat{H}_o t_o/\hbar}e^{-i\hat{H}t_o/\hbar} - \frac{i}{\hbar}\int_{t_o}^{t}e^{i\hat{H}_o t_1/\hbar}\hat{H}_I(t_1)e^{-i\hat{H}(t_1)t_1/\hbar}dt_1\right]. \quad (3.6)$$

If we make the interaction Hamiltonian zero at a time infinitely in the past and assume all population is initially in the ground state, we can set $t_o=-\infty$ and simplify the above equation to,

$$e^{-i\hat{H}t/\hbar} = e^{-i\hat{H}_o t/\hbar}\left[1 - \frac{i}{\hbar}\int_{-\infty}^{t}e^{i\hat{H}_o t_1/\hbar}\hat{H}_I(t_1)e^{-i\hat{H}(t_1)t_1/\hbar}dt_1\right]. \quad (3.7)$$

The LHS of the above equation is the correct expression to solve for $c_3(t)$, however, the RHS is a function of the total Hamiltonian $\hat{H}$. At this point a common trick in perturbation theory is used to arrive at an equation valid for any order of the interaction Hamiltonian. Equation (3.7) can be substituted into itself for $e^{-i\hat{H}(t_1)t_1/\hbar}$, with the variable of integration changed in the substitution to t_2. The portion of the resulting equation second order in $\hat{H}_I$ becomes,

$$e^{-i\hat{H}t/\hbar} = \frac{-e^{-i\hat{H}_o(t)/\hbar}}{\hbar^2}\int_{-\infty}^{t}e^{i\hat{H}_o t_1/\hbar}\hat{H}_I(t_1)e^{-i\hat{H}_o t_1/\hbar}dt_1\int_{-\infty}^{t_1}e^{i\hat{H}_o t_2/\hbar}\hat{H}_I(t_2)e^{-i\hat{H}_o t_2/\hbar}dt_2.$$
$$(3.8)$$

Strictly speaking, after only one substitution the last term in the above equation should be, $e^{-i\hat{H}t_2/\hbar}$. However, notice that upon one more substitution we would only retain the first term in Eq. (3.7) for an expression second order in $\hat{H}_I$. So it is valid to simply substitute $e^{-i\hat{H}_o t_2/\hbar}$ for $^{-i\hat{H}t_2/\hbar}$. The resulting equation is exactly what is needed to solve for $c_3(t)$ at second order in $\hat{H}_I$. In the derivation of this equation we dropped several terms that were either not a function of $\hat{H}_I$ or only first order in this operator. It is not an approximation to drop those terms, the expectation value for c_3 given by any operator lower than second order in $\hat{H}_I$ is zero.

Now that we have the appropriate operator equation, the expectation value can be calculated. This is done by inserting the unity operator as a sum over all

states in between the two $\hat{H}_I$ operators. In other words the equation for $c_3(t)$ is now,

$$c_3(t) = \sum_i \langle 3| \frac{-e^{-i\hat{H}_o(t)/\hbar}}{\hbar^2} \int_{-\infty}^{t} e^{i\hat{H}_o t_1/\hbar} \hat{H}_I(t_1) e^{-i\hat{H}_o t_1/\hbar} dt_1$$

$$\times \int_{-\infty}^{t_1} e^{i\hat{H}_o t_2/\hbar} |i\rangle\langle i| \hat{H}_I(t_2) e^{-i\hat{H}_o t_2/\hbar} dt_2 |1\rangle. \qquad (3.9)$$

For the purposes of this derivation we are including only one intermediate state, so the summation over $|i\rangle$ can be dropped. It is of course rather straight-forward to see that the case for multiple intermediate states is just given by the coherent sum of the amplitudes calculated using each state separately. After evaluating the operators given by Eq. (3.2) we arrive at the c-number equation,

$$c_3(t) = \frac{-\mu_{12}\mu_{23}}{\hbar^2} e^{-(i\omega_3+\gamma_3/2)t} \int_{-\infty}^{t} dt_1 \int_{-\infty}^{t_1} dt_2 e^{(i\omega_3+\gamma_3/2)t_1} e^{-(i\omega_2+\gamma_2/2)t_1}$$

$$\times e^{(i\omega_2+\gamma_2/2)t_2} \tilde{E}(t_1)\tilde{E}(t_2). \qquad (3.10)$$

Performing the integral over t_2 the c-number equation becomes,

$$c_3(t) = \frac{-\mu_{12}\mu_{23}}{2\hbar^2} e^{-(i\omega_3+\gamma_3/2)t} \int_{-\infty}^{t} dt_1 e^{(i\omega_3+\gamma_3/2)t_1} e^{-(i\omega_2+\gamma_2/2)t_1} \tilde{E}(t_1)$$

$$\times \left[\frac{E_A e^{t_1(i(\omega_2-\omega_A)+\gamma_2/2)}}{\gamma_2/2 + i(\omega_2 - \omega_A)} + \frac{E_B e^{t_1(i(\omega_2-\omega_B)+\gamma_2/2)}}{\gamma_2/2 + i(\omega_2 - \omega_B)} \right]. \qquad (3.11)$$

We can start to interpret this result by noticing the two resonant denominators. These two denominators correspond to a photon from either mode A or B exciting the electron from the ground to intermediate state. Considering these two resonant denominators are to be multiplied by $\tilde{E}(t_1)$ we can see how the four possible configurations shown in Fig. (3.1) arise. The main reason for mentioning this is so that we may simplify the expression from this point, the full expression is complicated and not necessary.

In all of our experiments we are only interested in the near-resonant or resonant two-photon amplitudes. The two configurations that correspond to two-photons absorbed from the same mode are in general not two-photon resonant

and can be safely neglected. This leaves only two configurations, absorption of a photon from mode A followed by B, and vice-versa. With this simplification the two-photon amplitude becomes,

$$c_3(t) = \frac{\mu_{12}\mu_{23}E_A E_B e^{-i\omega_3 t}}{4\hbar^2} \left[\frac{e^{i(\omega_3 - \omega_A - \omega_B)}}{(\omega_3 - \omega_A - \omega_B) - i\gamma_3/2} \right]$$
$$\times \left[\frac{1}{(\omega_2 - \omega_A) - i\gamma_2/2} + \frac{1}{(\omega_2 - \omega_B) - i\gamma_2/2} \right]. \qquad (3.12)$$

The above form of the equation is used in the subsequent chapters. Sometimes we approximate this equation further when we are considering only the ordered absorption from two modes, meaning we retain only one of the intermediate resonance denominators. The condition of two-photon resonance is met when $\omega_A + \omega_B = \omega_3$. In this case notice that the amplitude evolves phase at its natural frequency of ω_3, often this phase evolution is not of importance and therefore neglected.

This treatment based on second-order perturbation theory proved to be quite useful in understanding our experimental results. One of the great advantages of this method is that a total two-photon amplitude may be easily constructed by coherently summing the c_3 calculated for each mode combination and intermediate state [55]. Furthermore, it is the only model we use explicitly expressed in frequency domain, so it allows easy interpretation. For example, it is easy to see the phase dependence of the two-photon amplitude as a function of intermediate state detuning.

3.2   Density Matrix Treatment

A state vector in Hilbert space is useful for describing a quantum system in a coherent superposition of eigenstates. However, it is not sufficient to describe arbitrary quantum states of an ensemble, which in general may be in a mixed state.

In our experiments we must treat the population relaxation due to spontaneous emission. Suppose at some initial time an ensemble of atoms is prepared such that every atom is in an excited electronic state. After some period of time, half of the atoms will have undergone spontaneous emission and the electron in those atoms will relax to the ground state. In this example, half of the atoms are excited and half are in the ground state. The probability of finding an atom in a certain state is entirely classical, as opposed to a quantum superposition of states. If one considers the subsequent interaction of this system with a resonant pulse of area $\pi/2$ the difference becomes more clear. More generally the state of an ensemble can be have quantum superpositions and classical distributions, this is referred to as a mixed state.

To account for incoherent population distribution due to spontaneous emission, we model the state of our system using a density matrix [56]. In terms of the amplitudes of the familiar state vector based approach, the elements of the density matrix are defined as, $\rho_{ij}=\langle c_i c_j^* \rangle$. So all density matrix elements are defined as ensemble averages. Matrix elements in which $i = j$ are typically called population terms, more appropriately they correspond to the probability of the system being in state i. For a closed system, like ours, the sum of the population terms is unity.

The off-diagonal terms in which $i \neq j$ are referred to as the coherences. Coherences are in general complex numbers that range in magnitude from 0 to 0.5. In our previous example of spontaneous emission causing half of the atoms to

be in the ground state the coherence term would be zero. The maximal coherence case of 0.5 would correspond to all the atoms in the ensemble being in an equal superposition of the ground and excited states with the same phase.

The time evolution of the density matrix is governed by the Liouville equation. A convenient form of this equation including relaxation can be found in the text by R. W. Boyd, Nonlinear Optics [57]. In the remainder of this section, a brief overview of the density matrix model is introduced highlighting points relevant to our implementation.

We start with the following form of the Liouville equation,

$$\dot{\rho}_{ij} = \frac{-i}{\hbar} \sum_k [H_{ik}\rho_{kj} - \rho_{ik}H_{kj}] - \frac{1}{2} \sum_k [\Gamma_{ik}\rho_{kj} - \rho_{ik}\Gamma_{kj}] + FeedingTerms \quad (3.13)$$

where the sum is taken over all states and the relaxation operator is defined as $\Gamma_{ij} = \gamma_{ij}\delta_{ij}$. The feeding terms account for incoherent population relaxation from higher energy states to lower energy states. The only loss of population we expect in our experiment is due to ionization, which over the duration of our measurements is negligibly small [58]. Therefore with the inclusion to the feeding terms the total population remains unity.

The full set of Liouville equations for a four-level system in a diamond configuration are calculated using Eq. (3.13) and listed below. We present the four-level equations because they include the effect of branching ratios and can easily be simplified to a two- or three-level system.

Populations:

$$\dot{\rho}_{11} = \frac{iE(t)}{\hbar}\left[\mu_{12}(\rho_{21} - \rho_{12}) + \mu_{13}(\rho_{31} - \rho_{13})\right] + (\gamma_2\rho_{22} + \gamma_3\rho_{33}) \quad (3.14)$$

$$\dot{\rho}_{22} = \frac{iE(t)}{\hbar}\left[\mu_{12}(\rho_{12} - \rho_{21}) + \mu_{24}(\rho_{42} - \rho_{24})\right] - \gamma_2\rho_{22} + \gamma_{42}\rho_{44} \quad (3.15)$$

$$\dot{\rho}_{33} = \frac{iE(t)}{\hbar}\left[\mu_{12}(\rho_{13} - \rho_{31}) + \mu_{34}(\rho_{43} - \rho_{34})\right] - \gamma_3\rho_{33} + \gamma_{43}\rho_{44} \quad (3.16)$$

$$\dot{\rho}_{44} = \frac{iE(t)}{\hbar}\left[\mu_{24}(\rho_{24} - \rho_{42}) + \mu_{34}(\rho_{34} - \rho_{43})\right] - \gamma_4\rho_{44} \quad (3.17)$$

Coherences:

$$\dot{\rho}_{12} = \frac{-i}{\hbar}[\rho_{12}(E_1 - E_2) + \mu_{12}E(t)(\rho_{11} - \rho_{22})$$
$$-\mu_{13}E(t)\rho_{32} + \mu_{42}E(t)\rho_{14}] - \frac{\gamma_2}{2}\rho_{12} \quad (3.18)$$

$$\dot{\rho}_{13} = \frac{-i}{\hbar}[\rho_{13}(E_1 - E_3) + \mu_{13}E(t)(\rho_{11} - \rho_{33})$$
$$-\mu_{12}E(t)\rho_{23} + \mu_{43}E(t)\rho_{14}] - \frac{\gamma_3}{2}\rho_{13} \quad (3.19)$$

$$\dot{\rho}_{14} = \frac{-i}{\hbar}[\rho_{14}(E_1 - E_4) + E(t)(\mu_{24}\rho_{12} - \mu_{12}\rho_{24}$$
$$+\mu_{34}\rho_{13} - \mu_{13}\rho_{34})] - \frac{\gamma_4}{2}\rho_{14} \quad (3.20)$$

$$\dot{\rho}_{23} = \frac{-i}{\hbar}[\rho_{23}(E_2 - E_3) + E(t)(\mu_{13}\rho_{21} + \mu_{43}\rho_{24}$$
$$-\mu_{12}\rho_{13} - \mu_{24}\rho_{43})] - \frac{\gamma_2 + \gamma_3}{2}\rho_{23} \quad (3.21)$$

$$\dot{\rho}_{24} = \frac{-i}{\hbar}[\rho_{24}(E_2 - E_4) + E(t)\mu_{24}(\rho_{22} - \rho_{44}) + E(t)(\mu_{24}\rho_{23}$$
$$-\mu_{12}\rho_{14})] - \frac{\gamma_2 + \gamma_4}{2}\rho_{24} \quad (3.22)$$

$$\dot{\rho}_{34} = \frac{-i}{\hbar}[\rho_{34}(E_3 - E_4) + E(t)\mu_{34}(\rho_{33} - \rho_{44}) + E(t)(\mu_{24}\rho_{32}$$
$$-\mu_{31}\rho_{14})] - \frac{\gamma_3 + \gamma_4}{2}\rho_{34} \quad (3.23)$$

In the above equations, the energy of state i is E_i and the electric field $E(t)$ is the real electric field. The equations for the populations contain the previously mentioned feeding terms. For example, the equation for ρ_{11} has been modified with $+(\gamma_2\rho_{22} + \gamma_3\rho_{33})$, so all of the population relaxation from states 2 and 3

branches to the ground state. A slightly different case is for ρ_{22}, this has been modified with $+\gamma_{42}\rho_{44}$. Where γ_{42} is the decay rate of state 4 multiplied by the branching ratio to state 2. In this case, the population in state 4 relaxes to the two intermediate states, so the proper branching ratio must be included. One thing to note is that the coherences are complex quantities that obey the relation, $\rho_{12}=\rho_{21}^*$.

We use a numerical approach to solving the set of coupled ordinary differential equations. Generally a fourth-order Runge-Kutta (RK4) algorithm is sufficient. However, in the current form of the coherences they evolve phase at approximately their natural frequencies, i.e. very fast. To significantly reduce the numerical error it is necessary to make a change of variables. We use the substitution, $\rho_{ij}=\tilde{\rho}_{ij}e^{i\omega_{ji}t}$, where $\omega_{ji}=\omega_j - \omega_i$. Under this change of variables the natural phase evolution of the coherences is explicitly in the equations of motion.

Even after the change of variables for the coherences the time step setting for the RK4 algorithm must be less than an optical period. This is due to the $E(t)$ term. In some of our applications the field in time domain is generated directly by Fourier transforming the measured pulse spectrum with some arbitrary phase mask, so it is a numerically generated time series. If this is not the case and we use an analytic expression for the field, we can invoke the rotating-wave approximation (RWA). This is done by expressing the field as, $E(t) = E_oA(t)\frac{1}{2}(e^{i\omega_o t} + e^{-i\omega_o t})$ where $A(t)$ is the slowly varying envelope and ω_o is the carrier frequency of the pulse. After this substitution, terms that evolve at $\sim 2 \times \omega_o$ may be dropped from the equations of motion. Having performed a comparison between the solutions with and without the RWA, for our typical experimental conditions, the difference is entirely negligible. After invoking the RWA the time step need only be short enough in duration to sample the pulse envelope. Note that this explanation is only valid for transform limited pulses, we did not use the RWA when considering

chirped pulses.

So far we have only described the approach used to numerically solve the equations of motion during excitation by a single pulse. To extend this model for excitation by a coherent pulse train we break up the solution into a numerical part and an analytic part. Clearly this is necessary considering the time scales of the problem. The numerical solution evolves the initial density matrix from time zero to some time after one pulse, where the pulse peak field occurs at the middle of this time window. The coherences and populations may be solved for analytically between pulses because the driving field is zero. The analytic evolution of the coherences is simply free-evolution of phase at the natural frequency and decay due to spontaneous emission.

Due to the large time between pulses compared to the pulse duration, most of the incoherent population redistribution occurs between pulses. During this field-free time, the equations for the populations with $E(t){=}0$ can be analytically solved. The resulting equations are,

$$
\begin{aligned}
\rho_{11}(t) &= (1 - e^{-\gamma_2 t})\rho_{22}(0) + \frac{\gamma_2 \gamma_{42} \rho_{44}(0)}{\gamma_2 - \gamma_4}[\frac{1}{\gamma_2}(e^{-\gamma_2 t} - 1) - \frac{1}{\gamma_4}(e^{-\gamma_4 t} - 1)] \\
&+ (1 - e^{-\gamma_3 t})\rho_{33}(0) + \frac{\gamma_3 \gamma_{43} \rho_{44}(0)}{\gamma_3 - \gamma_4}[\frac{1}{\gamma_3}(e^{-\gamma_3 t} - 1) - \frac{1}{\gamma_4}(e^{-\gamma_4 t} - 1)] \\
&+ \rho_{11}(0) &\text{(3.24)}
\end{aligned}
$$

$$
\rho_{22}(t) = e^{-\gamma_2 t}\rho_{22}(0) + \frac{\gamma_{42}}{\gamma_2 - \gamma_4}\rho_{44}(0)[e^{-\gamma_4 t} - e^{-\gamma_2 t}] \tag{3.25}
$$

$$
\rho_{33}(t) = e^{-\gamma_3 t}\rho_{33}(0) + \frac{\gamma_{43}}{\gamma_3 - \gamma_4}\rho_{44}(0)[e^{-\gamma_4 t} - e^{-\gamma_3 t}] \tag{3.26}
$$

$$
\rho_{44}(t) = \rho_{44}(0)e^{-\gamma_4 t}. \tag{3.27}
$$

Where the time, t, is the inter-pulse period and all initial populations are $\rho_{ii}(0)$. The initial populations are given by the density matrix after the previous pulse. This two step process of solving for the density matrix is then simply repeated for some desired number of pulses.

For a complex level structure the direct numerical solution for the density matrix becomes increasingly difficult. The number of equations that must be solved grows as the square of the number of states. So for example in [87]Rb there are 16 hyperfine levels to consider in the full 5S to 5P to 5D interaction, this would correspond to solving 16^2=256 coupled ordinary differential equations. One alternative is referred to as the quantum Monte Carlo wavefunction approach [59]. In this type of treatment the number of equations grows linearly with the number of states. However, it is a stochastic model in which spontaneous emission events occur at random times. So to obtain high quality results representing an ensemble of atoms the model must be solved many times.

To model the full set of 16 hyperfine levels we used fourth-order perturbation theory based on the Liouville equation. I will not present the details of this model but rather some of the key approximations made in its derivation. The model was derived and implemented in C-code by one of our very talented collaborators, Dr. Daniel Felinto [60]. In this model the excitation of the full set of hyperfine levels is calculated for an impulsive pulse train to fourth-order in perturbation theory. The impulsive approximation is used when the spectral width of the exciting pulse is significantly larger than the frequency spread of the hyperfine levels [50]. Clearly a delta function (impulsive) electric field has an infinitely broad spectrum and no carrier-frequency need be defined. The only input to this model to describe the field is an area parameter, which is defined as the pulse area with a dipole moment given by, $\mu = ea_o$, where e is the electron charge and a_o is the Bohr radius. It should also be noted that the dipole moments used in the model are given by the root-sum-of-the-squares of the individual dipole moments for each magnetic sub-level transition. These are calculated directly in the software, so either polarization q=(1,0) may be used. However, note that this approximation forces all dipole moments to be positive, see section (6.2) for an example of when

this approximation breaks.

One of the useful features of this model is that it does remarkably well at predicting the population distribution due to incoherent optical pumping. In fact we used this model to normalize one of our measured lineshapes in section (4.4) to account for optical pumping effects. An introduction to this model outlining the general approach may be found in the thesis of Dr. Adela Marian [37].

Chapter 4

Direct Frequency Comb Spectroscopy

In this chapter we present our experiments demonstrating single and two-photon direct frequency comb spectroscopy (DFCS). We have conducted all of our experiments using ^{87}Rb atoms trapped and cooled prior to measurement in a MOT. This choice of atom is not only convenient from an experimental point of view for laser cooling and trapping, but also the energy level structure of the 5S, 5P, and 5D states is well known from previously published experiments. Furthermore, this is the first experiment to use an optical frequency comb to directly conduct high-resolution absolute frequency measurements, so we may easily compare our results to those obtained with traditional cw-laser spectroscopy.

The full set of hyperfine levels that may be excited by our Ti:Sapphire laser spectrum is shown in Figure (4.1). We indicate the $5S_{1/2}F{=}2$ to $5P_{3/2}F{=}3$ to $5D_{5/2}F{=}4$ transition by the red lines. This is a particularly important two-photon transition, it will be the basis for our experimental demonstration of coherent accumulation in section (4.1) and our studies of systematic errors in section (4.2). Not only does this transition have the largest dipole moments, but it is also closed, meaning all excited population returns to the $5S_{1/2}F{=}2$ ground state. The broadband nature of DFCS can be understood directly from this figure, notice the range of wavelengths span $\sim$54 nm, we in fact measure transitions over all of the indicated wavelengths. One important wavelength not indicated in this figure

corresponds to half of the 5S to 5D two-photon transition frequency at 778 nm, we generally center our spectrum at this wavelength. The $5P_{3/2}$ intermediate states are at $\sim$1 THz below the half two-photon frequency and the $5P_{1/2}$ states at $\sim$8 THz below. The lifetime of population in a 5P states is taken to be 27 ns, 241 ns for the 5D states [61], and 88 ns for the 7S states [62]. So the natural linewidths of the 5P states are 6 MHz, ten times broader than the 5D state linewidth of 660 kHz. Keep these numbers in mind as we will manipulate the comb frequencies and spectral phases around these real intermediate states.

We use the femtosecond pulses emitted by the mode-locked Ti:Sapphire laser to directly excite the one or two-photon transition we wish to study. Generally the laser is operated with a $\sim$55 nm FHWM spectrum centered at 778 nm that we approximate to be Gaussian for modeling purposes. At our repetition rate of $f_r \sim$100 MHz, this yields about 200 nW of power per comb mode near the center wavelengths used to excite the 5S to 5D transition. To probe the atoms the light is focused with a 1 m focal length lens to a beam waist radius of $\sim$160 μm, so the on-axis per mode intensity is $\sim$0.8 mW/cm^2. These numbers are only meant to provide a rough idea of the intensities we used, over the course of our experiments this has changed depending on the particular application. Figure (4.2) illustrates the basic idea of resonantly enhanced two-photon DFCS. For all of our two-photon spectroscopy experiments we set the f_r and f_o of the comb such that only two modes from the comb laser spectrum were resonant or near resonant with three states. We will discuss the effect of the many thousands of other comb mode pairs that are two-photon resonant but detuned from an intermediate state in Chapters (5) and (6). A comb mode with mode order number N_1 has an optical frequency given by $\nu_{N1} = N_1 \times f_r + f_o$ and is detuned from the closest intermediate state by δ_{SP}. Similarly a second comb mode N_2 completes the two-photon transition.
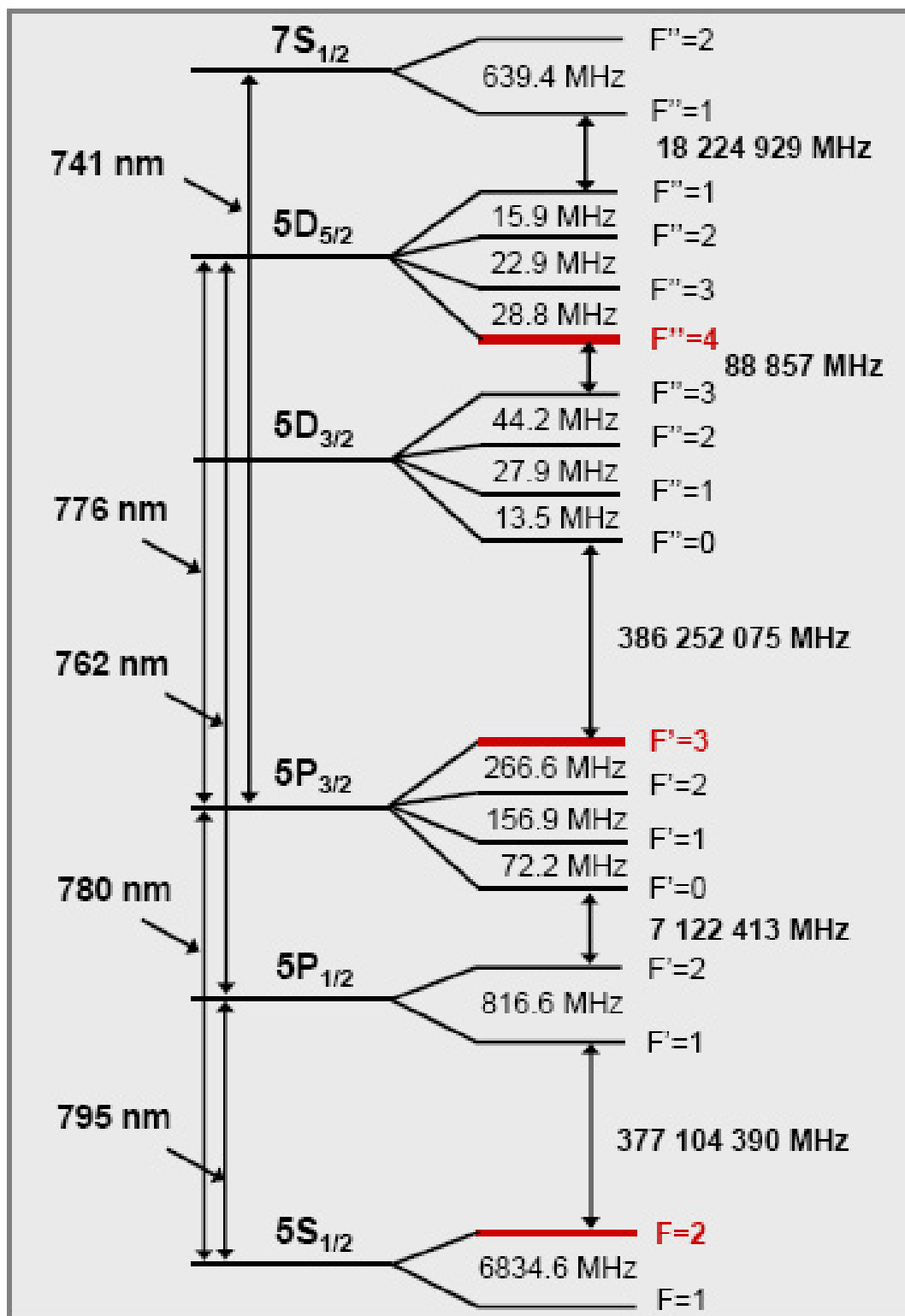
Figure 4.1: Energy level structure of all the relevant ^{87}Rb states for our experiments. The three red levels indicate the only closed transition.
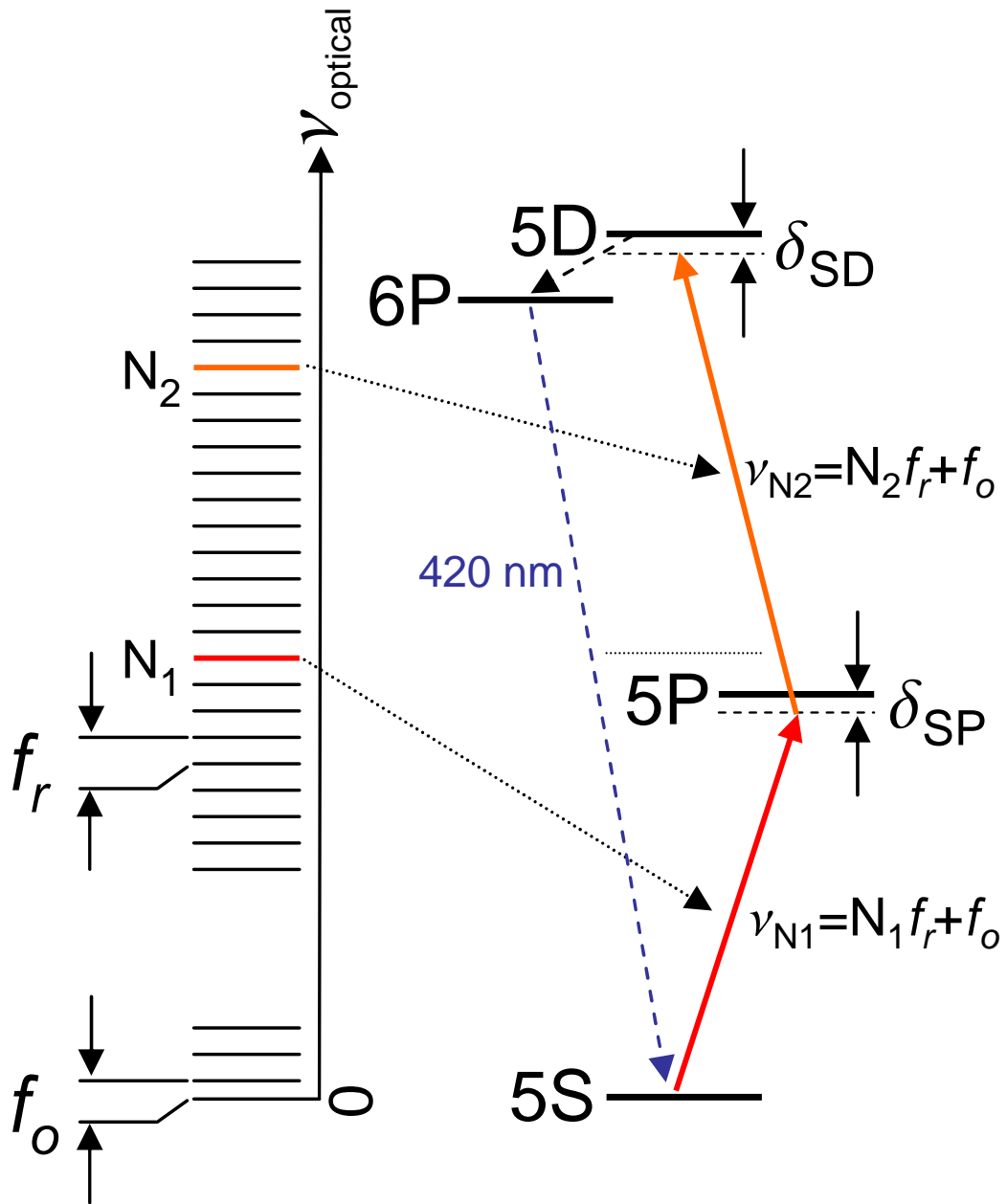
Figure 4.2: Diagram of the optical frequency comb and a near resonant three-level sub-system of ^{87}Rb. All of the DFCS experiments we present utilize only two resonant comb modes as shown in this figure. The notation and equations for the comb mode frequencies ν_{N1} and ν_{N2}, and detunings δ_{SP} and δ_{SD}, are used throughout this chapter. For two-photon spectroscopy we detect the 420 nm spontaneously emitted photons indicated by the dashed blue line from 6P to 5S.

The total two-photon optical frequency is given by,

$$\nu_{2\gamma} = (N_1 + N_2) \times f_r + 2 \times f_o. \tag{4.1}$$

The two-photon transition lineshape and frequency is measured by shifting either f_r or f_o, and thus changing the excited state detuning δ_{SD}. A convenient detection technique for our 5D and 7S two-photon spectroscopy is via the 5D to 6P to 5S cascade fluorescence at 420 nm. We count photons using a PMT sensitive to this 420 nm light to infer the 5D or 7S populations, strictly speaking we only need to know our signal is directly proportional to the excited population, the absolute value is not essential. In section (4.4) we also measure some 5S to 5P transition frequencies using single photon DFCS, we measured the 5P fluorescence directly in those experiments. The details of our data acquisition process vary depending on the specific measurement, and therefore are discussed in the context of each experiment.

4.1   Coherent Accumulation Experiment

The first experiment we discuss provides a clear demonstration of the principle of coherent accumulation to achieve high spectral resolution. Chronologically this experiment was actually conducted after the spectroscopy experiments presented later in this chapter. However, it is useful to present this work first because it sets the conceptual foundation for direct frequency comb spectroscopy. In particular, we show the quadratic scaling of the excited population versus pulse number at short times, a characteristic of fully coherent atom-light interaction. We also measure the two-photon transition linewidth versus the comb offset frequency f_o and total number of accumulated pulses to demonstrate the high-resolution we obtain with direct frequency comb spectroscopy.

We excite the $5S_{1/2}F=2$ to $5P_{3/2}F=3$ to $5D_{5/2}F=4$ resonant two-photon

transition versus a variable number of femtosecond pulses and f_o settings. This excitation is achieved by locking the Ti:Sapphire with f_r=100.41356730 MHz and f_o=18.14 MHz. For this set of comb mode frequencies, mode number 3,826,456 is resonant from $5S_{1/2}F$=2 to $5P_{3/2}F$=3, and mode number 3,847,566 is resonant from $5P_{3/2}F$=3 to $5D_{5/2}F$=4 within $\sim \pm 20$ kHz. All other allowed two-photon transitions within the $\sim$30 nm FWHM power spectrum of the laser are detuned at least 8 MHz, and at least 13 MHz for single photon transitions. Given the $\sim$6 MHz 5S to 5P transition linewidth and 660 kHz 5S to 5D linewidth the mentioned comb modes may be considered exactly resonant with the respective transitions.

This particular transition is used quite a bit in our experiments, for example all the characterization of our systematic errors is conducted on this transition. Due to the single photon transition hyperfine selection rule, ΔF=0,$\pm$1, this transition may only be excited via the $5P_{3/2}F$=3 intermediate state. More importantly $5D_{5/2}F$=4 may only decay back to $5P_{3/2}F$=3 or $6P_{3/2}F$=3, both of which may only decay to $5S_{1/2}F$=2. We refer to this as a closed transition because all the excited population relaxes back to the same ground state. All other one and two-photon transitions from this ground state may relax to the $5S_{1/2}F$=1 state, thus reducing the signal. This process of incoherent pumping to the off-resonant ground state will be discussed further in the context of our spectroscopy experiments.

A second advantage of this two-photon transition is that it has the largest dipole moments. We probe with linearly polarized Ti:Sapphire light in a nominally zero magnetic field, so we can assume to excite only Δm_F=0 transitions. This type of Δm_F=0 selection rule is often referred to as a transition with q=0. As opposed to transitions with Δm_F=$\pm$1, which correspond to q=$\pm$1. The process of zeroing the magnetic field is explained in subsection 4.2.4. There are in fact a total of 5 separate transitions from $5S_{1/2}F$=2 to $5D_{5/2}F$=4 corresponding to m_F=$\pm$2,$\pm$1,0. As mentioned in section 3 we do not model all of these states in our density

matrix, but rather treat all the magnetic sub-levels as a single hyperfine level. Each transition in this model then has an effective dipole moment given by the root-sum-of-the-squares of each individual transitions dipole moment. Implied in this approximation is that the magnetic sub-levels are uniformly populated, and the signs of the dipole moments are irrelevant, an approximation that will be lifted in section 6.2.

The timing diagram for this experiment is shown in Fig. (4.3). Similar to the rest of our experiments we form a MOT for 7 ms every 10 ms. This means the trap and repump lasers are turned on at time zero and the current to the anti-Helmholtz coils is turned on for the trapping magnetic field. At 7 ms the trap and repump lasers are turned off in ~ 3 μs via AOMs and the current to the anti-Helmholtz coils is turned off. For the next 2 ms the atoms are freely expanding as the magnetic field turns off, refer to section **??** for a description of the magnetic field systematics. During part of the remaining 1 ms the data acquisition occurs. This 1 ms window is split up into many identical probing windows each of total duration 5.09891 μs, which is equal to $\sim 512 \times \frac{1}{f_r}$. At the beginning of each ~ 5 μs sub-window the Pockels cell, used to turn on/off the Ti:Sapphire laser light to the atoms was switched on. A variable duration TTL signal generated by a SRS-535 digital delay generator was used to trigger the Pockels cell high voltage driver, and thus transmit a variable number of femtosecond pulses to the atoms, denoted as M-pulses in Fig. (4.3). To ensure that the number of transmitted pulses remains constant the SRS-535 was triggered synchronously with every 512th femtosecond pulse. This was done by digitally dividing down the f_r signal directly from the Ti:Sapphire laser so the Pockels cell trigger was always phase locked to the 512th sub-harmonic of f_r. We only conducted this experiment with total transmitted pulse numbers between 1 and 150, so the longest the Ti:Sapphire was ever on during the 5 μs sub-window is 1.5 μs. That means there is at least 3.5 μs for the
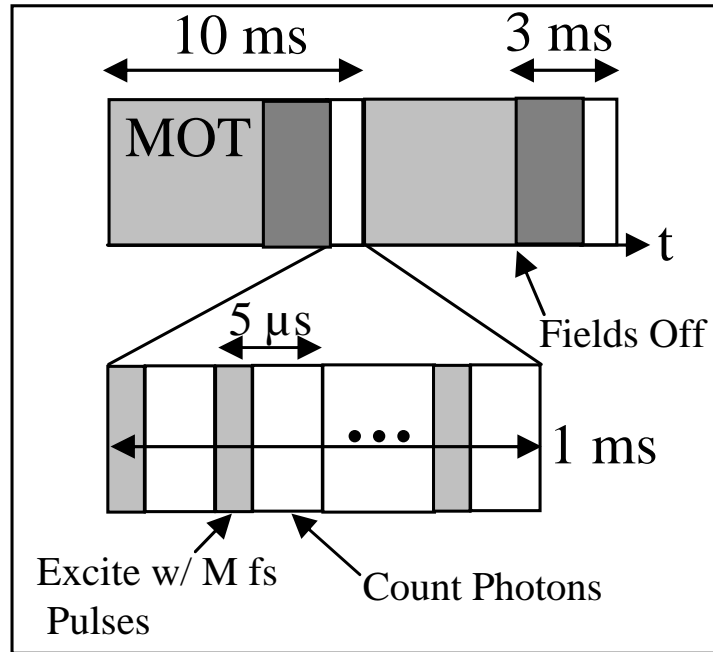
Figure 4.3: Timing diagram for the coherent accumulation experiment. The 1 ms duration measurement window is divided into separate excitation periods and photon counting periods. During the first part of the 5 μs window the atoms are excited by M femtosecond pulses transmitted via the Pockels cell. Immediately following this period of excitation the laser is switched off and photons are counted. This 5μs excitation and probing window is then repeated for 1 ms before another MOT is formed.

atoms to fully relax between sub-windows, many times the 5D and 6P excited state lifetimes.

The signal for all of our two-photon excitation experiments is obtained by counting 420 nm photons from the 6P to 5S spontaneous emission with PMT as shown in Fig. (4.2). In this experiment we used a multichannel SRS-430 photon counter to count and temporally bin our signal. It was operated with 2048 sequential bins each of duration 40 ns, with the first bin triggered 500 ns before the first Pockels cell trigger. So we measured the signal during the first 81.92 μs of the 1 ms window when the MOT optical and magnetic fields were off. Each 5.09891 μs sub-window then corresponds to about 127.5 bins. With an error of about 20 ns, or one-half a bin duration, we can then assign a time stamp to each bin modulo 5.09891 μs. Although it is possible to plot the data as a function of time, we are only interesting in the total integrated fluorescence after excitation by M pulses.

To transmit a variable number of femtosecond pulses we used a four-crystal KD*P Pockels cell model 25D manufactured by Conoptics Inc as a high speed shutter. It is designed to operate with a low half-wave voltage, which allows high repetition rate switching. The advertised rise and fall times are ~ 7.5 ns, which is just slightly less than our 10 ns inter-pulse period. Our model Pockels cell has one high quality polarizing beam splitter cube on the output, so it is necessary to ensure high quality linear polarization of the input light. There are two voltage settings on the high-voltage drivers itself, the bias voltage and maximum switched voltage. Our high-voltage drive only supplies 175 Volts peak, slightly less than the half-wave voltage. So depending on the bias voltage setting it can be operated to either optimally attenuate power, or transmit the most power. We chose to operate with the bias voltage set to minimize the transmitted power when the cell is switched off. With the switched voltage set to maximum, the transmitted

power is approximately 90% of the input power and the steady state on/off power ratio is 100:1, using the entire 30 nm FWHM spectrum.

The pulse picking performance was measured with a fast-photodiode on a suitably fast oscilloscope. While observing the photodiode voltage on the scope the trigger delay and duration to the Pockels cell was adjusted for the best single pulse transmission performance. We found that the best performance we could achieve was to actually set the trigger duration to 53 ns with a 3 ns delay, the delay is dependent on the cable lengths, so this is only relevant to our setup. With this 53 ns duration trigger one pulse was transmitted with the two adjacent pulses down by a factor of 6.5 in power, and all other pulses down by a factor of 100. It is not clear why the single pulse trigger duration is so much more than 10 ns, however, increasing the duration by $N \times 10$ ns transmits N additional pulses. Although the dispersion of the Pockels cell, including the output PBS, is approximately 6400 fs^2 we do not compensate for this chirp. The effect of this amount of chirp on the excited $5D_{5/2}F{=}4$ population is small, refer to section (5.4) for more details.

The first result we present is the measured signal scaled to the theoretical $5D_{5/2}F{=}4$ population versus pulse number. The data shown in Fig. (4.4) shows the scaled signal as squares for pulse numbers from 1 to 140. This data was taken with the probe laser split into two equal power beams using a non-polarizing beam splitter. Just prior to the beamsplitter the Ti:Sapphire light passed though a 1 m focal length lens. These two probe beams were then counter-propagated through the Rb atoms with careful attention to overlapping the beams spatially, although not necessarily temporally overlapping in the atom cloud. Figure (4.4) shows two theoretical predictions corresponding to the experimental peak electric field strength of $E_o \sim 10^7$ V/m (solid line), and asymptotically low power $E_o \lll 10^7$ V/m (dashed line). Where E_o corresponds to the peak electric field strength
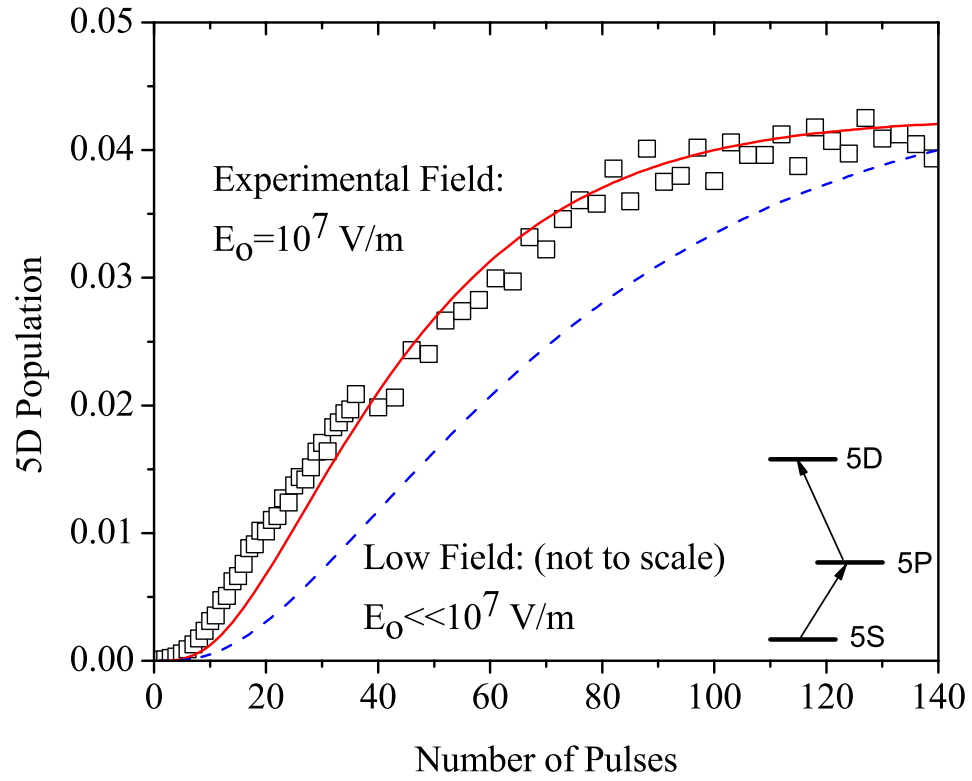
Figure 4.4: Measured signal (squares), scaled to theoretical 5D population (solid line), versus pulse number. Asymptotically low power signal (not to scale) versus pulses is shown as the dashed line.

assuming a transform limited Gaussian pulse. From this data we can already see the 5D population reaches steady state at the experimental electric field strength of 10^7 V/m sooner than for asymptotically low power. After approximately 80 accumulated pulses the mean 5D population is constant, this saturation is the time domain signature of power broadening. Figure (4.5) shows the first 15 pulses of this data set to illustrate the scaling law versus pulse number at times short compared to the 5S-5D coherence time of $\sim$480 ns. In this figure the solid line is not theory but a fit to a function of the form $c_1 M^2$, where M is the pulse number, the purpose of this fit is to illustrate the quadratic scaling law.

For a two-level system driven on resonance the population exhibits the familiar process of Rabi flopping in the absence of any decoherence. We define the accumulated pulse area from time t=0 to t=t' to be,

$$A(t') = \frac{\mu}{\hbar} \int_0^{t'} E_o(t) dt \tag{4.2}$$

where μ is the relevant dipole moment and $E_o(t)$ field envelope magnitude. With this definition of the pulse area the excited population varies as $\sin(\frac{A(t')}{2})^2$, for example, a pulse area of $A(t') = \pi$ inverts the population. If we extend this definition of pulse area to include multiple phase coherent pulses, the total accumulated pulse area after M pulses is simply $M \times A(t_{pulse})$, where $A(t_{pulse})$ is the total area of a single pulse. So for small total accumulated pulse area, $M \times A(t_{pulse}) \ll \pi$, the dependence of the excited population on pulse number goes as M^2. This analogy holds true for two-photon excitation as well in the case of intermediate and final state resonance. The population in the $5D_{5/2}F=4$ state is proportional to M^2, however, the exact dependence is more complicated than in the two-level case so we don't have an analytic expression. We have checked this scaling law in the case of weak excitation of $5D_{5/2}F=4$ driven by a series of phase coherent pulses using our three-level density matrix model. So by considering the familiar case
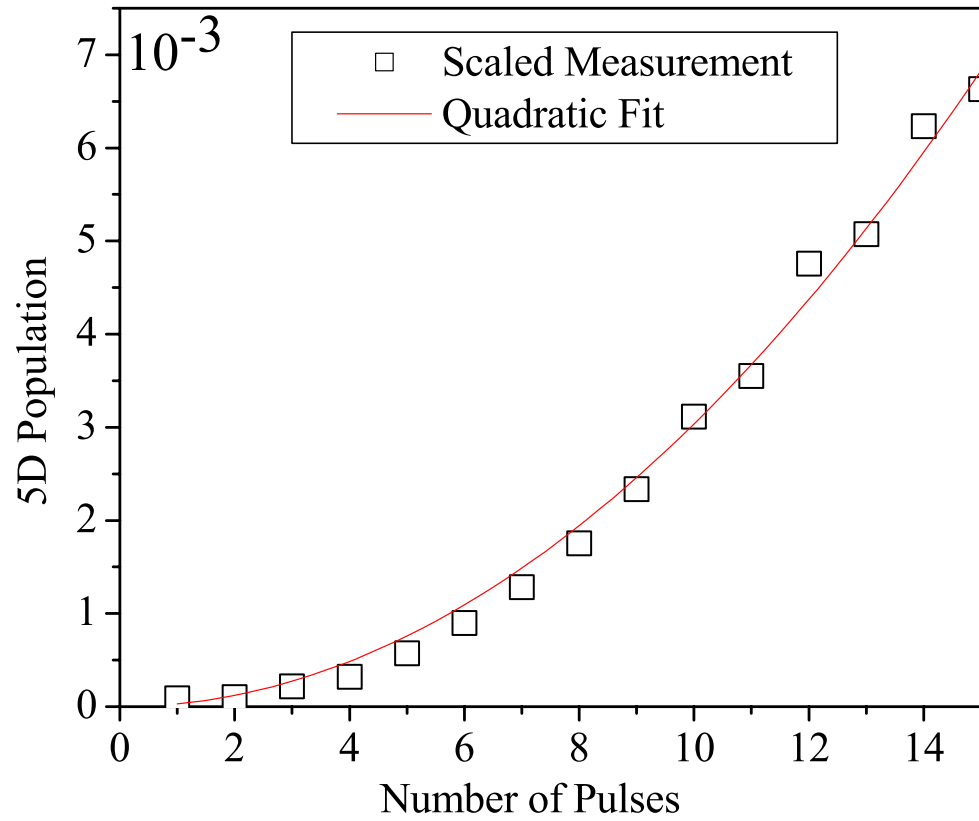
Figure 4.5: Measured signal (squares) versus number of accumulated pulses for short times, the data is fit to a function of the form $C_1 M^2$ where M is the pulse number.

of a coherently driven two-level atom we can understand the quadratic scaling of the excited population for accumulated pulse numbers < 15 in Fig. (4.5). One interesting conclusion from this analysis and experimental result is for a given laser power a higher repetition rate comb excites more 5D population. In frequency domain this can be understood by considering a higher repetition rate comb has more power per comb mode. Our results in section (5.4) demonstrate that this quadratic scaling law holds true for chirped pulse excitation as well.

The second part of this experiment is to demonstrate high-resolution spectroscopy. In general there are two ways to change the detuning from two-photon resonance, either by shifting f_r or f_o. Figure (4.6) shows the signal scaled to the theoretically calculated $5D_{5/2}F=4$ population versus two-photon detuning for 4 sets of accumulated pulse number. In this result we scanned f_o, due to the fact it is a two photon transition, the detuning is given by

$$\delta_{2\gamma} = 2 \times (18.14 - f_o) \quad [MHz] \tag{4.3}$$

where f_o=18.14 MHz is the resonance condition. The measured lineshapes after 10, 15, 20 total accumulated pulses is shown with the corresponding $5D_{5/2}F=4$ population on the left y-axis, similarly the population after 80 pulses is on the right axis.

This result simply provides a clear picture of how the measured lineshape narrows as more pulses are used for excitation, or in other words how we obtain high-resolution from coherent pulse accumulation. There are a few things that in general can limit the linewidth of the measured transition in our experiments. For the results presented in Fig. (4.6) the linewidth is limited by probing time, or the number of pulses, for less than ~80 pulses. After ~80 pulses have been used to excite the transition the linewidth no longer continues to decrease due to power-broadening, recall that the population after 80 pulses was in steady state.
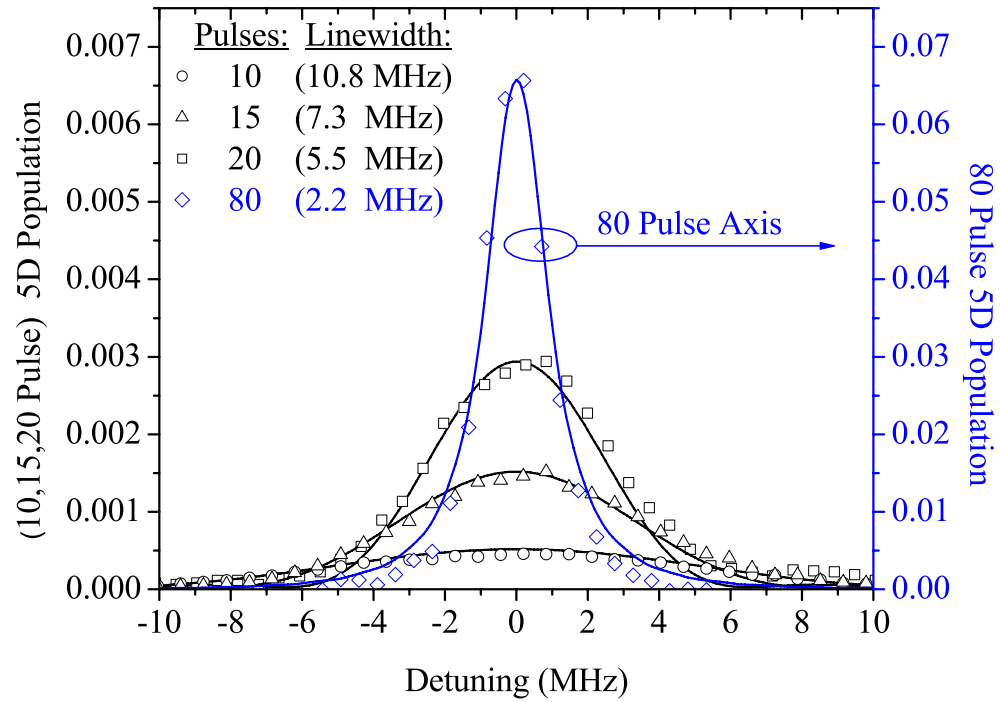
Figure 4.6: Measured signal (squares), scaled to theoretical 5D population (solid line), versus f_o and for several values of accumulated pulse number.

Traditionally most high resolution spectroscopy has been done with cw-lasers. A line-broadening phenomena common to cw-laser spectroscopy is transit time limiting. This occurs when the duration of excitation of the atom is limited, usually by motion through the probe beam, to be less than either the electronic or laser dephasing times. In this sense excitation by only 10, 15, 20 pulses is analogous to transit time broadening. We chose to operate with the most laser power possible for this experiment to increase the signal, particularly for the measurements taken with very few pulses. In principle the resolution obtainable with direct frequency comb spectroscopy is only limited by the natural linewidth of the excited state. Experimentally the narrowest linewidth we have achieved was ~1.1 MHz FWHM, most likely limited by power-broadening.

4.2   Systematic Effects

In this section we discuss several of the most important sources of error that may either broaden or shift the lineshapes we measure using DFCS. In general we are not interested in determining the natural linewidths of the transitions we measure so the main reason to reduce line-broadening is to improve our line-center estimates. In particular, we will discuss the effect of radiation pressure on the atoms due to the probe laser, Zeeman shifting of the ground and exited states, probe laser linewidth, and Stark shifts. Power-broadening of the excited state linewidth was already discussed briefly in section (4.1). After careful minimization of the systematic effects presented in this section we generally measured power-broadened linewidths ranging from 1.1 MHz to 2.5 MHz in our spectroscopy results.

Before addressing the previously mentioned systematics, it is worth estimating the effect of the atomic cloud temperature on the linewidths. As discussed previously we conduct all of our experiments on a sample of ^{87}Rb laser cooled in

a MOT. All of the one and two-photon spectroscopy results we present were conducted after an additional $\sim$ ms polarization gradient cooling (PGC) stage while the trapping magnetic field was turning off. Although we did not measure the atomic cloud temperature directly, we can estimate the range of Doppler widths we expect for temperatures from 20 μK for excellent PGC, to 100 μK without PGC. In the range of these temperatures, we expect the Doppler widths for single photon transitions from 5S to 5P to be $\sim$130 to 300 kHz, much less than the 6 MHz transition linewidth. The Doppler width for the two-photon transitions is approximated to be twice that of the single photon case, $\sim$260 to 600 kHz. A reasonable approximation considering the resonant wavelengths are typically very similar. So we can expect that the 660 kHz natural linewidth of the 5S to 5D transition will be slightly Doppler broadened, however even at 100 μK the Doppler width is still less than the typical power-broadened linewidths we measure.

A common misconception people have about the effect of the intermediate state on the two-photon transition is that it may broaden the measured linewidth. In our experiments we generally set the comb frequencies such that a mode is single photon resonant with an intermediate state, and another resonant from that state to the excited state. As mentioned previously, we measure the two-photon transition linewidth by scanning either f_r or f_o, which shifts not only the excited state detuning but the intermediate state detuning as well. So if we scan the excited state detuning by ± 4 MHz using f_o, we recover most of the $\sim$2 MHz FWHM lineshape, and the intermediate state detuning only changes by ± 2 MHz. Considering the intermediate state natural linewidth of 6 MHz the detuning is not very significant. The effect of changing the intermediate state detuning as we scan the two-photon lineshape does not broaden the line, but it does in fact change the lineshape slightly. For example, using Eq. (3.12) to estimate this effect, the deviation from a Lorentzian lineshape between ± 2 MHz detuning is at most 5%,

qualitatively the effect is to make the tails of the lineshape approach zero faster than that of a Lorentzian lineshape.

4.2.1   Laser Linewidth

To conduct high-resolution DFCS it is important to ensure the linewidth of each comb mode is sufficiently narrow. Recall that the order numbers of the resonant modes, corresponding to ~ 780 nm, are of order 4×10^6. So any noise in f_r is multiplied up in the optical domain by this factor. We typically locked the comb f_r by phase stabilizing the 10th harmonic of f_r to the Wenzel low phase noise crystal oscillator, as described in section (2.1). With the comb f_r locked to the Wenzel oscillator and f_o locked via self-referencing we can measure the linewidth of an individual comb mode by forming a beat note with a stable cw-laser.

We have done this measurement using two different cw-lasers, an Iodine stabilized NPRO-YAG laser, which typically has a narrow 5 kHz linewidth at 1 ms [9]. And also a cavity stabilized diode laser with a significantly narrower linewidth [63]. In both cases the linewidth of the cw-lasers is much less than that of the comb over our measurement time. Figure (4.7) shows a typical beat signal between the comb and the cavity stabilized diode laser at 698 nm. Using a Lorentzian fit to the data we extract a 638 kHz FWHM comb linewidth measured at 698 nm. Similarly when we measured the beat between the comb and the NPRO-YAG at 1064 nm, we recovered a 330 kHz FWHM linewidth. In both of these measurements the required wavelength to form a beat with the cw-lasers was generated from supercontinuum generation in a highly nonlinear fiber; we are assuming negligible extra phase noise in this process.

It has been shown that the spacing between comb modes is extremely uniform [64]. In other words the frequency noise of different comb modes is highly correlated and is generally due to noise in f_o and f_r. Neglecting the smaller f_o

noise we can attribute the measured linewidths primarily to fluctuations of f_r and estimate the comb linewidth at 780 nm. Under these approximations the comb linewidth at 780 nm is between 570 kHz, using the 698 nm measurement, and 450 kHz using the 1064 nm measurement. One thing to note is that these measurements were conducted about two years apart so the difference in estimated linewidths may be attributed to differences in the f_r lock. Although the linewidth of our comb modes is relatively wide, it does not present a problem due to the fact we conduct most of our experiments with sufficient intensity to power broaden the two-photon transition linewidth to about ∼1.5-2.2 MHz.

4.2.2   Radiation Pressure

One of the most important systematic effects in our experiments is due to radiation pressure exerted on the atoms by the probe beam itself. The radiation pressure we consider in this section is due to the momentum imparted on an atom from incoherent photon scattering out of the probe laser mode. Coherent photon scattering, responsible for the dipole force, gives rise to a much weaker force that we ignore in this section. When an atom is excited it receives a momentum kick in the direction of the probe beam propagation, however, the spontaneously emitted photon imparts a momentum kick of the same magnitude but with a random direction. The net effect on an ensemble of atoms probed from one direction is primarily to increase the mean velocity in the direction of the probe. Due to the random directions of emissions and number of photons scattered after some period of time, the width of the velocity distribution of the atom ensemble also increases. These two effects lead to a Doppler shift of the measured center frequency of a transition and an increased linewidth due to Doppler broadening.

In the case of our two-photon transition measurements with a resonant intermediate state this effect is quite significant. Recall that the linewidths for the
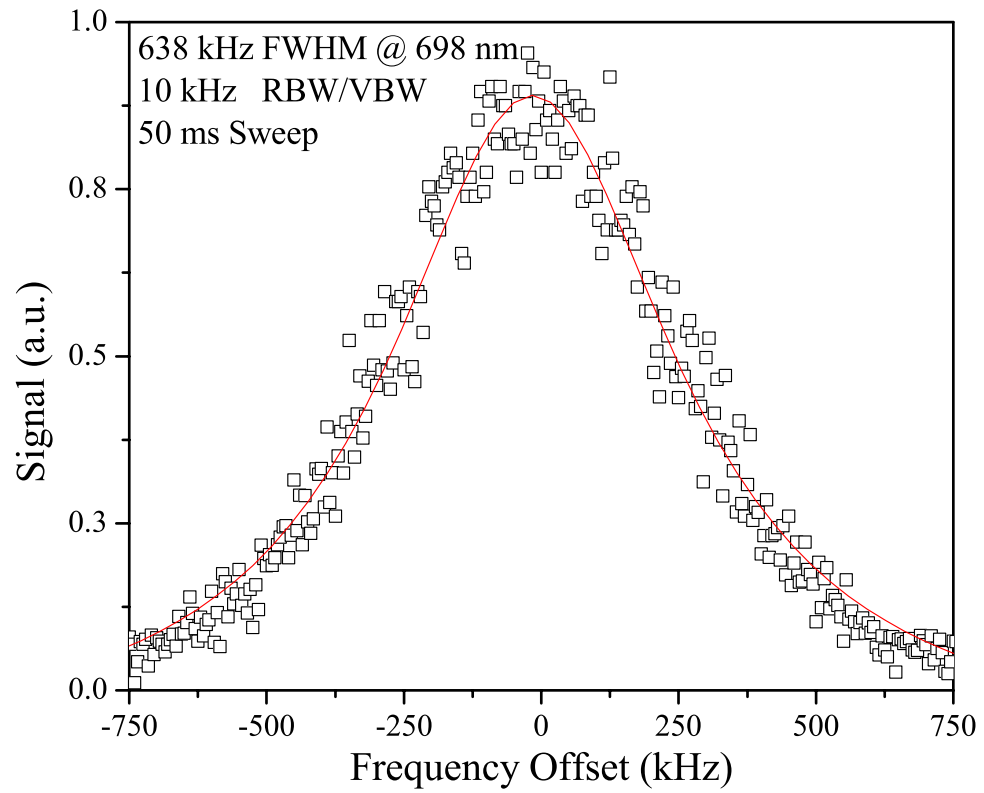
Figure 4.7: Comb linewidth measured by the beat frequency linewidth between a comb mode and a cavity stabilized diode laser, solid line is a Lorentzian fit with 638 kHz FWHM.

5P states is 6 MHz, ten times larger than for the 5D states. Furthermore, the two-photon excitation probability ρ_{5D} arises at second order in perturbation theory and is in general much less than the one-photon excitation probability ρ_{5P}. The total incoherent scattering rate from a particular state is,

$$\gamma_i' = 2\pi\Delta\nu_i\rho_{ii} \tag{4.4}$$

where $\Delta\nu_i$ is the linewidth of state i and ρ_{ii} is the population. So the incoherent scattering rate from the resonant 5P state is much larger than the 5D, typically by a factor of at least 100. In other words for every 420 nm photon emitted from the 5D-6P-5S radiative cascade there are on average at least 100 photons scattered from the resonant intermediate 5P state. On average for every photon scattered from 5P at 780 nm the atom obtains a recoil velocity kick of,

$$\vec{v}_r = \frac{\hbar\vec{k}}{m} \tag{4.5}$$

where m is the ^{87}Rb mass, and $\vec{k}$ is the probe laser wavevector. Substituting for the laser wavevector and atomic mass we find the recoil velocity is about 5.88 mm/s, which causes a Doppler shift at 780 nm of 7.54 kHz. Clearly the accumulated Doppler shift from many photon recoils can amount to a significant shift of the measured linecenter frequencies.

To better understand and develop a model of the radiation pressure effects we studied the $5S_{1/2}F=2$ to $5P_{3/2}F=3$ to $5D_{5/2}F=4$ transition using excitation from only one direction. As mentioned previously the large dipole moments and closed nature of this transition makes it the best choice for studying systematic effects. The experiment is simply to measure the signal at 420 nm versus excitation time under three different initial detuning conditions. Figure (4.8) shows the relevant three-level system and the two comb modes nearest to resonance. The detuning of this comb mode pair from $5P_{3/2}F=3$ is denoted as δ_{SP}. For this
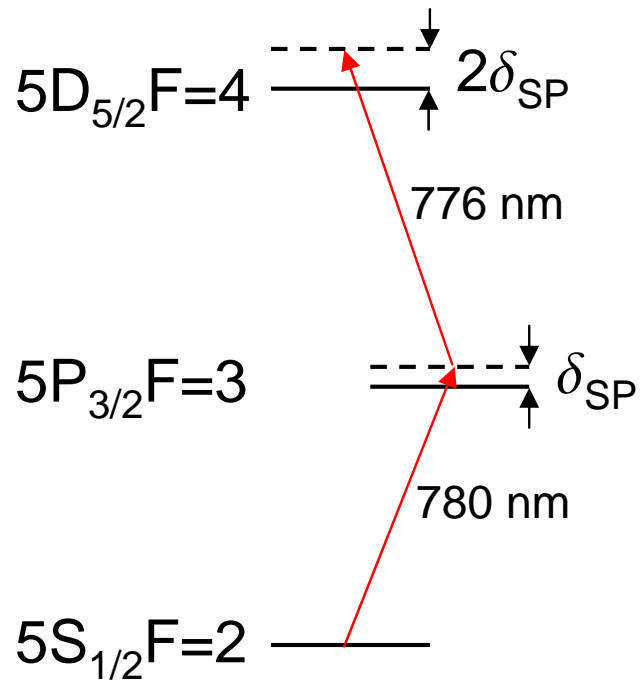
Figure 4.8: Energy level diagram of the relevant three-level system for studying the radiation pressure. All detunings are relative to atoms stationary in the lab frame, radiation pressure will Doppler shift the light and therefore change the detunings.

experiment we initially set f_r and f_o such that $\delta_{SP}=0$ and the comb modes are resonant. By shifting f_o by either 1 MHz or 2 MHz we make the detuning from $5D_{5/2}F=4$ either 2 MHz or 4 MHz. When we conducted this experiment we did not have the Pockels cell as a shutter. Instead the Ti:Sapphire was switched on or off using a liquid crystal shutter with a much slower, ~ 30 μs, response time. Our measurement results are shown in Fig. (4.9) as symbols, together with the theoretical predictions of our model (solid lines). The three detuning cases correspond to the initial detunings from $5P_{3/2}F=3$, or more specifically to atoms at rest in the lab frame. Note that a positive detuning corresponds to blue detuning from intermediate resonance, so the atoms will eventually be Doppler shifted into resonance.

Considering we only measure the 420 nm fluorescence from the two-photon transition, it can be thought of as a probe for the mean velocity of the atoms. When the Doppler shift is equal to $\sim 2\delta_{SP}$ the $5D_{5/2}F=4$ state is resonant and starts to fluoresce. With this in mind the characteristic shapes of the results in Fig. (4.9) may be interpreted. For an initial detuning $\delta_{SP}=0$ the LC shutter slowly turns on for the first ~ 40 μs, when the shutter is completely on the signal is a maximum. The signal then rapidly decays over ~ 150 μs as the mean velocity of the atom ensemble Doppler shifts atoms off of two-photon resonance. Similarly for the blue detuned cases, initially the signal is essentially zero due to the $5D_{5/2}F=4$ detuning, however at later times the atoms are Doppler shifted onto two-photon resonance. The two initially detuned cases show significantly broader peaks than the $\delta_{SP}=0$ case due to the fact the atoms have undergone more heating.

To go beyond simply a qualitative understanding of the radiation pressure we developed a more comprehensive model. We have already discussed two of the key pieces to our model, the incoherent scattering rate Eq.(4.4), and the single photon recoil velocity Eq.(4.5). Due to the fact the radiation pressure is almost

entirely from $5P_{3/2}F=3$ incoherent scattering, and the time scale for accumulating a significant Doppler shift is much larger than the 5P lifetime, we only need to consider the steady state value of the $5P_{3/2}F=3$ population. Solving for the density matrix of a two-level system using the Optical Bloch Equations in steady state [30], we calculate the scattering rate to be,

$$\gamma'_{5P} = \frac{\gamma}{2}\frac{s_o}{1 + s_o + (\frac{2(\delta+\omega_D)}{\gamma})^2} \qquad (4.6)$$

where s_o is the on-resonance saturation parameter, δ is the angular frequency detuning of the laser, ω_D is the Doppler shift, and $\gamma=2\pi\Delta\nu_{5P}$. The on-resonance saturation parameter can be written in terms of the saturation intensity, I_s, as $s_o=\frac{I}{I_s}$ where $I_s=2.5$ mW/cm^2 for linearly polarized light. The detuning δ is the detuning for an atom at rest in the lab frame. It is defined as, $\delta=\omega_l-\omega_a$, where the subscripts refer to the laser and atom angular frequencies. The Doppler shift is given by the familiar formula, $\omega_D=-\vec{k}\cdot\vec{v}$, where $\vec{k}$ is the probe beam wavevector at 780 nm.

Ultimately we are interested in deriving an equation for the velocity of an atom versus time given some initial conditions. Recall that the change in velocity of an atom after one incoherent photon scattering event is $\frac{\hbar\vec{k}}{m}$. Equation (4.6) gives us the rate at which the photons are scattered. So the differential equation for the rate change of velocity as a function of time is simply,

$$\frac{dv(t)}{dt} = \frac{\hbar k\gamma}{2m}\frac{s_o}{1 + s_o + (\frac{2(\delta-kv(t))}{\gamma})^2} \qquad (4.7)$$

where we have simplified the vectors to scalars by only considering the probe beam propagation direction. Given an initial velocity along the probe beam direction this equation can be solved to calculate the detuning from $5D_{5/2}F=4$ versus time. Finally, the equation for the two-photon transition amplitude from second-order perturbation theory, Eq. (3.12), may be used to calculate the expected signal versus time.

It is possible to solve Eq.(4.7) analytically for the velocity versus time assuming the initial velocity of the atom is zero. This method correctly predicts the positions of the peaks in Fig. (4.9), however, it does not account for several effects that broaden the peaks observed in our results. One of the most important simplifications made is assuming a constant on probe beam intensity. In our experiment we expect to have a radial intensity dependence due to the Gaussian mode of the beam, in the focal plane the intensity varies as,

$$I(r) = I_o exp[-2\frac{r^2}{w_o^2}] \qquad (4.8)$$

where I_o corresponds to the on-axis intensity ($\sim$0.8 mW/cm^2) and the beam waist radius w_o is $\sim$ 130 μm. If we assume a constant radial density of atoms and a two-photon transition rate that varies as I^2, it is possible to calculate the signal strength versus radial displacement. The number of atoms in a thin ring at fixed radius is proportional to r, so the radial dependence of the signal is proportional to $rI(r)^2$.

To incorporate the radial intensity variation into s_o and several other stochastic processes we turn to a numerical simulation based on Eq. (4.7). Although we also modeled the longitudinal dependence of the signal, due to absorption and beam focusing, it is sufficient to consider only the radial degree of freedom to generate the results in Fig. (4.9). We divided the radial direction into 20 segments from r=0 to r=3w_o, and each segment had 20 atoms. Each atom was assigned an initial velocity, assuming a Maxwell-Boltzmann distribution at T=20 μK. The atom velocity, and two-photon signal weighted by $r\Delta r$, was solved for versus time to 300 μs in 100 steps. To incorporate the stochastic nature of the number of photons scattered per unit time, Δt, each atom obtained a random velocity kick in each time segment. The magnitude of the random velocity kick is 2$\times v_r$ multiplied by a random number from a Normal distribution of standard deviation $\sqrt{N}$, where

N is the mean number of photons scattered given by $\gamma'_{5P}\Delta t$, see Eq.(4.6). Summing over the predicted two-photon signal from each atom at each radial segment provides quite a good estimate of the total signal versus time. However, one final stochastic process that was included is the variation of the probe laser frequency given by the comb linewidth. We assumed the laser noise to be a slow process compared to 300 μs, meaning for each of the above 300 μs simulations the laser was at a fixed frequency in the lab frame. The final theory result shown in Fig. (4.9) was generated by repeating the above simulation 50 times, and randomly selecting a laser frequency consistent with the Lorentzian comb mode linewidth. Clearly the agreement between this model and the measured signal versus time in quite good.

For all of our spectroscopy experiments we would like to reduce the net momentum transfer to the atoms as much as possible. We do this by balancing the radiation pressure on the atoms along the probe beam direction with another counter-propagating probe beam at the same intensity. Before the Ti:Sapphire beam enters the MOT chamber it is focused with a 1 m lens then split into two equal intensity beams with a non-polarizing 50:50 beam splitter. By far the most tedious alignment issue with this experiment is overlapping these beams at the atoms to optimally balance the radiation pressure. One of the reasons this is tedious is that to have sufficient signal to noise in our two-photon signal requires $\sim$1 s of real time data acquisition, or 100 MOT cycles. First, the signal from one beam is maximized by finding the center of the atom cloud, adjustments of the focusing lens may also be necessary for this step initially. Then the spatial overlap of the two beams in the center of the atom cloud is found by maximizing the two-beam signal. To obtain our best results we would then further optimize by scanning a two-photon transition line and adjusting the beam overlap so as to measure the narrowest linewidth. Figure (4.10) shows the measured two-photon
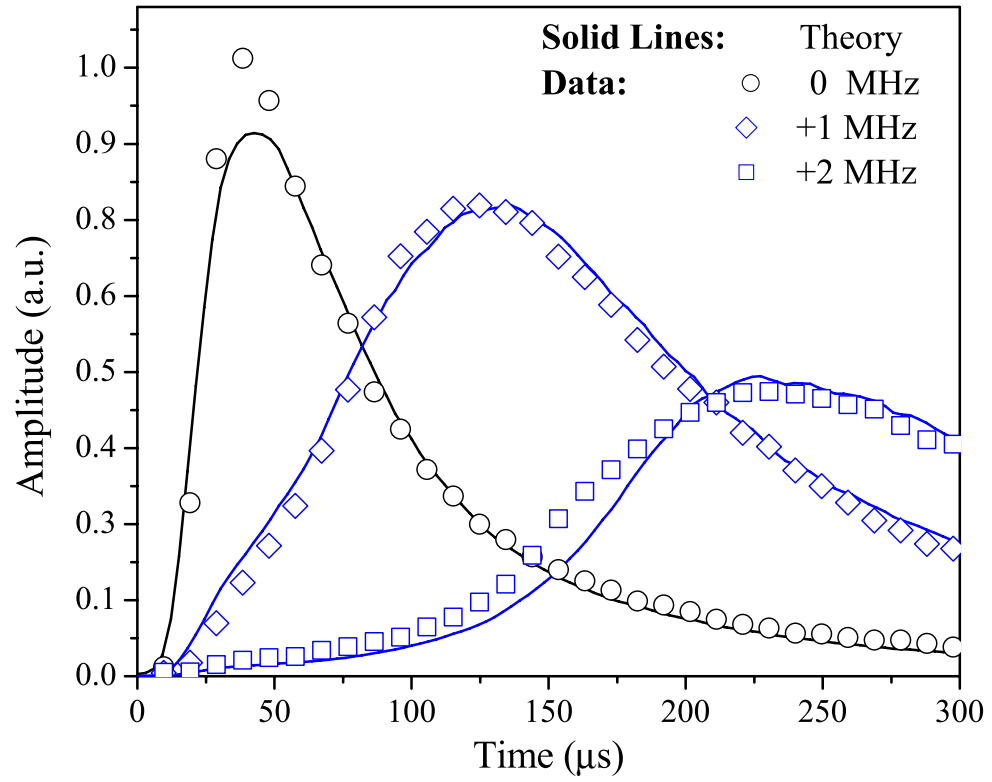
Figure 4.9: Measured signal and theoretical prediction versus probing time for three detuning configurations. Detunings are from the intermediate $5P_{3/2}F{=}3$ state, the $5D_{5/2}F{=}4$ detuning is twice as large.

transition lines (symbols) together with a Lorentzian fit (solid lines) under counter-propagating and single beam excitation. We set the two channel photon counter to record the signal from 0-20 μs and also 100-120 μs to observe the linecenter and width after some probing time. Clearly the use of well overlapping counter-propagating beams significantly reduces the linecenter shift versus time seen in the single direction excitation. Despite the fact the net momentum transfer to the atoms is nearly zero, there is still heating of the atoms, which appears as an increase of the linewidth versus time in the counter-propagating case.

4.2.3   AC Stark Shift and Power Broadening

Ideally we would like to measure the frequency and linewidth of a particular two-photon transition without any perturbations. In this section we discuss two of the most important fundamental perturbations from the probe light itself, the AC-Stark shift and power-broadening. Unlike the case of an ideal two-level system, for a two-photon transition in a three-level atom there is almost always a Stark shift of the excited state. In the case of ^{87}Rb this is due to the fact that the intermediate state is shifted $\sim$1 THz from exactly half of the two-photon transition frequency. So if we were to try and resonantly excite a 5D state with two-modes, of equal or dissimilar frequencies, there is always a mode detuned from intermediate state resonance, resulting in an AC-Stark shift. Figure (4.11)(**a**) shows a diagram of the relevant three-level system with a pair of one and two-photon resonant modes. Only one configuration of the modes is resonant with the 5P intermediate state, the other configuration is detuned and causes a Stark shift. In this case the second configuration, while two-photon resonant, is detuned from $5P_{3/2}$F=3 by 2 THz. The near intermediate resonance Stark shift has been studied using two-mode excitation in Alkali vapors by Liao and Bjorkholm [65].

To study the Stark shift and power-broadening we measured the $5S_{1/2}$F=2
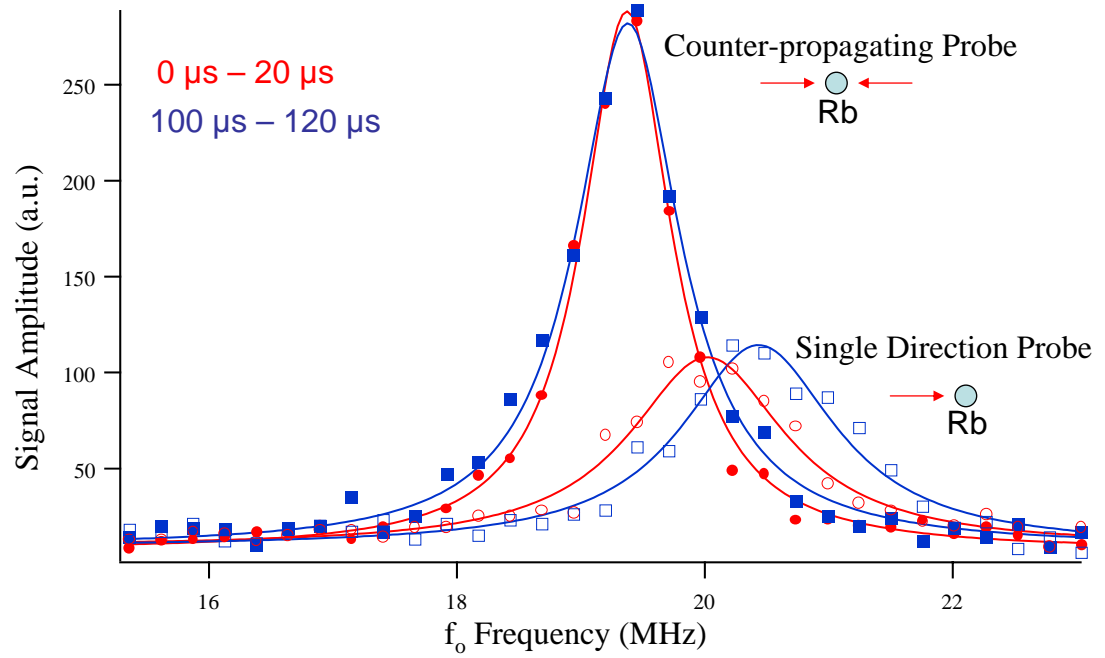
Figure 4.10: Measured signal (symbols) and Lorentzian lineshape fits (solid lines) under counter-propagating and single direction excitation. The color of the symbols and lines correspond to different measurement delays after the probe beam is turned on; red for zero delay and blue for 100 μs delay. The f_o for two-photon resonance of zero velocity atoms is 18.14 MHz.
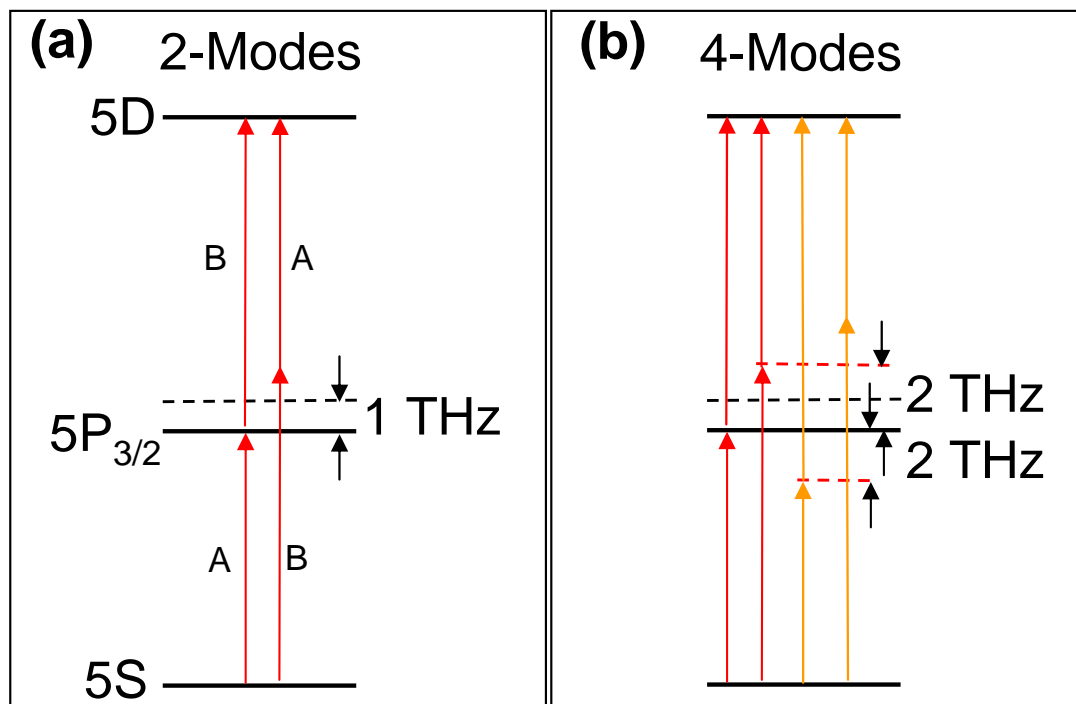
Figure 4.11: (**a**) Three-level system under two mode excitation, due to the 1 THz offset of the $5P_{3/2}$ states from half the two-photon frequency there are two different mode pair configurations. (**b**) Same three-level system under four mode excitation illustrating the possibility to approximately cancel the Stark shift arising in (**a**).

to $5D_{5/2}F{=}4$ transition frequency and linewidth with three different intermediate resonance conditions. We have already discussed the f_r and f_o frequencies for excitation with one and two-photon resonance. In addition to the on intermediate resonance set of comb frequencies we also used two other pairs of f_r and f_o corresponding to ± 4 MHz $5P_{3/2}F{=}3$ detuning. For all three cases of varying intermediate state detuning the $5D_{5/2}F{=}4$ state is two-photon resonant. Note that for these experiments we used counter-propagating probe beams in an attempt to balance the radiation pressure, however, there is some residual imbalance. We also used the LC shutter in this experiment to turn on/off the Ti:Sapphire, so for the first 40 μs of data the probe power is increasing to its maximum value.

Figure (4.12) shows the measured linecenter shift versus probing time for the three cases of intermediate state detuning. The 420 nm fluorescence was counted using the SR-430 multichannel photon counter to obtain time resolution. For each case of intermediate state detuning, f_o was scanned to measure the two-photon transition lineshape. Using this record of signal versus both f_o and time we fit each line with a Lorentzian function and extracted the linecenter and FWHM linewidth. Clearly after 40 μs of probing time the ± 4 MHz detuned cases exhibit much less of a lineshift versus time. This decrease is due to the reduced 5P population and thus radiation pressure compared to the on-intermediate-resonance case. To obtain the best possible estimate of the unperturbed linecenter frequency for our spectroscopy results we extrapolated to zero probing time.

We model the effect of the Stark shift and power-broadening due to the comb excitation using the three-level density matrix theory discussed in section (??). The driving field was a Gaussian envelope electric field with a 35 fs pulse duration. Although we have developed a version of this model that uses excitation by counter-propagating pulses, we only used excitation from one direction for this numerical study. The reason being that properly treating the counter-propagating
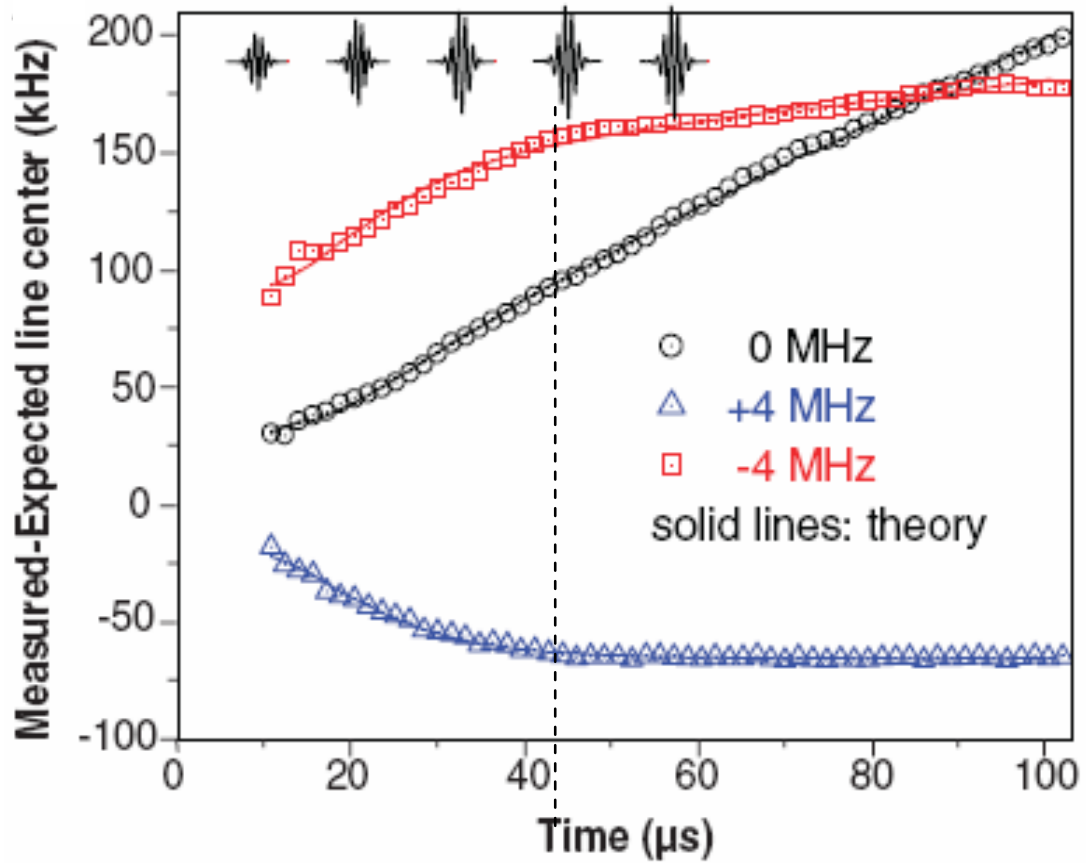
Figure 4.12: Measured linecenter shifts from the literature value of the $S_{1/2}F=2$ to $5D_{5/2}F=4$ two-photon transition frequency versus time and intermediate state detuning. During the first ~40 μs the LC shutter is opening and therefore the power is increasing.

pulse excitation requires an added spatial integration. Computationally this is too lengthy considering the fact we wish to vary f_o and the peak field strength independently. Another shortcoming of this three-level model is that the magnetic sub-levels are not included. Table (4.1) contains the angular part of the reduced dipole moments for transitions relevant with linear polarized light.

Intermediate State	μ'_{gi}	μ'_{if}	$\mu'_{gi}\mu'_{if}$
5P$_{3/2}$F=3 m$_F$=2	$\frac{1}{3}$	$\sqrt{\frac{3}{35}}$	0.0976
5P$_{3/2}$F=3 m$_F$=1	$\frac{2\sqrt{\frac{2}{5}}}{3}$	$\frac{\sqrt{\frac{3}{7}}}{2}$	0.1380
5P$_{3/2}$F=3 m$_F$=0	$\frac{1}{\sqrt{5}}$	$\frac{2}{\sqrt{35}}$	0.1512

Table 4.1: The angular part of the reduced dipole matrix elements for the 5S$_{1/2}$F=2 to 5P$_{3/2}$F=3 to 5D$_{5/2}$F=4 transition with linear polarized light (q=0).

Due to the large variation of the dipole moment products between different m_F levels, optical pumping could potentially change the two-photon transition rate. Instead of running the model for each m_F level and incoherently summing the populations we used the average dipole moments. Analytic expressions for the Stark shift and power-broadening have been derived for a three-level system driven by two-modes by Brewer and Hahn [51]. However, to arrive at an analytic expression several simplifications were made, such as equal Rabi frequencies for each transition step.

Figure (4.13) shows the predicted linecenter shift versus peak field strength for each 5P detuning case. The linecenter shifts at 10^7V/m seen for ±4 MHz detuning agree well with the ± ~150 kHz shift measured in the experiment. For the case of zero intermediate state detuning the Stark shift is significantly reduced. We attribute this to the fact all comb modes are equally spaced, so the shift from the pair detuned N×f_r below 5P$_{3/2}$F=3 is canceled by the shift from the pair tuned symmetrically above 5P$_{3/2}$F=3.

At large electric field strengths even the on-intermediate-resonance case

Figure 4.13: Theoretical predictions for the AC-Stark shift of the $5S_{1/2}F=2$ to $5D_{5/2}F=4$ two-photon transition frequency versus peak field strength and intermediate state detuning. We used a 35 fs FWHM Gaussian driving field centered at 778 nm to drive our three-level density matrix model.

starts to exhibit some Stark shift, this appears to be due to the finite spectral width and center wavelength. For example, the Stark shift using a peak field strength of 3×10^7 V/m is (-148 kHz, -98 kHz, -36 kHz, 30 kHz, 89 kHz) for center spectrum wavelengths (776 nm, 778 nm, 780nm, 782 nm, 784 nm). Referring back to Fig. (4.11)(**b**), in the case of four mode excitation it is possible to cancel some of the Stark shift. We discussed the 5P resonant two mode case previously, in that case the Stark shift arises from a mode pair detuned by 2 THz from the intermediate state. If we introduce two more modes of equal strength detuned 2 THz below intermediate resonance, canceling that particular source of Stark shift. In this four-mode example, the Stark shift arises from a mode pair detuned 4 THz above the intermediate resonance, and gives rise to less of a shift. The Stark shift cancellation due to comb excitation may be thought of as an extension of this four mode example, although with >100,000 modes in the ~55 nm FWHM Gaussian spectrum. This explanation is only meant to provide a conceptual picture. Further study is required to understand the extent to which the Stark shift differs between two-mode and comb-based two-photon excitation.

We also measured the power-broadening versus time and intermediate state detuning in the same experiment. Figure (4.14) shows the measured FWHM linewidths from the Lorentzian fits of each line versus time. Similar to our study of Stark shifts the on-intermediate-resonance case exhibits an increasing linewidth versus time even after the LC shutter is fully opened. This is due to the heating caused by the counter-propagating probe lasers discussed in subsection (4.2.2). At the expense of an increased Stark shift we can retain narrower linewidths by detuning from intermediate resonance, seen in the ±4 MHz detuned results. We observe what appears to be a signature of Doppler cooling, or more accurately suppressed heating, in the case of -4 MHz (red) detuning from the intermediate state. This is evident in the reduced linewidth measured with red detuning ver-
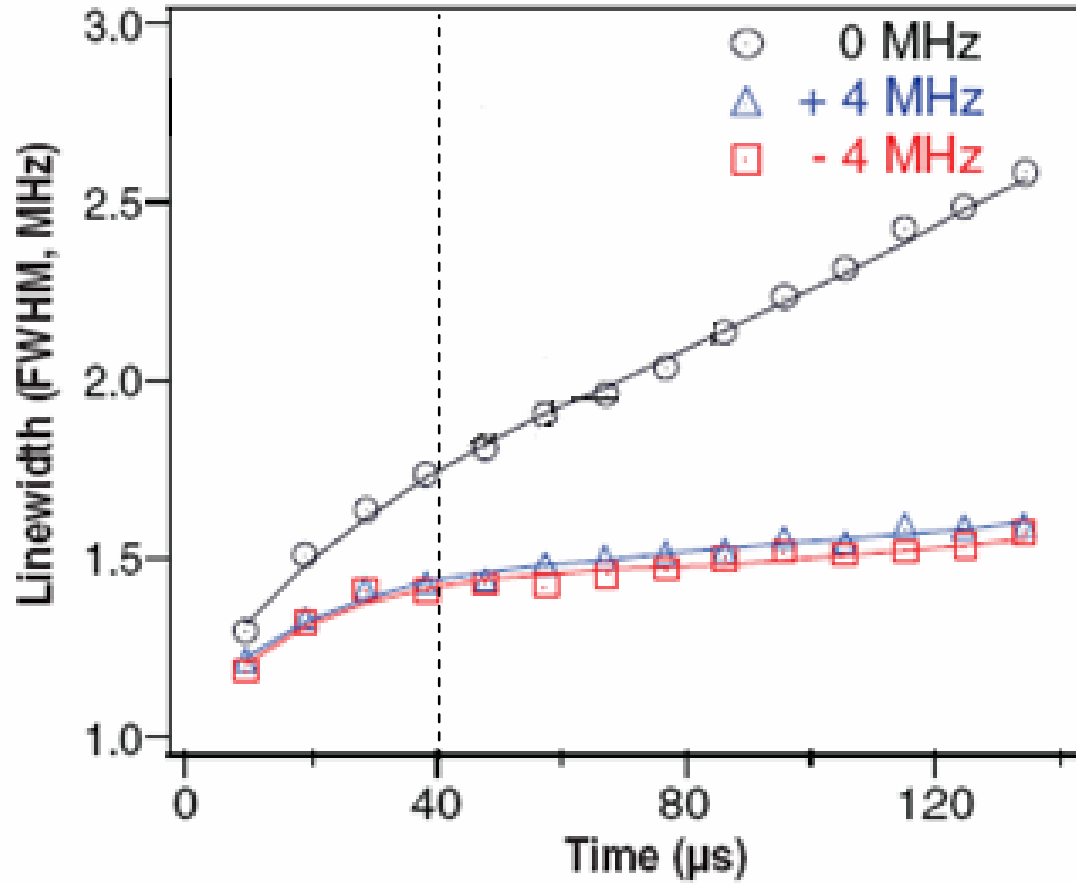
Figure 4.14: Measured linewidths of the $S_{1/2}F=2$ to $5D_{5/2}F=4$ two-photon transition versus time and intermediate state detuning. During the first $\sim$40 μs the LC shutter is opening and therefore the power is increasing.

sus equal blue detuning. Of course regardless of intermediate state detuning all linewidths tend to increase versus time so there is still heating of the atomic ensemble due to the 5S-5P incoherent photon scattering. At very short times, before the radiation pressure has caused significant heating, the linewidths corresponding to ± 4 MHz intermediate state detunings are narrower than the on-resonance case. This is indicative of reduced power broadening, and is due to a reduced resonant enhancement of the two-photon transition rate.

The theoretical prediction for power-broadening was obtained in the same manner as the previously discussed Stark shifts. Figure (4.15) shows the results of our theoretical model for a range of peak electric fields. For the on-intermediate-resonance case the power-broadened FWHM linewidth at 10^7 V/m is 1.1 MHz. This serves to provide an estimate of the effect of power-broadening only, the experimental results for this case exhibit a large line-broadening due to heating as well. Unfortunately this set of experiments was among the first conducted and we did not have the Pockels cell yet. Perhaps better agreement would be obtained between theory and experiment if the peak field strength was not a function of time, due to the slow turn on of the LC shutter. Then power-broadening could be more clearly separated from radiation pressure effects which take time to accumulate. Note that the coherent accumulation experiment presented in section (4.1) was conducted with a Pockels cell, in that case we observed good agreement between theoretically predicted and experimentally measured power-broadened linewidths. But the atoms were excited for at most ~ 13 μs, corresponding to the 80 pulse excitation case.

4.2.4   Zeeman Shift

There are two primary sources of magnetic field that may Zeeman shift the atomic energy levels. The anti-Helmholtz magnetic field used to trap the atoms
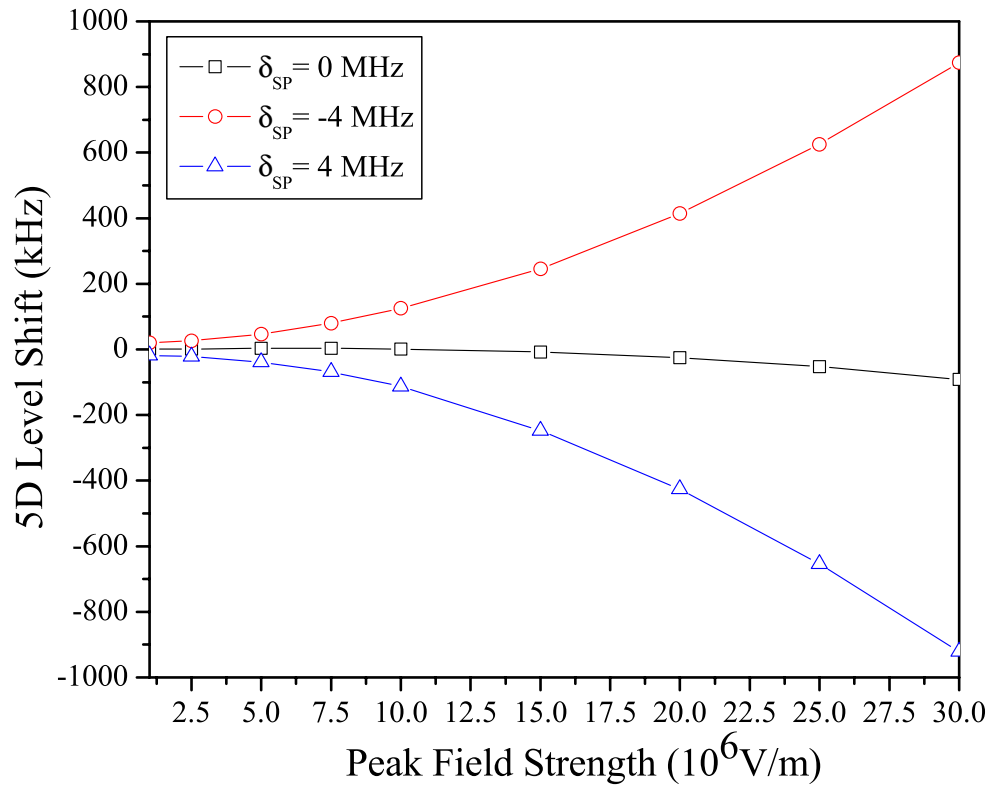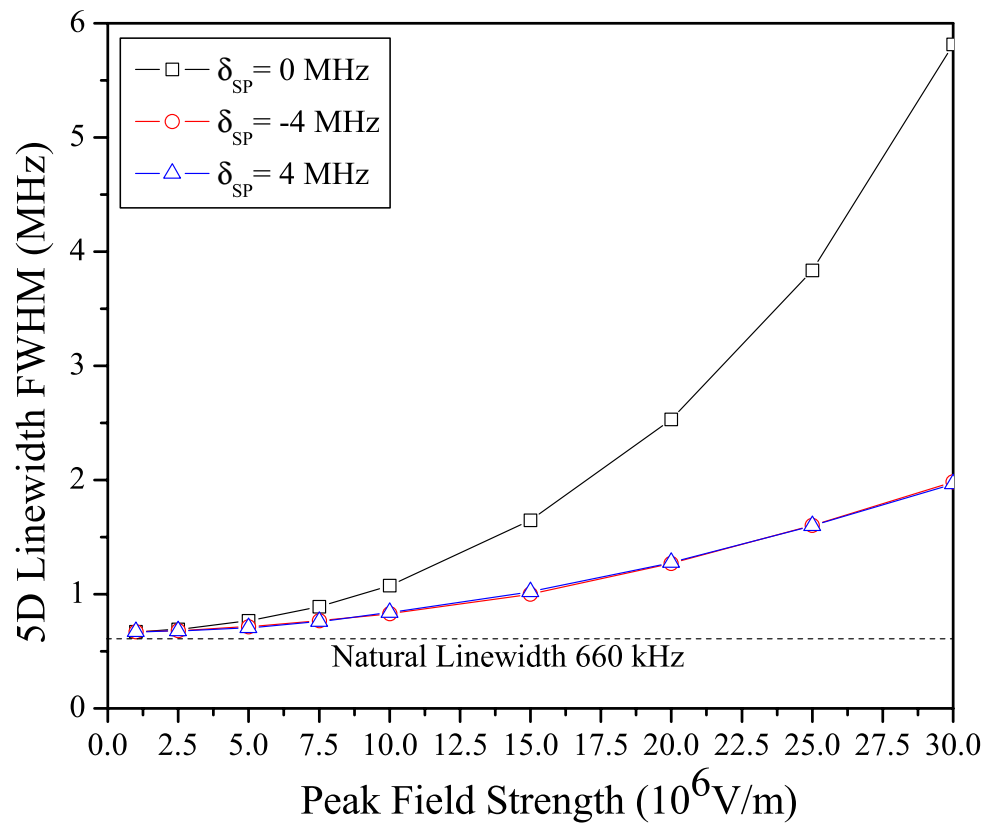
Figure 4.15: Theoretical predictions for power-broadened linewidth of the $5S_{1/2}F=2$ to $5D_{5/2}F=4$ two-photon transition versus peak field strength and intermediate state detuning. We used a 35 fs FWHM Gaussian driving field centered at 778 nm to drive our three-level density matrix model.

in the MOT and the ambient magnetic field, for example from the Earth. Ideally we would like to conduct spectroscopy in a magnetic field free environment so we use three sets of large Helmholtz coils to compensate for the ambient field. These Helmholtz coils are mounted around the MOT and oriented to provide three relatively homogeneous orthogonal static magnetic fields.

To adjust the three pairs of Helmholtz coil magnetic fields we probe the $5S_{1/2}F=2$ to $5P_{3/2}F=3$ to $5D_{5/2}F=4$ two-photon transition with left and right circular polarized light. This particular two-photon transition is well suited for this study because the population will tend to be pumped to the stretched states, $m_F=\pm F$, under σ^+ or σ^- excitation.

As we discussed previously, the trapping magnetic field is turned off before we probe the atoms, however, this process takes some time. We determined a reasonable delay between the time we turned off the trapping magnetic field and probe the atoms. This was done by turning on the Ti:Sapphire and measuring the linecenter shift at various delays after the trapping magnetic field was turned off. At times less than ~0.5 ms we observed large linecenter shifts, from 4 MHz at zero delay to 100 kHz at 0.5 ms delay. To be certain the Zeeman shift from the trapping magnetic field was negligible we measured all of our data with at least a 2 ms delay.

The Helmholtz coils used to compensate for the ambient field are oriented such that it is relatively easy to probe the atoms with a beam parallel to the generated magnetic field. For example, there is a pair of Helmholtz coils oriented to create a vertical magnetic field, to adjust this field we probe the atoms with the Ti:Sapphire beam vertically. For each of the three directions we record the two-photon transition lineshape with left and right circular polarized light versus the current applied to the Helmholtz coil. Experimentally great care was taken to ensure the quality of the polarization, meaning we reduced the ellipticity as best

we could.

Figure (4.16) shows the resulting linecenter shift from some arbitrary value versus the applied magnetic field. The magnetic field at the atoms is weak so we are in the anomalous Zeeman regime, meaning the linecenter shift is a linear function of magnetic field. The optimal field value is given by the crossing of two linear fits to the data, one for left circular the other for right circular. This process is repeated at least once for all three directions, in practice we did each direction twice to ensure the best results.

4.2.5   Incoherent Optical Pumping

Incoherent optical pumping is a particularly important, and complicated, process in DFCS. Recall that the only closed two-photon transition is $5S_{1/2}F=2$ to $5P_{3/2}F=3$ to $5D_{5/2}F=4$. Population excited to either the intermediate or final state in this transition will eventually spontaneously decay back to the $5S_{1/2}F=2$ ground state. We are simplifying the optical pumping process somewhat here by ignoring the magnetic sub-levels, the populations of which are determined by incoherent optical pumping as well. With the exception of this one closed transition, the signal size of all the other transitions is influenced by incoherent optical pumping.

In general all of the two-photon resonant transitions are resonant from only one of the two $5S_{1/2}$ hyperfine levels. So the signal strength depends on the amount of population in the resonant ground state. Because of the significantly faster scattering rate of the 5P states compared to the 5D states, most of the optical pumping occurs due to decay from the 5P states. For our typical probe intensity the two ground states reach a steady state population distribution in a time of order $\sim$1-10 μs. So any initial state preparation we may do with the trap or repump laser before probing is quickly undone.
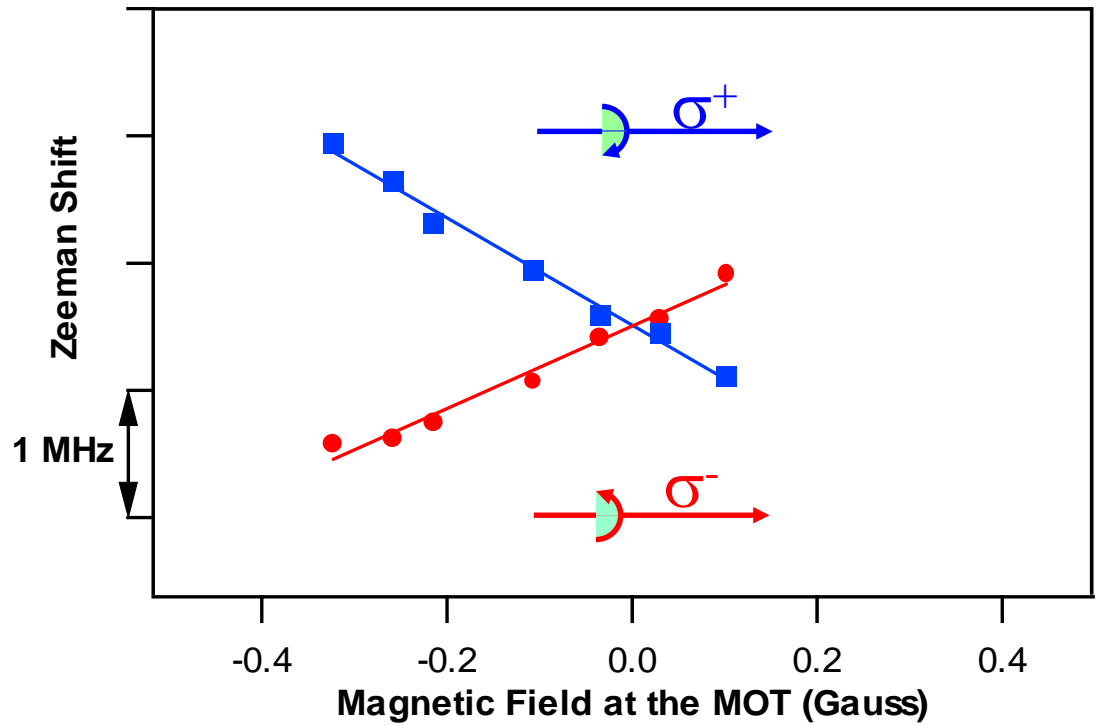
Figure 4.16: Example linecenter crossing for σ^+ and σ^- excitation of the $5S_{1/2}F=2$ to $5D_{5/2}F=4$ two-photon transition. The x-axis scaling is calculated from the linecenter shifts and atomic properties.

In our early experiments we noticed many lines were missing from our measurements. Suspecting incoherent optical pumping to the off-resonant ground state we employed a repuming scheme interleaved with our data collection. Instead of recording data continuously we gated the photon counter to only record data for 2.5 μs every 5.0 μs, over a total time of 0.5 ms for every MOT cycle. After each 2.5 μs counting window we turned on the repump laser for 2.5 μs to pump population from $5S_{1/2}F=1$ back to $5S_{1/2}F=2$. Figure (4.17) shows the lines we measured by scanning f_o with and without the interleaved repumping scheme. Clearly this greatly increases our signal for all but the one closed transition. The reason that the incoherent optical pumping process is complicated to predict is that it is not only due to the decay from the resonant intermediate state. The steady state population distribution is also a function of the rate at which the comb itself repumps population. This point will be made quite evident in subsection (4.4) where our optical pumping model plays a key role.

4.3   Two-Photon Spectroscopy Results

With a clear understanding of the systematic effects we now proceed to use the comb for direct frequency comb spectroscopy. There are two unique advantages of using the comb directly for spectroscopy. The first and perhaps more important is that we may determine the absolute frequencies of the transitions with reference to the cesium standard. Initially we studied two-photon transitions to a set of hyperfine $5D_{5/2}$ and $5D_{3/2}$ hyperfine levels. As this was the first experimental demonstration of DFCS these transitions served as excellent proof-of-principle measurements because all of them had been measured previously by conventional cw-laser spectroscopy. In fact the uncertainty in the previous measurements of these transitions was 10-16 kHz, much less than our laser f_r. This allowed us to determine the comb mode order numbers without additional measurements. We
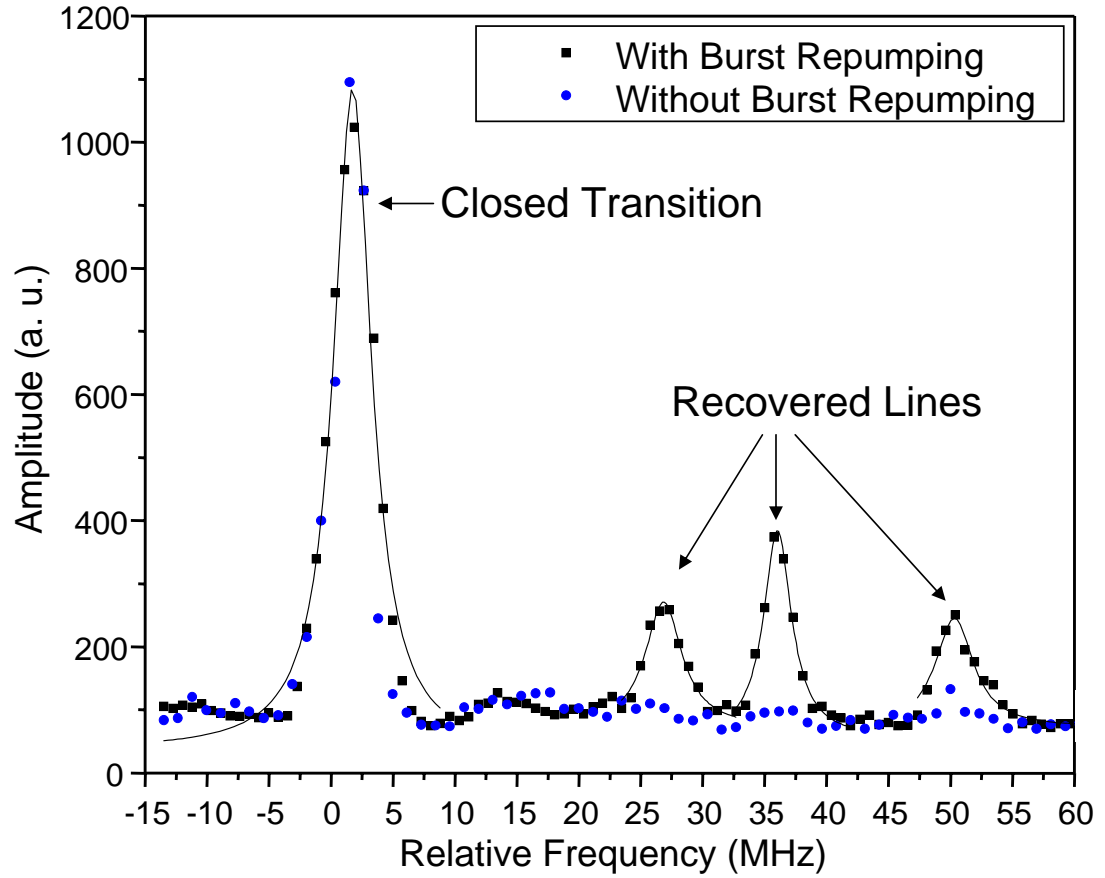
Figure 4.17: Measurement of several two-photon transitions illustrating the effect of incoherent optical pumping. Black symbols are measurements made with interleaved repumping, blue symbols without repumping. The only closed transition, $5S_{1/2}F=2$ to $5P_{3/2}F=3$ to $5D_{5/2}F=4$ is unaffected by the repumping.

also conducted measurements of the 5S to 7S two-photon transitions, the frequencies of which were not known to better than 100 MHz. To resolve the absolute transition frequencies for 7S we had to determine the mode order numbers using multiple measurements. A second advantage of DFCS is the broad spectrum of the femtosecond pulses. We show that simply scanning f_r over $\sim$26 Hz excited all allowed two-photon transitions within the comb spectrum.

4.3.1   Repetition Rate Scan

After reducing the systematic errors such as Zeeman shifts and radiation pressure by studying the strong transition to $5D_{5/2}F=4$ we scanned f_r of the laser to observe the full set of two-photon transitions. The two-photon transition frequency to all of the 5D states is $\sim$770.5 THz, as a very rough estimate. The resonance criteria for two-photon transitions is given by,

$$\nu_{2\gamma} = f_r \times (N_1 + N_2) + 2 \times f_o \qquad (4.9)$$

where N_1 and N_2 are the integer mode order numbers. Of course this equation has many solutions within the spectrum of the comb. However, the sum $N_1 + N_2$ is the same for all mode pair combinations with a given f_r and f_o. Considering we use $f_r \sim$100 MHz, the sum of mode order numbers $N_1 + N_2 \sim$7.7$\times 10^6$. Similarly for the intermediate state transitions the mode order number is $\sim$3.8$\times 10^6$. Because of the fact $f_r/3.8 \times 10^6 \sim$26 Hz, changing f_r by 26 Hz shifts the comb such that the one-photon transition is resonant with the next comb mode, $N_1 - 1$. In the case of the two-photon transitions the change of f_r needs to only be 13 Hz before the two-photon resonance condition is again satisfied. Therefore when we scan the comb f_r we expect the two-photon transitions to repeat every 13 Hz and the single-photon transitions to repeat every 26 Hz. Of course this is not true if f_r is changed so much that the resonant mode order numbers change appreciably.

In Fig. (4.18) we present the measured signal versus f_r over a range of 28 Hz with a fixed f_o=-19.0 MHz. This result provides a very clear demonstration of the versatility of DFCS for measuring many different transition frequencies. Between the two ground hyperfine levels and eight 5D hyperfine levels there are a total of 14 allowed two-photon transitions. Considering we know the frequencies of these transitions from previous measurements it is possible to identify each of the 14 transitions in this result. There are also two extra small peaks in this data set that do not correspond to any 5S to 5D transition, we attribute these to 5S to 7S transitions and will discuss these in further detail in subsection (4.3.2).

The largest peak corresponds to when the comb is resonant from $5S_{1/2}F=2$ to $5D_{5/2}F=4$ with perfect intermediate state resonance with $5P_{3/2}F=3$. For this particular experiment we used a value of f_o and scanned f_r over a range such that this three-level resonance would occur. There is a second clearly identifiable peak corresponding to a transition to the same final state, however in this case the two-photon resonant comb pair is detuned from the intermediate state. Notice there are two peaks that appear virtually identical in signal size and width at ∼0.8 Hz and ∼26.8 Hz. These peaks are due to both the two-photon and single photon resonance conditions repeating after a change of f_r by 26 Hz.

4.3.2   Absolute Frequency Measurements

To conduct high-resolution absolute frequency measurements of several two-photon transitions we need to focus on individual lineshapes. We have selected 5 two-photon transitions from 5S to 5D to measure as an initial test of DFCS. After we successfully measured these transitions we shifted the center wavelength and expanded the spectral width of our Ti:Sapphire laser to be able to measure the 5S to 7S transitions. We will discuss how to determine the relevant mode order numbers in the context of our 7S measurements.
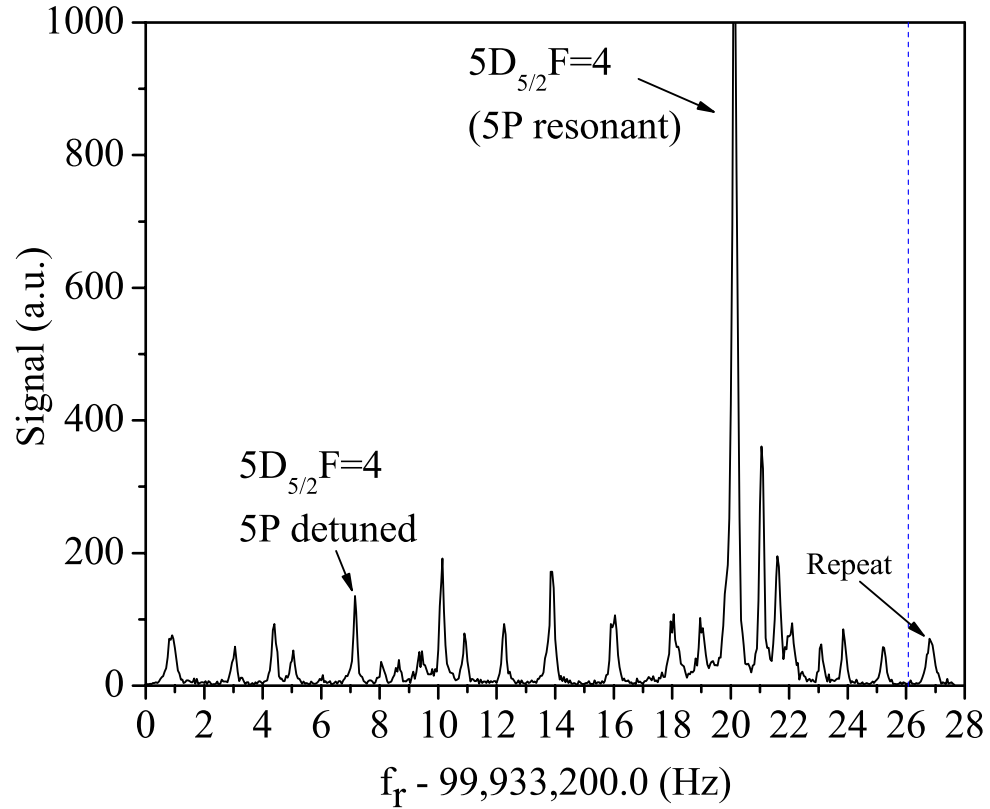
Figure 4.18: Full two-photon transition spectrum recovered by scanning f_r by 26 Hz. The strongest peak is for intermediate and final state resonant excitation of the $5S_{1/2}F=2$ to $5D_{5/2}F=4$ transition. The two nearly identical peaks at ~0.8 Hz and ~26.8 Hz correspond to the same excited hyperfine level and intermediate state detuning.

As was discussed previously we know the frequencies of all of the 5P and 5D hyperfine levels from previously published literature measurements. So instead of scanning f_r over all of the transitions we calculate specific values of f_r and f_o such that the comb is not only two-photon resonant but also resonant with an intermediate state. This allows us to reduce the Stark shift discussed in subsection (4.2.3). With a fixed value of f_r we measure the two-photon lineshape by scanning f_o around the resonant frequency.

To estimate the linecenter frequency corresponding to a relatively unperturbed atom we record the signal versus time and estimate the linecenter using a fit to the data. Specifically we counted photons using the SR430 multichannel photon counter with a per bin duration of 160 ns. We then post-process the data into new bins yielding a moving average, this was done by adding up 40 bins of 160 ns duration each and shifting by 5 bins. So the end result is a set of bins each with a 6.4 μs in 800 ns intervals. These times were chosen so that there is enough signal to noise in each 6.4 μs bin to reasonably fit the data to a Lorentzian lineshape and extract the linecenter.

Due to the fact the power transmitted through the LC shutter is a function of time we can not simply extrapolate the linecenter data to zero time using a linear fit function. Instead we fit the linecenter data minus the expected linecenter value with a function of the form,

$$\Delta\nu'(t) = c_1 + c_2 \times P(t) + c_3 \times (P(t) \times t) \tag{4.10}$$

where $\Delta\nu'(t)$ is the linecenter shift from the expected value versus time, $P(t)$ is the power versus time measured after the LC shutter, and t is the time after data collection initiates. The coefficient c_1 is the estimate of the unperturbed linecenter frequency shift from some reference frequency. The last two coefficients are used to empirically model the Stark shift and radiation pressure Doppler shift of the

linecenter frequency. We expect the Stark shift to be solely a function of power for a fixed probe beam mode and intermediate state detuning, so it is modeled as $c_2 \times P(t)$. The Doppler shift due to radiation pressure on the other hand is an accumulated effect, at short times we expect this to vary linearly with power and time, so it is modeled as $c_3 \times (P(t) \times t)$. This type of fitting function assumes that the atom is not Doppler shifted from intermediate state resonance, as we discussed in subsection (4.2.2), the actual shift versus time is nonlinear. Initially, when the LC shutter is just beginning to transmit the probe light the signal to noise ratio is not sufficient to reasonably fit the lineshape data. For this reason we only fit the linecenter data with Eq.(4.3.2) from about 20 μs to 100 μs. This data analysis technique proved quite successful, the one-sigma uncertainty in our estimates of c_1 ranged from $\sim$11 kHz to $\sim$50 kHz.

Conducting direct frequency comb spectroscopy of the 5S to 7S transition required several additional considerations beyond our 5D measurements. The first of which is that the optimum Ti:Sapphire center wavelength is different. Like our previous measurements, we wish to conduct two-photon spectroscopy with a resonant intermediate state. The resonant wavelengths are shown in Fig. (4.1), it can be seen that to excite 7S via a $5P_{3/2}$ state requires 780 nm and 741 nm light. To provide more power at the 741 nm wavelength the center wavelength of the Ti:Sapphire was shifted to 770 nm. Unfortunately further blue shifting of the spectrum deteriorates the f_o beat signal too much.

A second important difference in our 7S measurements is that the two-photon transition frequency was not initially known to better than $\sim f_r/2$, therefore we must determine the resonant mode order numbers. Recall the equation for the two-photon transition frequency is,

$$\nu_{2\gamma} = f_r \times (N_1 + N_2) + 2 \times f_o. \tag{4.11}$$

We know the 5S to $5P_{3/2}$ transition frequencies very well and can therefore assign a mode order number to N_1. The question is how do we determine N_2 ? If the measured two-photon transition linecenter frequency had zero uncertainty we could simply measure the line with a slightly shifted f_r and the peak would appear at a shifted f_o. Clearly the frequency shift of $\nu_{2\gamma}$ is a function of N_2 so this would allow the determination of N_2. The problem is that there is uncertainty in our linecenter frequency measurements. So differentiating between say, N_2 and N_2+1 requires a change of f_r by at least the uncertainty in our estimate of f_o corresponding to the linecenter.

From previous measurements of the 5S to 7S transition we know that the frequency is of order $\sim$788.8 THz. This corresponds to an estimated $N_1 + N_2$ of 7.888×10^6, so the two-photon resonance condition repeats every $\Delta f_r \sim$12.6775 Hz for an $f_r \sim$100 MHz. In our experiment we measured the two-photon transition linecenter at two values of f_r separated by 600 kHz. Considering this change in f_r is much greater than 12.6775 Hz, the resonant mode order numbers changed between the two measurements. In principle one could measure the change in mode order numbers between the two measurements by observing how many times the peak repeats as f_r is scanned over 600 kHz. This is of course very tedious experimentally. Fortunately for the 5S to 7S measurements we can determine the *change* of mode order number N_2 based on previously published cw-laser based measurements.

Suppose we define the integer $M=N_1 + N_2$ where we know N_1, and N_2 is to be determined. We denote our uncertainty in the linecenter frequency as δf_o. The two equations we have to solve for the change in M are,

$$\nu_{2\gamma} = f_r \times (M) + 2 \times (f_o + \delta f_o)$$

$$\nu_{2\gamma} = (f_r + \Delta f_r) \times (M + \Delta M) + 2 \times f_o' \tag{4.12}$$

where $f'_o = f_o + \delta f_o + \Delta f_o + \delta f'_o$. We have introduced Δf_o to denote the change in f_o between the two measurements and $\delta f'_o$ is the error in our linecenter frequency estimate. Note that the change in f_r is given by Δf_r and can be measured at the sub-mHz level. The above set of equations can be solved for ΔM, the change in total mode order number,

$$\Delta M = -\frac{M\Delta f_r + 2\Delta f_o + \delta f'_o}{f_r + \Delta f_r}. \tag{4.13}$$

Considering the denominator is a large number of order 10^8 and ΔM must be an integer we can interpret this equation. We know $2\Delta f_o$ well, by definition the error is given by $\delta f'_o$, so we can calculate the ΔM from this contribution. Our uncertainty in the second linecenter estimate, $\delta f'_o$, is 120 kHz or less, so when divided by $(f_r + \Delta f_r)$, is much less than an integer. The remaining term is,

$$-\frac{M\Delta f_r}{f_r + \Delta f_r}. \tag{4.14}$$

Because of the fact $\Delta f_r \ll f_r$ any uncertainty in our estimate of M is suppressed. Using numbers from our experiment, $f_r \sim 100$ MHz and $\Delta f_r \sim 600$ kHz, it would take an uncertainty in M of the order ~ 160 to cause a shift of ΔM by 1. Given our laser repetition rate of 100 MHz this would correspond to a 16 GHz initial uncertainty in the two-photon transition frequency. Fortunately this is not the case for the 5S to 7S transitions which have been roughly measured [66]. For further reading on how to estimate an absolute transition frequency using a frequency comb refer to references [67, 68].

Now that we have estimated ΔM it can be used to solve Eqs. (4.12) unambiguously for M and thus the two-photon transition frequency $\nu_{2\gamma}$. Of course there is still the uncertainty δf_o in our lineshape fit which can not be avoided, so our knowledge of $\nu_{2\gamma}$ is limited to δf_o. Experimentally the exact value of f_r is not known perfectly, however, we generally measure it on a Cesium referenced

counter. If we count long enough to reduce the uncertainty in f_r to the 1 mHz level the resulting error in the two-photon linecenter is of order $\sim$7.7 kHz, less than our lineshape fit uncertainty.

The resulting absolute frequency measurements for several 5D and 7S hyperfine levels are shown in Table (4.2). We report the linecenter frequencies we determined from the previously discussed fit to the linecenter versus probing time, along with the one-sigma uncertainty in our estimate. The quoted literature values were all measured using traditional cw-laser spectroscopy. Absolute frequency measurements of the 5S to 5D transitions are reported in reference [69]. In the case of the 5S to 7S transitions an optical frequency comb was used to measure the absolute frequencies of the cw-lasers used to excite the transitions [70]. Our study agrees well with this cw-laser based study which was conducted and published about the same time we made our measurements. This provides strong validation of our technique for determining the mode order numbers and thus absolute transition frequencies. Note that all of the reported two-photon transition frequencies, with the exception of $7S_{1/2}F=1$, are via the $5P_{3/2}F=3$ intermediate state. Therefore the 5S to 5P transition is closed and we obtained a better signal to noise than for the $7S_{1/2}F=1$ transition, which was via $5P_{3/2}F=1$.

Transition	Measured Frequency (kHz)	Literature Frequency (kHz)
$5S_{1/2}F=2\rightarrow5D_{5/2}F=2$	770 569 184 527.9 (49.3)	770 569 184 510.4 (16)
$5S_{1/2}F=2\rightarrow5D_{5/2}F=3$	770 569 161 560.5 (11.1)	770 569 161 555.6 (16)
$5S_{1/2}F=2\rightarrow5D_{5/2}F=4$	770 569 132 748.8 (16.8)	770 569 132 732.6 (16)
$5S_{1/2}F=2\rightarrow5D_{3/2}F=3$	770 480 275 633.7 (12.7)	770 480 275 607.6 (10)
$5S_{1/2}F=2\rightarrow5D_{3/2}F=2$	770 480 231 393.9 (38.1)	770 480 231 385.2 (10)
$5S_{1/2}F=2\rightarrow7S_{1/2}F=2$	788 794 768 921.4 (44.5)	788 794 768 878.0 (40)
$5S_{1/2}F=1\rightarrow7S_{1/2}F=1$	788 800 964 199.3 (121.9)	788 800 964 042.0 (40)

Table 4.2: Measured absolute two-photon transition frequencies and comparison to reported values from literature. Note that all of our reported values and fit errors are from the extrapolation to $\sim$0 probing time and power.

4.3.3   Two-Photon Selection Rules

Our measurements of the two-photon transitions from 5S to 7S are particularly well suited for a discussion of two-photon transition selection rules. Previous picosecond [16] and cw-laser based measurements [66] of this two-photon transition did not observe any transition corresponding to $5S_{1/2}$ to $7S_{1/2}$ in which the hyperfine quantum number changed by 1. In other words the only change in total hyperfine quantum number observed was $\Delta F=0$. However, we observed weak $\Delta F=\pm 1$ transitions, and other authors have as well with S-S transitions in Sodium [71]. The explanation of this two-photon selection rule in the literature is rather incomplete. Essentially it amounts to a two-photon transition selection rule that is dependent on the intermediate state detuning, however, no explicit dependence is given. The only observed $\Delta F=\pm 1$ transitions occurred when the two-photon transition was resonantly enhanced via an intermediate state.

A good question is, how does this effective two-photon transition selection rule vary as a function of intermediate state detuning? The answer to this question provides a good example of how to treat two-photon transitions via multiple intermediate states when comb mode pairs are detuned from any intermediate resonance, an important aspect of our experiment in chapter (6).

For the purpose of this explanation we will discuss only excitation by linear polarized light, so we may use q=0 selection rules. It is important to first understand any two-photon transition between 5S and 7S is via an intermediate state, in this case the 5P states need only be considered. In other words, regardless of the intermediate state detuning, this two-photon transition is the sum of several two-photon transition amplitudes via the different intermediate states. Using standard single photon selections rules, in particular $\Delta F=\pm 1,0$, we can determine the possible intermediate states for a transition from $5S_{1/2}F=1$ to $7S_{1/2}=2$ as an

example. Table (4.3) shows the angular part of the reduced dipole moment matrix elements for the first and second step of the two-photon transition as a function of m_F and intermediate state.

Intermediate State	$m_F=-1$	$m_F=0$	$m_F=1$
$5P_{3/2}F=2$	$(\frac{1}{2\sqrt{3}} , \frac{-1}{6})$	$(\frac{1}{3} , 0)$	$(\frac{1}{2\sqrt{3}} , \frac{1}{6})$
$5P_{3/2}F=1$	$(\frac{\sqrt{5}}{6} , \frac{1}{2\sqrt{15}})$	$(0 , \frac{1}{3\sqrt{5}})$	$(\frac{-\sqrt{5}}{6} , \frac{1}{2\sqrt{15}})$
$5P_{1/2}F=2$	$(\frac{-1}{2\sqrt{3}} , \frac{-1}{6})$	$(\frac{-1}{3} , 0)$	$(\frac{-1}{2\sqrt{3}} , \frac{1}{6})$
$5P_{1/2}F=1$	$(\frac{-1}{6} , \frac{1}{2\sqrt{3}})$	$(0 , \frac{1}{3})$	$(\frac{1}{6} , \frac{1}{2\sqrt{3}})$

Table 4.3: Angular part of the reduced dipole moment matrix element for each possible q=0 transition from $5S_{1/2}F=1$ to $7S_{1/2}=2$.

The first term in each parenthesis corresponds to the 5S to 5P part of the transition and the second term to the 5P to 7S step. For any given m_F and intermediate state, the corresponding two-photon transition amplitude goes as the product of dipole moments of each single photon step. The total two-photon transition amplitude can be calculated using these dipole moments and Eq. (3.12) based on second-order perturbation theory. Clearly for the $m_F=0$ transitions, via any intermediate state, this two-photon transition is not allowed. Suppose we only use two-modes to excite this transition, then the two-photon amplitudes due to each intermediate state would be a function of the mode detuning. So for large intermediate state detunings, compared to the $5P_{3/2}F=2$ to $5P_{3/2}F=1$ hyperfine splitting of $\sim$160 MHz, the two-photon transition amplitudes would be weighted equally for both $5P_{3/2}F=2$ and $5P_{3/2}F=1$ transition pathways. The important thing to notice is that for linear polarized light the product of dipole moments for the F=2 and F=1 intermediate states (for either $5P_{1/2}$ or $5P_{3/2}$) are equal and opposite. So the total two-photon transition amplitude is zero due to complete destructive interference. This approach to calculating the total two-photon transition amplitude from $5S_{1/2}F=1$ to $7S_{1/2}=2$ can be used for arbitrary

intermediate state detunings. And of course, if the detuning in comparable to the hyperfine splitting the two-photon amplitude from one intermediate state will be stronger than the other, leading to incomplete destructive interference. Note that the same cancellation occurs for the other possible $\Delta F \neq 0$ transition, $5S_{1/2}F=2$ to $7S_{1/2}=1$.

Although we don't present the dipole moments relevant for circular polarized light, $q=\pm 1$ transitions, a similar cancellation occurs. However, in it is not between hyperfine levels of a particular fine-structure intermediate state, but rather between different fine-structure states. So the cancellation only occurs when the intermediate state detuning is much larger than the 5P fine-structure splitting of 7 THz.

A final interesting observation from this analysis is that a single femtosecond pulse, with a spectrum that does not cover the $5P_{1/2}$ to 7S transition, should not excite any population from $5S_{1/2}F=1$ to $7S_{1/2}=2$. This is somewhat at odds with the idea that the two-photon selection rule is solely a function of detuning. In this case the spectrum is of course equally resonant with both intermediate states, however, the two-photon transition amplitudes via $5P_{3/2}F=2$ and $5P_{3/2}F=1$ should be equal and opposite and still cancel out. Further discussion on two-photon transition selection rules may be found in [72].

4.4   Single Photon DFCS

We have also performed direct frequency comb spectroscopy of single photon transitions in ^{87}Rb. There are some advantages and disadvantages of single photon DFCS relative to our previous two-photon measurements. A significant advantage is that the single photon transition rate is much higher than the two-photon transition rate. Recall in the context of the radiation pressure, subsection (4.2.2), we estimated that the 5S-5P incoherent scattering rate is at least 100 times that

of the 5S to 5D. However, the fluorescence that we measure as our signal is at either 795 nm for the $5P_{1/2}$ states or 780 nm for the $5P_{3/2}$ states. Both of these wavelengths are of course in the bandwidth of the Ti:Sapphire laser, after all that is how we excite the transitions. So we had to alter our data acquisition technique and apparatus to avoid measuring scattered Ti:Sapphire light. The last aspect of the 5P measurements we will discuss is how to use the intermediate state enhancement of a two-photon transition to determine a 5P lineshape and linecenter frequency indirectly.

Similar to our two-photon spectroscopy measurements we still used a 100 Hz MOT cycle. For the first 7.5 ms the trap and repump lasers and magnetic field were on to load and cool atoms in the MOT. For the next 2 ms while the trap magnetic field was turned off the atoms were further cooled using polarization gradient cooling (PGC), meaning the trap laser was attenuated and detuned from the cooling transition. This period of PGC cooling is primarily intended to hold the atoms in optical molasses, the temperature gives rise to negligible Doppler broadening relative the the 5P 6 MHz linewidth. Finally, the atoms are probed and the 780 nm or 795 nm fluorescence counted on a PMT for 0.5 ms, after allowing the the trap and repump lasers to fully extinguish.

We had to use a somewhat more complicated probing cycle for the measurements at 780 nm and 795 nm to avoid saturating the PMT with scattered Ti:Sapphire light. The imaging apparatus before the PMT was modified so that an image of the atom cloud was formed on a ∼1 mm aperture. After the aperture the light was passed through a 3 nm bandwidth optical interference filter centered at the desired detection wavelength, and finally focused onto the PMT. This combination of spectral filtering and imaging helped reduce the amount of scattered Ti:Sapphire light incident on the PMT.

Unfortunately with the design of our MOT chamber there is a lot of scattered

Ti:Sapphire light, so we also have to time gate the data acquisition to avoid saturating the PMT. This was accomplished by using a fast high voltage switching circuit to drive the PMT. The total 0.5 ms data collection window for each MOT cycle was divided into sub-windows of total duration 3.2 μs. Using the Pockels cell to switch the Ti:Sapphire laser we only transmitted the probe light and excited the atoms during the first 200 ns of this sub-window. During the next 400 ns the PMT was switched on and we counted photons as the excited 5P population decayed. Due to the relatively long turn-off time of the PMT the next 2.6 μs was simply a delay before turning on the Ti:Sapphire again. This data acquisition cycle was repeated for the first 200 μs of the 0.5 ms window before the MOT fields were turned back on. A typical signal was the result of repeating this process for hundreds of MOT cycles, or several seconds per point.

Using this direct detection technique we measured the transition frequencies from $5S_{1/2}$F=2 to $5P_{3/2}$F=3 and $5P_{1/2}$F=2. One simplification over the 5S to 5D transition frequency measurements is that we no longer used the slow turn-on LC shutter but rather the Pockels cell to switch the Ti:Sapphire light. So the probe power was constant versus time for all of these measurements. Again using the multichannel SR-430 photon counter we measured the signal versus f_o as we scanned over the transition lineshape. From this data the linecenter was estimated from a Lorentzian fit versus time and the unperturbed linecenter frequency determined by linear extrapolation to $\sim$0 probing time. We measured an absolute transition frequency for the $5S_{1/2}$F=2 to $5P_{3/2}$F=3 transition of 384 228 115 271 (87) kHz. This agrees well with a previously published cw-laser based measurement of 384 228 115 203 (7) kHz in reference [73]. Similarly for the $5S_{1/2}$F=2 to $5P_{1/2}$F=2 transition we measured an absolute frequency of 377 105 206 563 (184) kHz. An improvement from a cw-laser based measurement reporting a value of 377 105 206 705 (400) kHz in reference [74].

4.4.1   5P Measurements via Two-Photon Transitions

In this subsection we present an alternative technique for measuring the 5P lineshapes and center frequencies. Instead of measuring the 5P-5S fluorescence directly we infer the intermediate state lineshape based on changes in the 420 nm fluorescence from the 5D states. Recall that in Eq. (3.12) the two-photon transition amplitude is enhanced as a function of the intermediate state detuning. Therefore if we measure the two-photon transition rate for various intermediate state detunings while maintaining two-photon resonance we can infer information about the intermediate state.

One of the complications of this technique is determining a set of f_r and f_o values corresponding to exact two-photon resonance but with varying intermediate detunings. The second complication was alluded to in subsection (4.2.5) concerning incoherent optical pumping to the off-resonant ground state. Unlike the 5P$_{3/2}$F=3 state, the 5P$_{1/2}$F=2 state population may decay to the off-resonant 5S$_{1/2}$F=1 ground state.

Using our knowledge of the 5P and 5D energy levels we created a list of f_r and f_o pairs corresponding to different intermediate state detunings from 5P$_{3/2}$F=3, but all two-photon resonant with 5D$_{5/2}$F=4, see Table (4.4). We also selected only those combinations of f_r and f_o such that all other intermediate and final states were detuned at least $\sim$2.5 linewidths.

The above set of comb f_r and f_o was used to measure the 5P$_{3/2}$F=3 lineshape via the two-photon transition 5S$_{1/2}$F=2 to 5D$_{5/2}$F=4. Another set of f_r and f_o frequencies were used to measure the 5P$_{1/2}$F=2 lineshape via the two-photon transition 5S$_{1/2}$F=2 to 5D$_{3/2}$F=3.

Initially one may expect that f_r and f_o may be simply scanned together in a smooth fashion to achieve the desired two-photon resonance and intermediate

Detuning (MHz)	f_r (MHz)	f_o (MHz)
-13	99.89260605	-16.4737
-10	99.92066423	-22.4503
-9	99.93474869	-16.2599
-4	99.92482030	-9.9189
-3	99.93890785	-11.1280
-2	99.91518350	-21.3653
+1	99.94325356	-24.2433
+3	99.86747878	-22.2673
+4	99.88155032	-24.0872
+5	99.89562280	-14.1944
+9	99.84803930	-11.4370
+12	99.84303590	-24.3973

Table 4.4: Set of f_r and f_o pairs with varying detunings from the intermediate $5P_{3/2}F=3$ state and two-photon resonant with $5D_{5/2}F=4$.

state detuning. While this is true in a three-level system, it becomes complicated by the many other possible transitions the comb may excite in an actual Rb atom. More specifically, take the $5P_{3/2}F=3$ lineshape measurement as an example. This intermediate state is offset from half the two-photon transition frequency by 1 THz, so considering we use $f_r \sim 100$ MHz, the difference in resonant comb mode order numbers is $\sim 10^4$. So a change of f_r by Δf_r only results in a differential change of frequency between the two resonant modes of $\sim 10^4 \times \Delta f_r$. Suppose that we wish to have a 10 MHz intermediate state detuning, this would require changing f_r by ~ 1 kHz. This change is large enough that the detunings from the many other intermediate and final states will in general change, and may become resonant with other comb modes. It is for this reason extra care must be taken in selecting the values in Table (4.4).

In Chapter (3) we briefly discussed one of our theoretical models based on fourth-order perturbation theory using the Liouville equation. Due to the fact that this model includes all of the 5S, 5P, and 5D states it is ideal for calculating the effects of incoherent optical pumping. In fact, as we will show below,

Figure 4.19: Theoretically predicted population distribution between the two hyperfine ground states for ± 4 MHz detuning from $5P_{3/2}F=3$. Note that the intermediate state detuning was set using values of f_r and f_o to ensure two-photon resonance with $5D_{5/2}F=4$ and reduce excitation to all other transitions.

it is essential for our indirect $5P_{1/2}F=2$ measurement. Figure (4.19) shows the theoretically predicted population distribution between the two hyperfine ground states for ± 4 MHz detuning from the $5P_{3/2}F=3$ state. We expect the majority of the population to be in the $F=2$ ground state initially. From this theoretical prediction we see that there is some optical pumping, due to other intermediate states. However, the amount of population that remains in the $F=2$ state is essentially independent of the $5P_{3/2}F=3$ detuning. Using the set of f_r and f_o pairs shown in Table (4.4) we measured the $5P_{3/2}F=3$ lineshape via its enhancement of the two-photon transition. With this indirect measurement technique we estimated the $5S_{1/2}F=2$ to $5P_{3/2}F=3$ transition frequency to be 384 228 115 309 (63) kHz, within ~ 40 kHz of the frequency measured with the direct single photon technique at 780 nm.

Figure (4.20) shows the same simulation for the resonance with the $5P_{1/2}F=2$ intermediate state. Recall that population in this state may decay to the off-resonant ground state, $5S_{1/2}F=1$. Clearly in this case optical pumping is an important effect, not only does most of the ground state population end up in $F=1$, but it depends on the intermediate state detuning. Note that in both cases the intermediate state detuning was achieved using our predetermine f_r and f_o values, like in Table (4.4). The steady state value of the ground state population distribution is not only determined by the optical pumping rate from $F=2$ to $F=1$, but also the rate for the reverse process, which in general occurs at a different rate. One of the reasons the incoherent optical pumping is different between the ± 4 MHz detuned cases is the optical repumping due to the comb itself from $F=1$ to $F=2$. Of course if there was no optical repumping all the population would eventually end up in the $F=1$ ground state.

Unfortunately the measured $5P_{1/2}F=2$ appears noisy due to the apparently random ground state population distribution for different f_r and f_o pairs. To
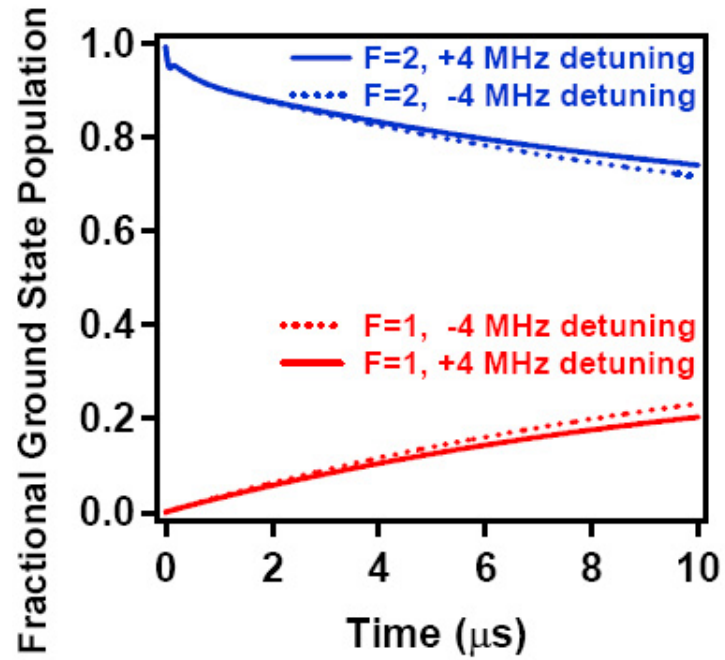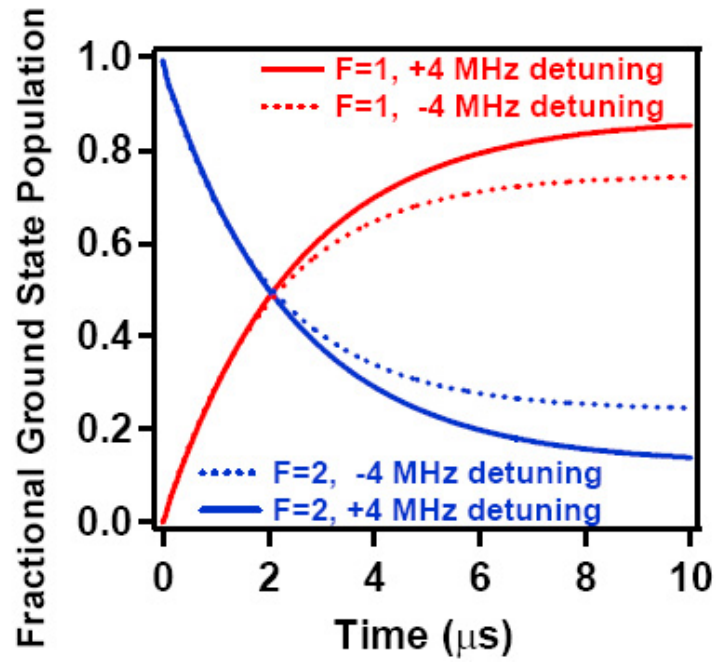
Figure 4.20: Theoretically predicted population distribution between the two hyperfine ground states for ± 4 MHz detuning from $5P_{1/2}F=2$. Note that the intermediate state detuning was set using values of f_r and f_o to ensure two-photon resonance with $5D_{3/2}F=2$ and reduce excitation to all other transitions.

improve the quality of our signal, meaning make the lineshape closer to Lorentzian, we normalized all of our measured $5P_{1/2}F=2$ data. This was done by dividing the signal measured at each intermediate state detuning by the theoretically predicted value of $(1-\rho_{F=1})$, where $\rho_{F=1}$ is the population in the off-resonant ground state $5S_{1/2}F=1$. Note that this is not the same as normalizing by $\rho_{F=2}$ because some population is excited. The raw lineshape measured prior to normalization is shown in Fig. (4.21)(**a**). After applying our normalization scheme the improvement in the Lorentzian fit is quite dramatic, see Fig.(4.21)(**b**). Using the normalized linshape we estimate the $5S_{1/2}F=2$ to $5P_{1/2}F=2$ transition frequency to be 377 105 206 939 (179) MHz, close to the single photon direct measurement. Although this provides an alternative means to measure an intermediate state it is not an improvement over the direct measurement technique applied in the previous section. However, it does provide a remarkable validation of the theoretical model used to calculate the optical pumping effects.
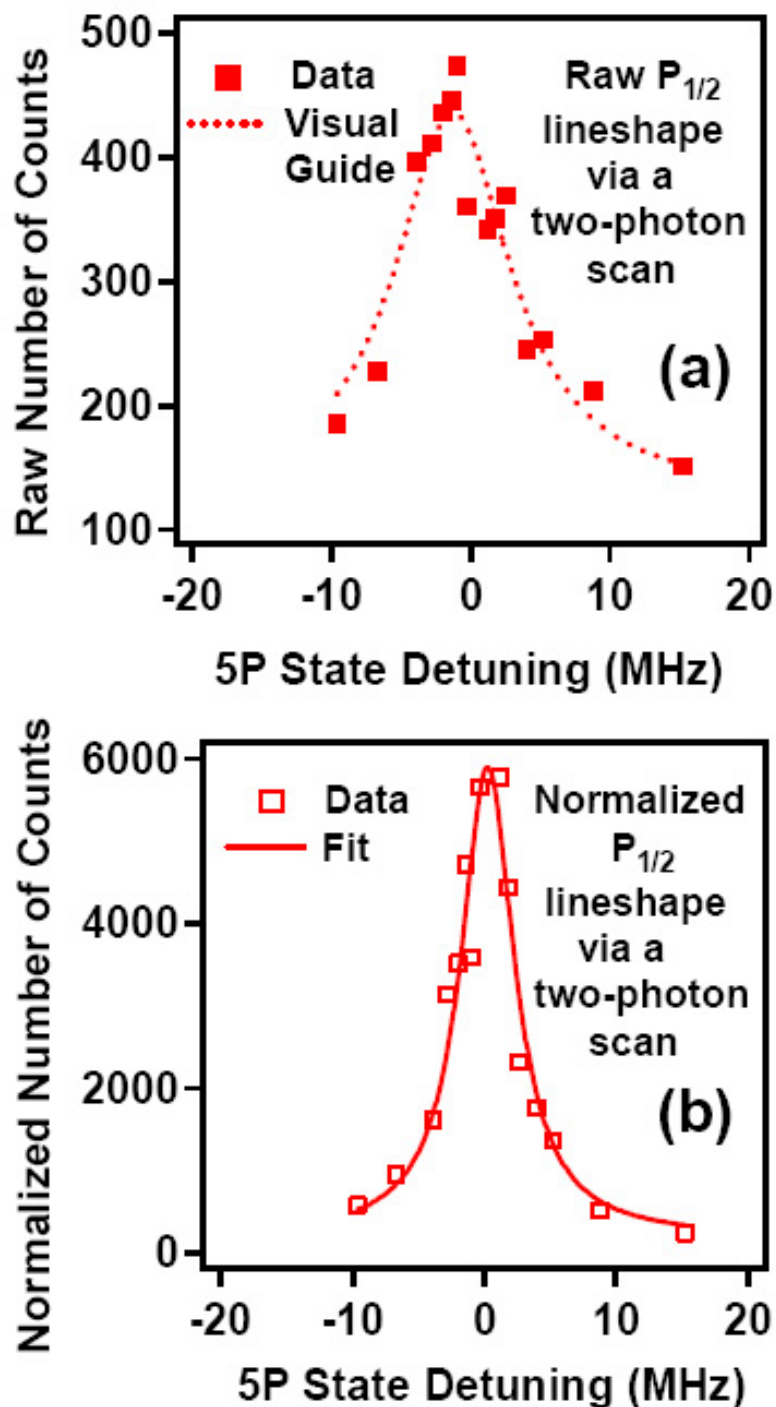
Figure 4.21: (**a**) Raw signal versus intermediate state detuning measured using the 420 nm fluorescence enhancement from the $5D_{3/2}F{=}2$ state. (**b**) Improved lineshape recovered by normalizing the raw data by the theoretically predicted values of $(1\text{-}\rho_{F=1})$ to compensate for the variable optical pumping to the F=1 ground state.

Chapter 5

High-Resolution Coherent Control: Chirp

5.1   Chirped Pulses

A simple non-transform limited pulse shape to consider is a pulse in time-domain with a linear frequency sweep. This means that the instantaneous frequency of the pulse is either increasing or decreasing versus time at a constant rate. Although the time domain definition is intuitively clear, the pulse shaping and atomic physics we wish to discuss are best considered in frequency domain.

We use a frequency domain definition of chirp given be the Taylor expansion of the phase of a Gaussian field envelope pulse about some center frequency. With our convention, changing the chirp of the pulse only changes the quadratic component of the phase in frequency domain, the power spectrum remains unaltered but the temporal duration is increased. The quadratic spectral phase term is given by,

$$\phi'' = \frac{1}{2}\frac{\partial^2 \phi}{\partial \omega^2}|_{\omega=\omega_o} \tag{5.1}$$

where ω_o is the center angular frequency of the pulse spectrum. This term is sometimes also called the group velocity dispersion, usually in the context of material dispersion, because it represents a change of group velocity as a function of frequency. With the given definition of chirp, lower frequencies precede higher frequencies for positive chirp, and vice-versa for negative chirp.

A Gaussian pulse with arbitrary chirp has an electric field given by,

$$E(\omega) = \sqrt{\pi} E_o T_o e^{-(\omega-\omega_o)^2 T_o^2/4} e^{i\phi''(\omega-\omega_o)^2} \tag{5.2}$$

where $2T_o$ is pulse duration defined by the $1/e$ values and E_o is the peak field magnitude of the transform limited pulse. In time domain this field becomes,

$$E(t) = E_o \sqrt{\frac{T_o}{T'}} cos((\omega_o + \alpha t)t + \phi_{ceo}) e^{-t^2/T'^2} \tag{5.3}$$

with

$$T' = T_o \sqrt{1 + (4\phi''^2/T_o^4)} \tag{5.4}$$

and

$$\alpha = \frac{2\phi''}{T_o^4 + 4\phi''^2}. \tag{5.5}$$

It can be seen from Eq.(5.3) that the instantaneous frequency changes at a constant rate given by α, and for either sign of α the chirped pulse duration, T', is greater than the transform limited pulse duration T_o. This expression for the electric field in time domain is used when solving numerically for the density matrix of the atomic system.

5.2   Pulse Stretcher Compressor

To generate pulses with large, tunable linear frequency sweep we use a grating based pulse stretcher and compressor [75]. Typically grating based pulse shapers are used to compress pulses after long travel through dispersive fiber [76] or for reducing the peak intensity of a pulse in a chirped-pulse-amplifier system [77]. In prism and grating based pulse shapers, the vast majority of the dispersion arises due to the angular dispersion, as opposed to the material itself. It was shown in [78] that angular dispersion normally gives rise to negative group-velocity dispersion, but by using a telescope in the pulse shaper it is possible to have both negative and positive dispersion. The large positive and negative

dispersion possible with a telescopic grating-based pulse shaper is ideal for our experiments, which required of order $\pm100,000$ fs^2 chirp.

It is worth going through a brief derivation of the second-order dispersion of a grating pair stretcher/compressor, just to highlight one of the subtleties. As mentioned previously, the second-order dispersion, responsible for the chirp of a pulse, is defined as the second frequency derivative of the optical phase. Therefore we must derive an expression for the phase as a function of frequency. Figure (5.1) shows a diagram of a basic two grating pulse stretcher/compressor with two input rays of the center wavelength λ_o used to approximate a finite width plane wave. There are three lengths defined: L$_{perp}$ is the distance between gratings along the grating perpendicular direction, L$_\lambda$ is the distance traveled by a ray of wavelength λ, and y is the extent of the beam along the second grating.

The total optical phase arises from two parts, the path length defined as ABCD and an extra phase due to phase matching. The grating equation for first order diffraction is,

$$sin(\theta_i) + sin(\theta_r) = \frac{\lambda}{d} \tag{5.6}$$

where the incident θ_i and reflected θ_r angles are defined in Fig. (5.1) and d is the groove spacing. Using the grating equation it is not hard to determine that the wavelength dependent path length ABCD, now defined as l, is

$$l = L_{perp}sec(\theta_r)(1 + cos(\theta_i - \theta_r)). \tag{5.7}$$

The second contribution is due to phase matching, and is somewhat less obvious, for this explanation we must consider two parallel input rays of the same frequency. There are two dashed blue lines perpendicular to the optical rays in Fig.(5.1) that denote the optical phase fronts, or in other words planes of constant phase. Notice that one of the rays must travel further than the other, denoted as the dashed red segments of the ray path. For the phasefronts to be at constant
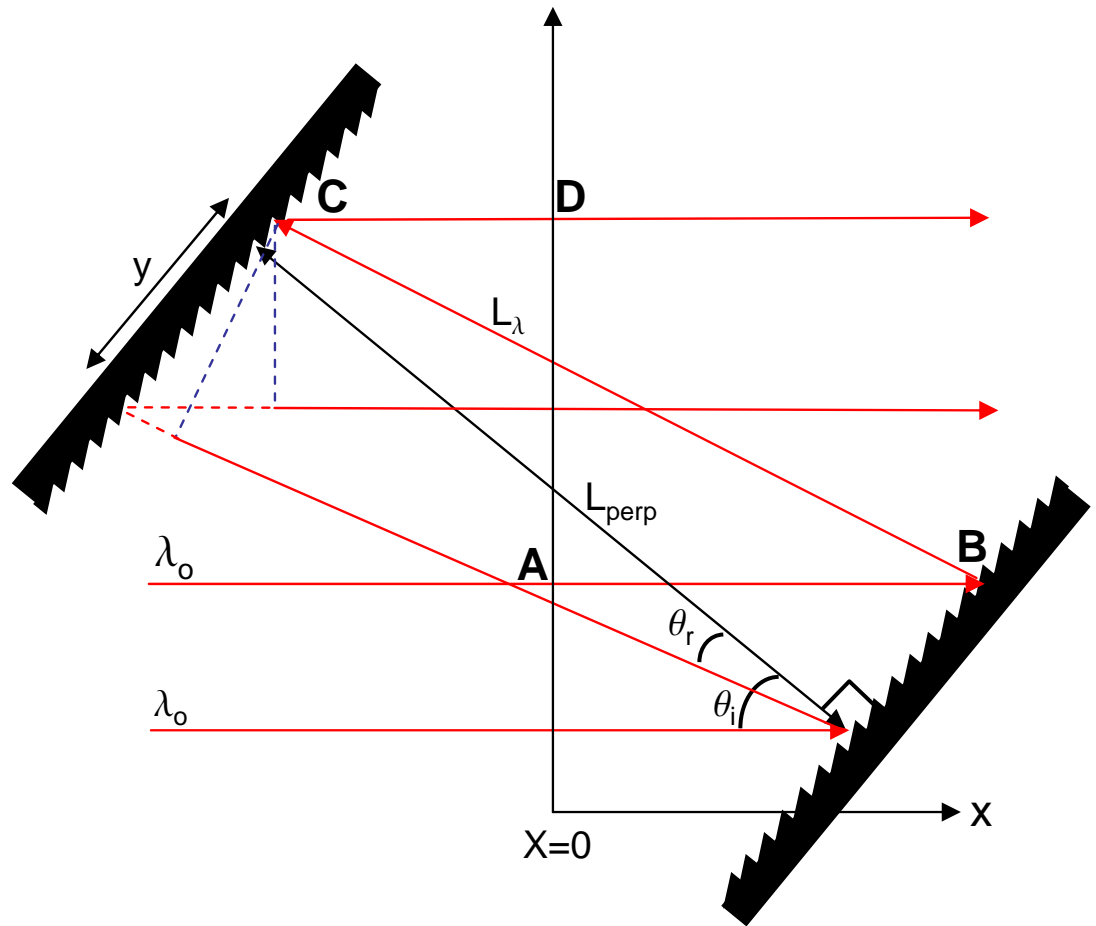
Figure 5.1: Grating pair diagram for the derivation of the second-order dispersion.

phase there must be an extra phase included due to the grating. This extra phase can be determined by calculating the extra path length, given by the two dashed red segments. With some geometry this extra length can be shown to be,

$$l_{extra} = y(sin(\theta_r) + sin(\theta_i)).\tag{5.8}$$

Notice that the previous equation can we rewritten using the grating equation as,

$$\phi_{extra} = 2\pi\frac{y}{d},\tag{5.9}$$

with $\phi_{extra} \equiv 2\pi\frac{l_{extra}}{\lambda}$. This can be interpreted as an extra phase shift of 2π per groove covered on the second grating. Note that due to the fact the beam has not been spectrally dispersed before the first grating, we need to only consider this effect after reflection from the second grating. Combining the results for l and l_{extra} and noting that $y = L_{perp}tan(\theta_r)$ the total phase as a function of frequency can be written as,

$$\phi(\omega) = \frac{\omega L_{perp}sec(\theta_r)(1 + cos(\theta_i - \theta_r))}{c} + 2\pi L_{perp}\frac{tan(\theta_r)}{d}.\tag{5.10}$$

After taking two frequency derivatives, substituting for L_{perp}, the second-order dispersion is found to be,

$$\phi'' = -\frac{4\pi^2 c}{d^2\omega_o^3}\frac{L_{\lambda_o}}{cos(\theta_r)^2}.\tag{5.11}$$

From this formula it can be seen that the chirp is a linear function of displacement L_λ. Further calculations for grating pair pulse effects can be found in the literature for beams of finite size [79], Gaussian beams [80], and distortions due to misalignment [81].

We used a grating with 1400 lines per mm in a folded 2f geometry, see Fig.(5.2). Although the telescope can be used with a magnification of greater than unity to increase the dispersion of the shaper, we used a magnification of unity for the purpose of allowing both signs of chirp. The apparatus was constructed with

Figure 5.2: Double pass grating pulse stretcher / compressor. This figure shows the design used in the our experiments with a telescope of unity magnification.
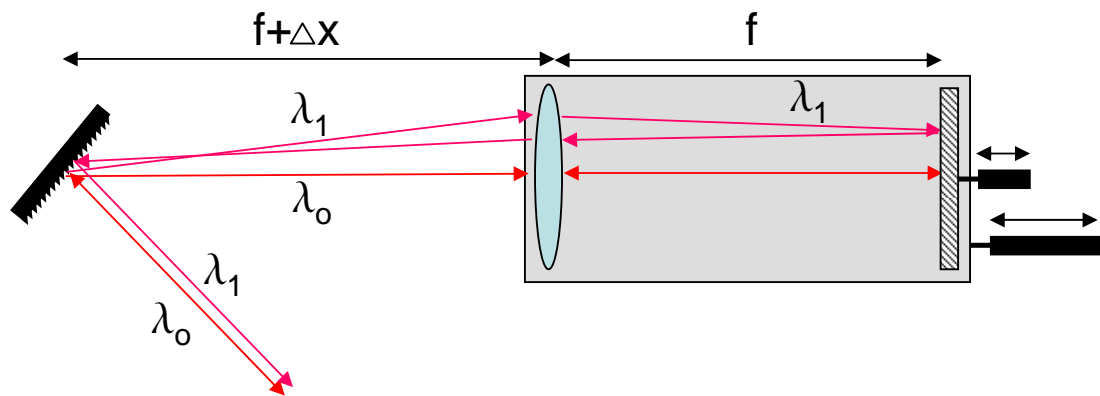
both the lens and the retro-reflection mirror mounted on one rigid platform that could be translated along the optical axis via a long travel micrometer. Using a long focal length lens allows large excursions of the lens+mirror pair from the grating, and thus a large range of $\pm\Delta$x. In this geometry the grating separation L_λ used in Eq. (5.10) must be substituted with Δx [78]. Figure (5.2) illustrates the offset of wavelengths that occurs after one pass through a grating pair. The input ray contains all wavelengths, but the rays corresponding to wavelengths λ_o and λ_1 traverse different paths due to the angular dispersion of the gratings and exit with a spatial offset. Spatial chirp, or wavelength dependent propagation directions, is an issue for our experiments. We focused the Ti:Sapphire beam into the atom cloud, if the modes corresponding to different wavelengths do not overlap well in the focal plane there will be reduced interference in the atomic excitation. Fortunately, the spatial chirp incurred by one pass through the shaper can be canceled out by a second pass. In our case the retro-reflection mirror shown in Fig.(5.2) is tilted slightly such that a pick-off mirror can be used outside the shaper to reflect the beam back for a second pass, note that this also doubles the total dispersion of the pulse stretcher.

For alignment purposes a 3 nm bandwidth optical interference filter was used at 778 nm, the center wavelength of the pulse, before the beam entered the pulse stretcher. The grating was rotated such that the specular reflection directly retro-reflected onto itself, this allows for a reference position to determine the angle of incidence. From this position the grating was then rotated to set the angle of incidence for optimum diffraction efficiency, approximately 90%. To align the grating grooves to the beam polarization the full spectrum of the pulse was used. This is done by ensuring the dispersed spectrum remains horizontal to the table, the grating mount allows for the tilt of the grooves to be adjusted.

The lens plus retro-reflection mirror, both mounted on a rigid platform on

a translation stage, was set such that the center wavelength of 778 nm traveled directly along the optical axis of the lens. The lens and retro-reflection mirror were both mounted on tip-tilt stages such that the 778 nm impinges normally onto the lens and is reflected slightly down from the mirror, allowing the beam to be picked off after one or two passes. A second short travel translation stage was used to mount the retro-reflection mirror, thus allowing fine tuning of the lens to mirror distance to be one focal length. As mentioned previously the beam was sent twice through the pulse stretcher by reflection from a pick-off mirror, to reduce spectral walk-off.

Any residual spatial chirp of the pulse must be reduced. This was accomplished by diverting the full spectrum beam onto a card about 8 meters after two passes through the pulse stretcher. Then the retro-reflection mirror position was adjusted via micrometer until the Ti:Sapphire mode dimmed uniformly as different spectral components were blocked in the fourier plane of the lens. When there is significant spatial chirp a dark line can be observed in the mode, the position of which depends on the color blocked.

Finally the remaining calibration was to determine the necessary grating offset, Δx, to compensate for the dispersion of the optics such that the pulse was transform limited at the atomic sample. For this we optimized the two-photon photocurrent on a GaAsP photodiode. The beam was diverted from the MOT chamber and focussed onto the photodiode. As the distance of the grating from the lens+mirror system was scanned via micrometer a clear peak was observed in the photocurrent corresponding to an approximately transform limited pulse. Note that for this experiment the variations in excited population we observe are on the scale of many thousands of fs^2 chirp, so a rough calibration is sufficient.

5.3 Dressed Atom Picture

The dressed atom picture is a useful tool for visualizing and estimating some of the basic physics involved with chirped pulse excitation of a three-level atom. In the case of large positive chirp the excitation of rubidium by one or more chirped pulses there is a characteristic oscillation of the excited population versus chirp. This characteristic oscillation was the main effect observed in the original single pulse experiments and also appears in our comb experiments. The first period of this oscillation can clearly be seen in our results presented in Fig. (5.5) of section (5.4). Theoretical calculations indicate that it continues beyond the range of chirp used in our experiment, which was limited by our pulse stretcher/compressor.

An intuitive derivation of the rough dependence of the oscillation period, in terms of chirp, can be arrived at from a dressed atom picture. Figure (5.3) shows the dressed energy levels of a three-level atom in a cascade configuration. We are interested in the interference between the two paths indicated by the red dashed arrows in the figure. Both paths start from the ground state before the pulse and end in the excited state after the pulse, however, one path passes through the triangle defined by ABC and the other goes directly from A to C. The path via ABC is said to be diabatic because the state vector passes between two dressed eigenstates, this will be referred to as path i. The other path is adiabatic because the state vector remains in the same dressed state, this will be referred to as path ii. In the actual experiment both paths are traversed simultaneously for the range of chirps and intensity used in our experiment. Clearly the energy of the state-vector changes as a function of laser frequency and thus time. We are interested in the difference in phase acquired, calculated from the energy of the wavefunction, between the two paths.

The dashed lines in Fig. (5.3) represent the dressed levels in the limit of very

weak instantaneous intensity, such that the Rabi frequency between adjacent levels is low and thus the coupling. In the limit of large chirps, this condition of weak coupling is satisfied and the dressed states, indicated by the solid lines, approach the energies given by the dashed lines. In this limit the difference between the two paths is just the triangle ABC. The total phases acquired along the two paths is given by,

$$\phi_i = \int_0^{t'} \omega_i(t)dt \tag{5.12}$$

$$\phi_{ii} = \int_0^{t'} \omega_{ii}(t)dt$$

where t' is the time it takes to sweep the frequency between points A and C, and $\omega_{i,ii}(t)$ is frequency of the wavefunction along path i or ii. Note, $\omega_{ii}(t)$ is constant and equal to ω_2 and that,

$$\omega_i(t) = \omega_2 + \alpha t, \tag{5.13}$$

between times t=0 to t=$\frac{t'}{2}$. The phase difference can be simplified to

$$\Delta\phi = 2\alpha \int_0^{t'/2} tdt. \tag{5.14}$$

As noted previously the rate change of frequency of a Gaussian envelope pulse for large chirps is given by α. The difference in frequency between points A and C is given by δ, the difference in frequency between the first and second transitions. So the time t', is just $\frac{\delta}{\alpha}$. In the limit of large chirps, Eq. (5.5) for the frequency sweep rate gives the relation $\alpha = \frac{1}{2\phi''}$. Using these substitutions and solving for $\Delta\phi = 2\pi$ gives the amount of chirp ϕ'' corresponding to one oscillation period,

$$\phi'' = \frac{4\pi}{\delta^2}. \tag{5.15}$$

So from this rather simple interfering paths argument assisted by the dressed atom picture we arrive at the correct dependence of the characteristic oscillation period on δ.
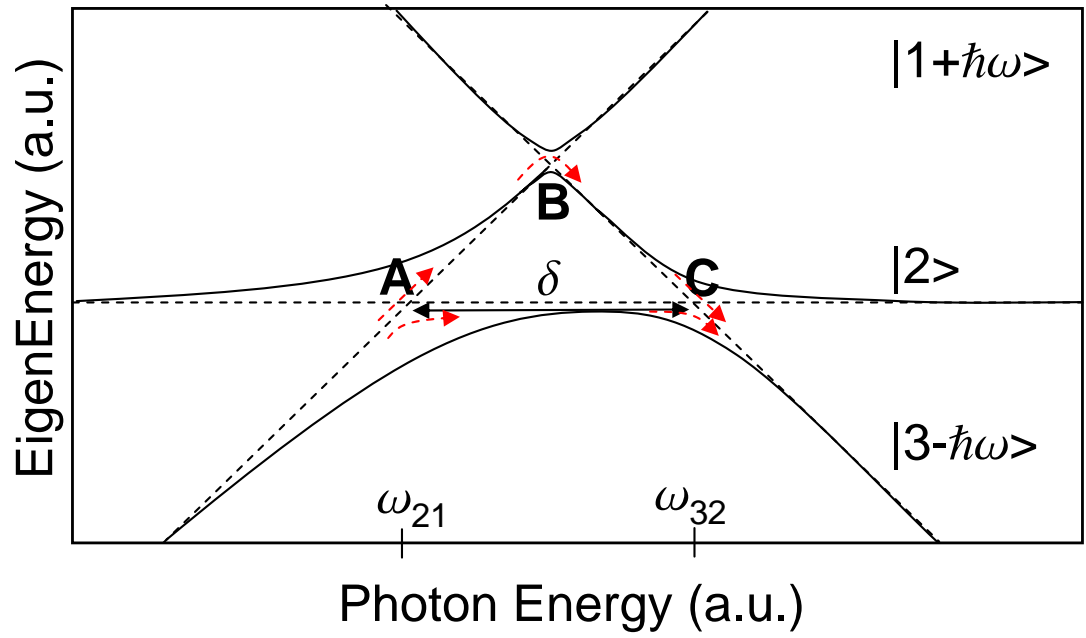
Figure 5.3: Diagram representative of the dressed atom states and the two interfering paths from the ground to excited state.

5.4   Chirped Pulse Experiment

One of the most common and simplest applications of coherent control is called ladder climbing. Ladder climbing refers to the subset of coherent control techniques relying upon a linearly chirped broadband pulse to excite some target state via one or more intermediate states. In general this type of multi-photon transition can be in either a cascade (ladder) type or Raman type configuration, the theory being nearly identical for the two cases. Ladder climbing has found application in molecular systems [82] for dramatically increasing dissociation. Some work has been conducted demonstrating a frequency selectivity much narrower than the bandwidth of the pulse(s) used in the experiment [83, 84]. If the chirp is sufficiently large, and the intensity high, the state vector follows some eigenstate adiabatically, this regime is referred to as adiabatic following [85]. Efficient population transfer in a three-level system can be achieved using two time delayed transform limited pulses, referred to as stimulated Raman adiabatic passage (STIRAP) [86], or a single chirped broadband pulse [87]. At pulse intensities such that adiabatic following is not present the interaction of a single broadband chirped pulse with a three-level system has been studied in rubidium [58], and Sodium [88, 89].

In this section we describe our first experiment demonstrating high-resolution coherent control. This experiment extends the previous work done on chirped pulse excitation of a three-level atom to the multi-pulse regime by using a femtosecond comb. All previous experiments studying the interaction of a shaped femtosecond pulse with an atomic or molecular system have been limited to only a few pulses with temporal separations of much less than a nanosecond. For example, pump probe experiments generally use an optical delay line to generate the time between pulses, significantly limiting the delay. Due to the relatively

long coherence time of the phase stabilized Ti:Sapphire laser we are not limited to short inter-pulse delays. As demonstrated in section (**??**), as long as the interaction between the femtosecond pulse train and the atom electronic states remains coherent the resolution obtained increases versus pulse number. We use this fact to study the effects of a series of linearly chirped pulses with a three-level subsystem of rubidium levels at high-resolution. In particular we excite only the $5S_{1/2}F=2$ to $5P_{3/2}F=3$ to $5D_{5/2}F=4$ cascade transition, see Fig. (5.4), all other allowed transitions are detuned by at least a few linewidths.

Figure (5.4) shows the resonant two comb mode wavelengths at approximately 776 nm and 780 nm and the frequency offset of the intermediate level from exactly half the two-photon transition frequency, we refer to this as δ. The comb was locked with an f_r of 100.41356730 MHz and f_o of 18.14 MHz, which results in the required resonance condition of one comb mode directly resonant with the $5S_{1/2}F=2$ to $5P_{3/2}F=3$ transition and another $5P_{3/2}F=3$ to $5D_{5/2}F=4$. As mentioned in the context of spectroscopy given the two degrees of freedom for the comb frequency spectrum it is possible to satisfy the above resonance condition exactly. Unlike our previous spectroscopy experiments, the entire spectrum of the femtosecond pulse plays a role in this experiment.

Next let us consider the role of the hundreds of thousands of remaining comb modes detuned from an intermediate state. The two-photon transition frequency from $5S_{1/2}F=2$ to $5D_{5/2}F=4$ is $\nu_{2\gamma} = 770.569132733400$ THz. Due to the fact it is a two-photon transition the sum of comb mode frequencies must add to this frequency such that,

$$\nu_{2\gamma} = f_r(N_1 + N_2) + 2f_o \qquad (5.16)$$

where N_1 and N_2 are two integer mode order number of order 4 million. Note that adding a constant quadratic spectral phase to each pulse does not change the
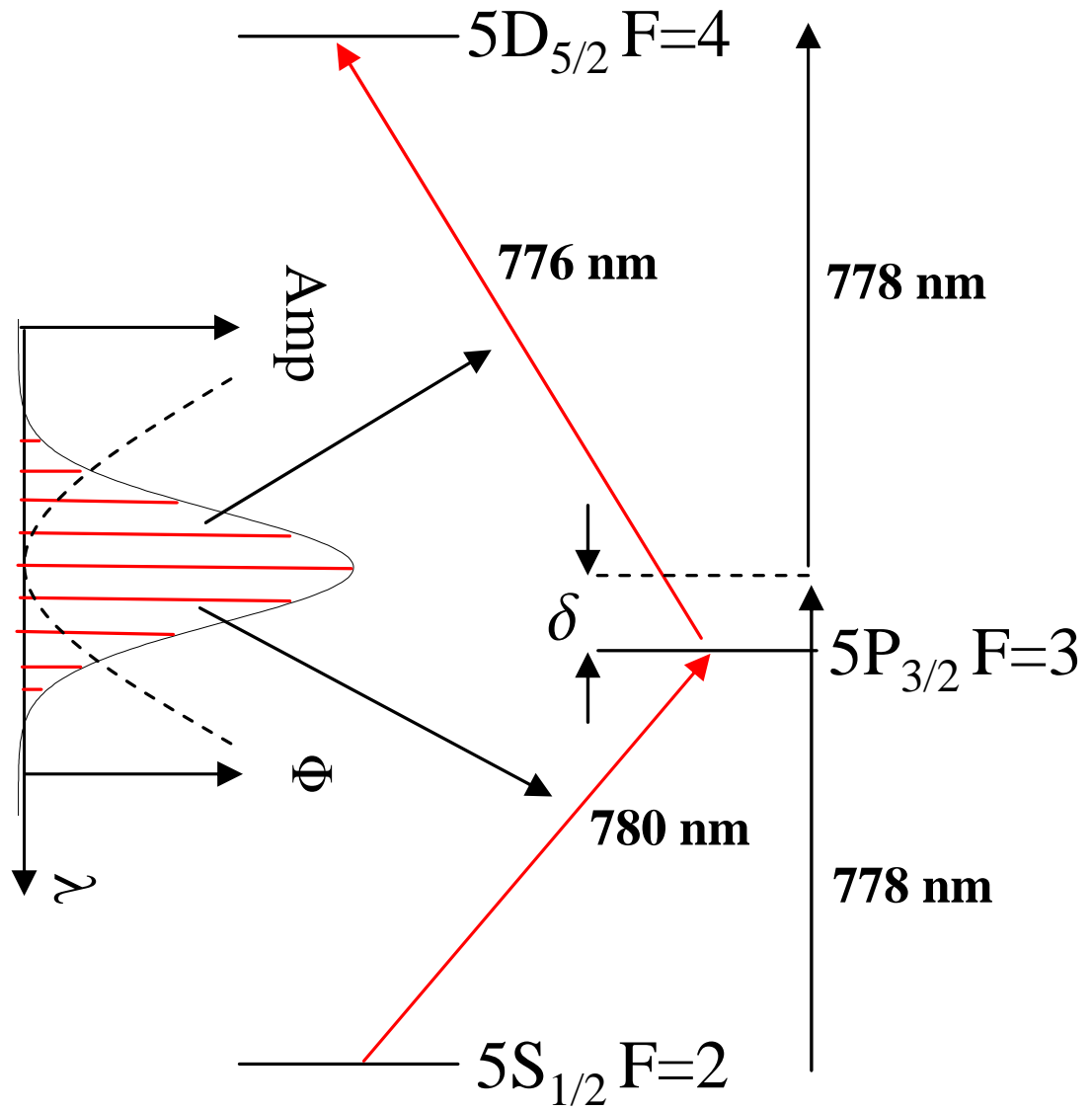
Figure 5.4: Energy level diagram of resonant states for chirped pulse experiment.

frequency spectrum of the comb, only a change in spectral phase as a function of time would modify the spectral content. From this equation it can be seen that if any particular pair of modes add to two-photon resonance then due to the equal spacing of comb modes all modes in the spectrum are part of a resonant pair. In this set of chirped excitation experiments the spectrum was approximated as Gaussian with a FWHM of 30 nm centered at 778 nm. This results in roughly a 15 THz FWHM spectral width supporting approximately 150,000 comb modes. If we take each separate possible two-photon transition amplitude to be from an ordered pair of modes there are ∼300,000 two-photon resonant transition amplitudes within the FWHM of the comb spectrum.

Each two-photon resonant transition amplitude is proportional to,

$$C_{N_1, N_2} \propto \frac{|E_{N_1}||E_{N_2}|e^{i(\phi_{N_1} + \phi_{N_2})}}{i(\omega_{gf} - 2\pi(N_1 + N_2)f_r - 4\pi f_o) + \pi\Delta\nu_f} \times \qquad (5.17)$$
$$\frac{1}{i(\omega_{gi} - 2\pi(N_1)f_r - 2\pi f_o) + \pi\Delta\nu_i}$$

where $|E_{N_{(1,2)}}|$ and $\phi_{N_{1,2}}$ are the magnitude and phase of the N_1 and N_2 modes, $\omega_{gf}(\omega_{gi})$ are the transition frequencies from ground to final(intermediate) states, and $\Delta\nu_{i(f)}$ are the intermediate(final) state linewidths. Note that this simplified form of the equation is for the N_1 mode from the ground state, i.e. it constitutes the first step in a specific ordering of absorption. The other possible ordering has N_2 exciting the 5S to 5P transition. The full formula is not necessary to explain the relevant physics for this section.

Inspection of Eq. (5.17) reveals that the phase of the excited state amplitude is a function of the phases of the two modes and also the detuning from intermediate state resonance. In particular we notice that for a transform limited pulse, if the frequency of the N_1 mode is much less(greater) than ω_{gi} the phase of the amplitude is -90°(+90°). The nearest mode pairs off-resonant from the intermediate state are detuned by $\pm f_r$ ∼100 MHz, for a transform limited pulse these

give rise to transition amplitudes of equal magnitude but $\sim180^o$ out of phase and therefore destructively interfere. All other modes are detuned further than 100 MHz from the intermediate state and therefore give rise to two-photon amplitudes with a phase of $\pm90^o$ as well. Altering the spectral phase from that of a transform limited pulse (constant phase) by introducing chirp, changes the phases of the two-photon amplitudes corresponding to different wavelengths.

Due to the fact the spectrum is centered at 778 nm, close to the $5S_{1/2}F=2$ to $5P_{3/2}F=3$ transition wavelength of 780 nm, it is a good approximation to say that for a transform limited pulse all mode pairs detuned from the intermediate resonance completely destructively interfere. Of course there is a second reason why the mode pairs detuned from an intermediate resonance can be ignored to a first approximation. The second term in Eq. (5.17) predicts the amount of resonant enhancement of the two-photon transition as a function of intermediate state detuning. So any mode pair detuned from the intermediate state has a greatly diminished amplitude compared to the intermediate state resonant transition amplitude.

In this chirped excitation experiment we are interested in the effect of the hundreds of thousands of mode pairs detuned from intermediate resonance. The experimental apparatus used in the section is very similar to that of the spectroscopy experiments. In particular the Pockels cell is used as a pulse picker in the same manner as section (4.1). As mentioned previously the Ti:Sapphire is operated with a spectral width of approximately 30 nm FWHM, at a center wavelength of 778 nm, resulting a transform limited pulse duration of about 80 fs. The average power at the MOT was measured to be approximately 55 mW. This beam was focused into the MOT, from one direction only, to a beam waist estimated to be about 160 μm. The peak transform limited electric field resulting from these beam parameters is approximately 1.3×10^7 V/m.

The MOT was operated in 10 ms cycles like our previous experiments. It was loaded for the first 7 ms, then the trapping and repump lasers and magnetic field were turned off for the remaining 3 ms. In the last 200 μs the atoms were probed with the Ti:Sapphire laser. Due to the fact the atoms were probed from one direction only there is a significant momentum transfer to the atoms. We only probed the atoms from one direction because we want all the atoms to be excited by the same exact pulse shape. We will discuss the effect of counter-propagating pulses in the context of coherent control in section (6.1). For this reason the data was collected during only the first 80 μs of the 200 μs window. This 80 μs was divided into two windows of equal 40 μs duration. During the first 40 μs the atoms were excited by the Ti:Sapphire laser that passes through the Pockels cell and the pulse stretcher, this is the chirped beam. During the second 40 μs window the Pockels cell is in the off position, during this time the Ti:Sapphire laser is diverted out the side exit of the cell and bypasses the pulse stretcher. This diverted beam is chirped from the Pockels cell and general optics, but remains at constant chirp throughout the experiment. We used this constant chirp beam as a reference to reduce the effect of MOT atom number fluctuations during the data collection process. Using a SR-400 two-channel photon counter we were able to normalize the counts taken on channel A during the first 40 μs to those taken on channel B during the second 40 μs. Each data point was taken at a set displacement of the lens and retro-reflection mirror, Δx in Fig. (5.2), and is the sum of 20,000 MOT cycles, 200 s of operation time, or 0.8 s of atom interrogation time.

The main result of this experiment is presented in Fig. (5.5). We scanned the displacement, Δx, of the pulse stretcher from 22 mm to -33 mm. Using Eq. (5.10) for the dispersion of a single pass through the stretcher and multiplying by

two for double pass we get the dispersion per unit Δx,

$$\phi''(\Delta x) = -6.774 \times 10^6 \Delta x. \quad [fs^2] \qquad (5.18)$$

This range of displacements gives -150,000 to 225,000 fs^2 chirp, enough to observe the characteristic oscillation. Figure (5.5) shows a theoretical calculation (red lines) for both the single pulse response (not to scale) and the asymptotic steady state $5D_{5/2}F=4$ population versus chirp. The measured signal is shown as open squares and has been scaled to the theoretically predicted population by one global scale factor that takes into account things such as photon collection efficiency and atom number. Although the dressed state approach and second-order perturbation theory yield useful information about the physics, the theory model used here is based on solving for the density matrix of the three-level system. In particular we solve for the density matrix of the system numerically as outlined in section (3.2) of chapter (3) for a series of linearly chirped femtosecond pulses.

There are two main features of the data in Fig. (5.5) that separate our comb experiment from previous single pulse experiments. The first of which is the large difference in the excited population between one pulse and 100 pulses for negative chirps. Intuitively the very low population predicted for a single negatively chirped pulse can be understood from the order of frequencies that arrive at the atom.

For a rubidium atom the 5S to 5P wavelength is less than that of the 5P to 5D wavelength. Initially the electron is in the $5S_{1/2}F=2$ ground state, with no probability to be in the 5P states. So the natural time ordering of wavelengths to excite an electron from 5S to 5P then 5D, is longer to shorter (positive chirp). In fact that is exactly what previous experiments in Na and Rb found for single pulse excitation [88, 58]. If the intermediate level lies above the two-photon half frequency then the ordering would need to be reversed.
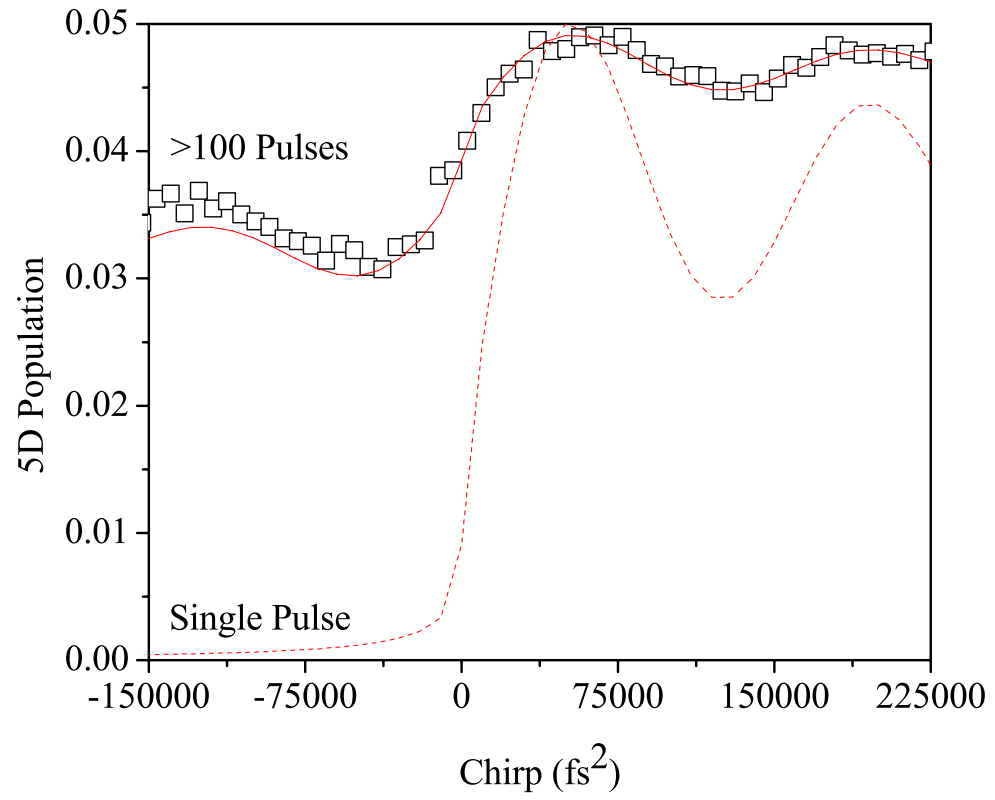
Figure 5.5: Steady state measured signal and calculated excited state population versus chirp and the single pulse theoretical response.

Coherent excitation by multiple pulses, like in our experiment, results in a significant 5D population at negative chirps. Initially we did not expect this result. However, after some thought this is a nice example of how coherent interaction with a chirped comb differs from a single pulse. This effect is due to the $5S_{1/2}F=2$-$5P_{3/2}F=3$ electronic coherence that persists between pulses, with a coherence time of about 50 ns. This coherence essentially ties together the electric field from several pulses. So despite the fact individually the pulses are chirped from short to long wavelengths, between the end of the first pulse and the beginning of the second the field jumps from long to short wavelengths. This inter-pulse frequency jump is similar to a positively chirped field, and is therefore capable of exciting the 5S to 5P to 5D transition in the proper time ordering. To demonstrate this effect we measured the 5D population versus the number of femtosecond pulses at $\pm$ 67,000 fs^2 chirp. Our results are shown in Fig. (5.6) starting from a single pulse excitation by 1 to 9 pulses. The theoretical predictions are the lines through the data points, which are shown as symbols. At both large positive and negative chirps the population grows as the square of the number of pulses, a signature of coherent accumulation. However, the scale factor for the negative chirp results is less population transfer than that of the positive. Unfortunately the single pulse signal is dominated by noise so the single pulse versus two pulse response does not show the dramatic increase expected from theory.

The second feature of significance is indicative of the high-resolution obtained in our experiment. Recall that the oscillation of the excited population is predicted to occur with a period of $\frac{2\pi}{\delta^2}$. Where δ is the detuning of the intermediate state from half of the two-photon transition frequency. In previous single pulse experiments there are two main sets of intermediate states due to the fine structure splitting, for example the 5P states in Rb. Excitation of Rb by a single pulse will result in population transfer to both the $5D_{3/2}$ and $5D_{5/2}$ excited states.
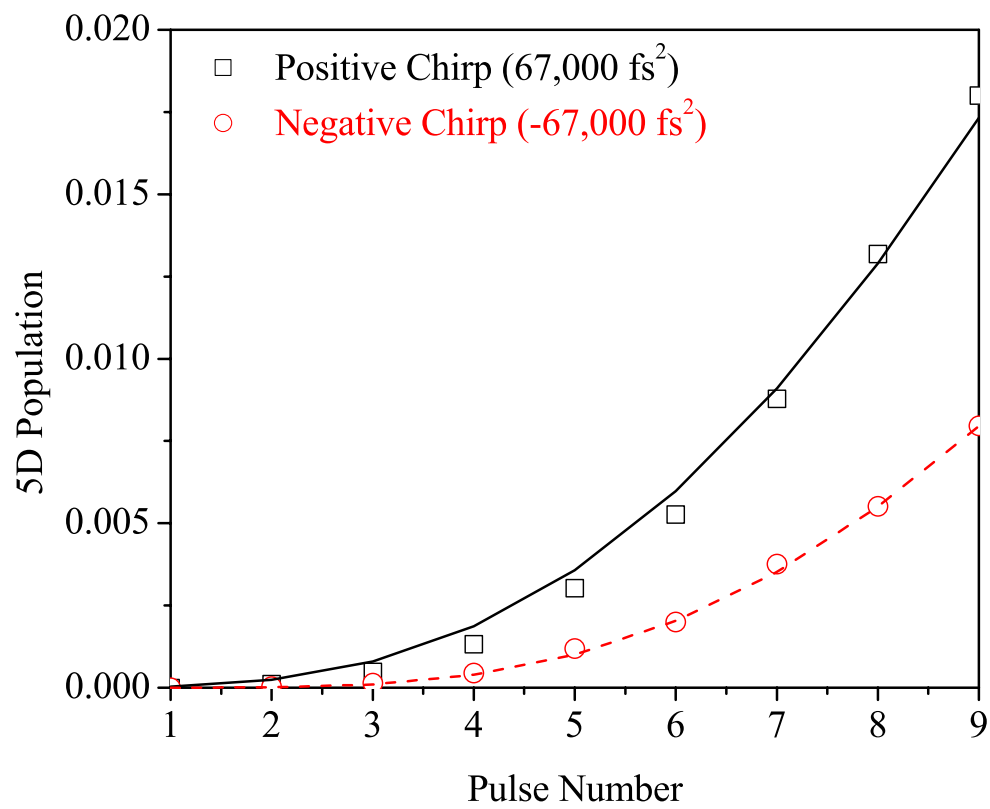
Figure 5.6: Measured signal and calculated excited state population versus pulse number for large positive and negative chirps.

The $5D_{3/2}$ excited state manifold is accessible via both the $5P_{1/2}$ and $5P_{3/2}$ states. These two sets of intermediate states have very different detunings from half the two-photon transition frequency. The $5P_{3/2}$ states have detunings, δ, in the range of 1 THz and the $5P_{1/2}$ states have much larger 7 THz detunings. Therefore it is expected that there should be two different periods for the oscillation of 5D population versus chirp, these different periods were observed in the Sodium single pulse experiment [88]. The high-resolution of the comb allows us to tune to specific transition pathways. In this particular experiment we chose the $5S_{1/2}F=2$ to $5P_{3/2}F=3$ to $5D_{5/2}F=4$ transition. Nearly all of the measured signal can then be attributed to population solely in the $5D_{5/2}F=4$ state, which is only accessible from the $5P_{3/2}F=3$ intermediate state. We measured an oscillation period of $\phi''_{2\pi}=14.5\times10^4$ fs^2, very close to the theoretical value of $\phi''_{2\pi}=14.3\times10^4$ fs^2. Note that if transitions via the $5P_{1/2}$ states contributed to the signal, there would also be a much shorter oscillation period of $\phi''_{2\pi}=2.4\times10^3$ superposed on the result.

To further demonstrate the capability of using a comb for high-resolution coherent control we conducted a final chirped pulse experiment in which we significantly reduced the nonlinear absorption. As explained previously the phase dependence as a function of intermediate state detuning predicted by Eq. (5.17) results in destructive interference. Specifically, recall that for a transform limited pulse the two-photon amplitude from a comb pair detuned below an intermediate state is canceled by an equal and opposite amplitude from a pair detuned symmetrically above the intermediate state. This prediction is especially valid for our choice of two-photon transition, $5S_{1/2}F=2$ to $5P_{3/2}F=3$ to $5D_{5/2}F=4$. As was discussed in section (4.1) this transition has a closed excitation pathway and is therefore a reasonable approximation to a three-level system, if we can ignore the m_F sublevels. So for a transform limited pulse all of the excitation is essentially due to only those two modes that are exactly resonant with a transition step. In

this experiment we demonstrate phase sensitive cancellation of the excited state population due to this interference effect.

By shifting the offset frequency f_o of the comb by $-f_r/2$ to -31.86 MHz, two-photon resonance is maintained, but there is no mode resonant from $5S_{1/2}F=2$ to $5P_{3/2}F=3$. All mode pairs are symmetrically detuned around the intermediate resonance by $f_r \times (1/2 + N)$, where N is an integer from zero. Figure (5.7) shows the resulting 5D population as a function of chirp between the range of about -75,000 to 150,000 fs^2. Like our previous chirped excitation results the theoretically predicted value is shown as a solid red line and the measured data points are symbols. The figure inset is a diagram depicting the detuning of comb mode pairs that are two-photon resonant but symmetrically detuned around $5P_{3/2}F=3$. There are two reasons why the signal is reduced in this experiment from our previous chirped excitation results shown in Fig. (5.5). First and foremost, is that the resonant enhancement of the two-photon transition is significantly reduced. For example, the ratio of the resonant enhancement from a mode pair directly on resonance to that of a mode pair detuned by 100 MHz is about 1000. The second reason for a reduction in the signal is the phase sensitive cancellation we are interested in demonstrating. From Fig. (5.7) it can be seen that by changing from zero to about 25,000 fs^2 the signal is increased five fold, a clear signature of the phase sensitive destructive interference.
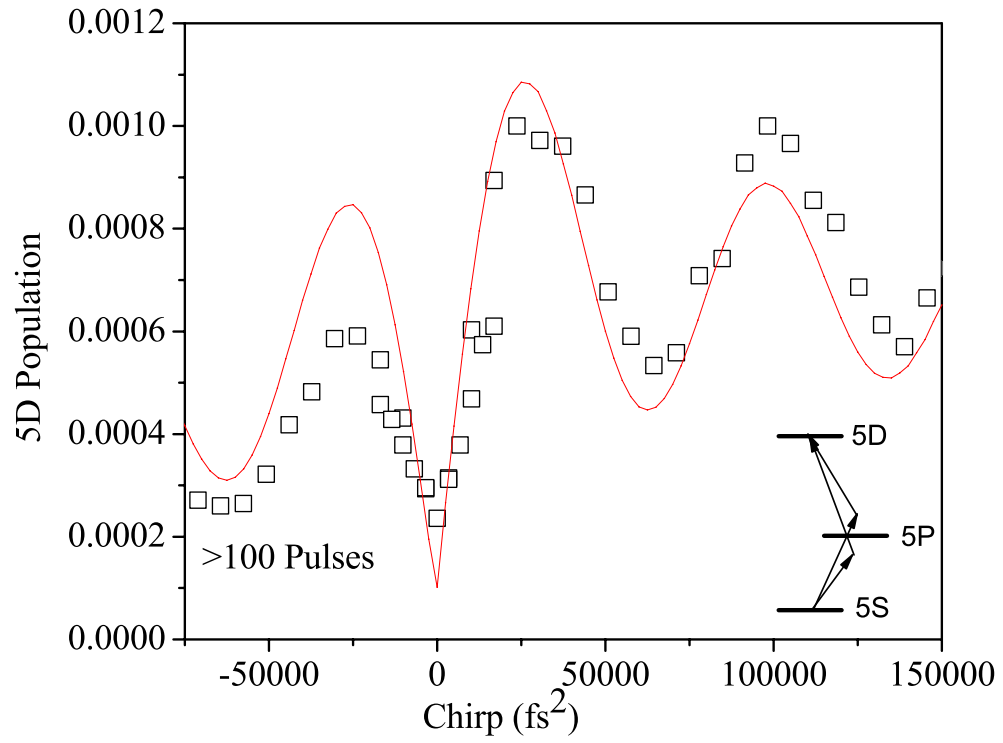
Figure 5.7: Steady state measured signal and calculated excited state population versus chirp for a comb tuned symmetrically about the intermediate state resonance.

Chapter 6

High-Resolution Coherent Control: Discrete Phase

6.1   Spatial Light Modulator Pulse Shaping

In this section the design and operation of the spatial light modulator (SLM) based pulse shaper is described. There are several crucial calibrations that must be conducted on both the SLM itself and the pulse shaper as a whole. It should be noted that these calibrations greatly influenced the results of our coherent control experiment. Although mundane, and perhaps obvious to some, the alignment and calibration procedures presented in this section constitute a great deal of the the necessary considerations for obtaining high quality coherent control results.

The design of our SLM based pulse shaper is shown in Fig. (6.1). It is based on a folded 2f-2f configuration with the SLM liquid crystal element at the Fourier plane. There are four optical elements shown on each side of the pulse shaper in Fig. (6.1). There is a flat mirror used to divert the beam to the grating, this mirror is on a removable mount such that the beam can pass directly though two irises for alignment. A 1200 grooves per mm grating is used to diffract the light to a pickoff mirror. The pickoff mirror is used to fold the optical path, this saves space and allows the grating to be adjusted for its optimum diffraction efficiency. Light is reflected from the pickoff mirror to the spherical mirror with a focal length of 25 cm, used to focus into the SLM. There is a f/2 length distance between the grating and pickoff mirror, f/2 distance from the pickoff mirror to spherical mirror,

and one focal length from the spherical mirror to the center of the SLM element. Before the pulse shaper we used a telescope to expand the Ti:Sapphire beam to approximately 3.5 mm diameter, resulting in a beam radius in the Fourier plane of about 30 μm. Ideally the spacing and angles of the elements on either side of the SLM are equal. Note that the grating, spherical mirror, and SLM are all mounted on micrometer translation stages for fine tuning.

6.1.1   Alignment Procedure

Proper alignment of the pulse shaper optics is essential for ensuring that the beam exiting the shaper has as little spatial chirp as possible. Although it is in principle simple to set the distances and angles of the optics on either side of the SLM to be equal, in practice this proves to be more difficult. Even with careful measurements of all the distances and beam heights, after the initial alignment, I found the beam exiting the pulse shaper to generally have a significant amount of spatial chirp and astigmatism. So it is useful, to explain the alignment procedure we used.

There are two alignment irises mounted on the same optical breadboard as the pulse shaper at equal heights. The first step is to ensure the input beam is aligned to these irises without passing through the pulse shaper. This is done by removing the two flat input/output mirrors. Next replace the flat mirrors, the first mirror is angled to direct the beam to the grating with a shallow downward slope, such that the beam is diffracted at the same angle to the pickoff mirror, but not clipped by the mirror.

For this part of the alignment it is best to aperture the input beam to a small diameter and filter the center wavelength with an optical interference filter. The grating rotation angle should be adjusted such that the diffracted beam is almost reflected back on itself, but tilted slightly down such that the full, unapertured
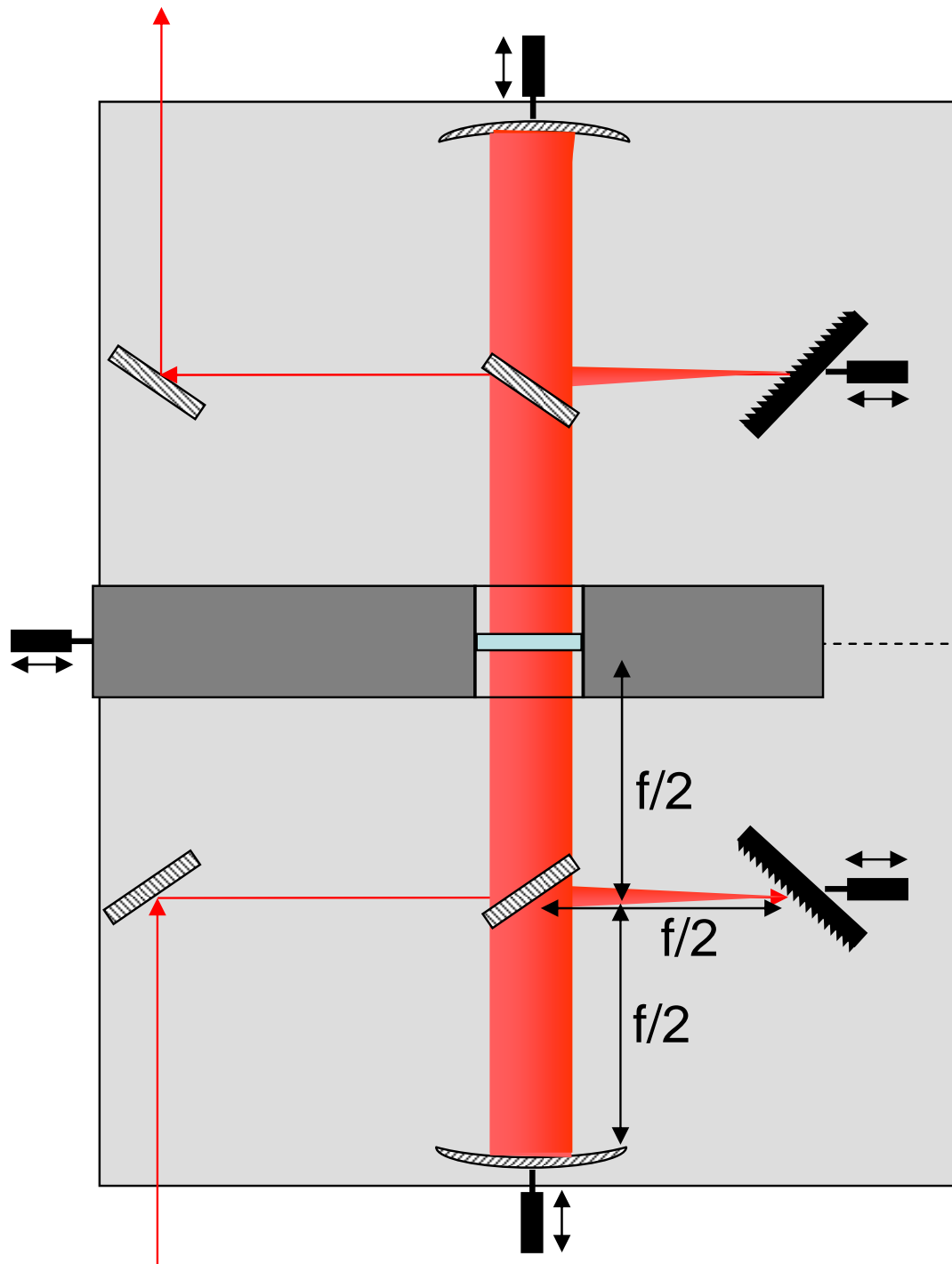
Figure 6.1: Spatial light modulator in a folded 2f-2f geometry pulse shaper. The input beam is expanded prior to entering the pulse shaper to ~3.5 mm diameter, however it is shown as a thin line. The broad line represents the spectrally dispersed beam after the grating. The dispersed beam is picked-off with a mirror and diverted to the spherical mirror to focus into the SLM elements. Note that the pick-off mirrors are below the beam sent to the SLM.

mode, is incident on the center of the pickoff mirror. If this is done properly the full mode will not be clipped by the pickoff mirror, but all vertical angles are kept to a minimum. The pickoff mirror is aligned to reflect the beam 90° in the horizontal plane and vertically upward such that the beam hits the spherical mirror at the the same height as the input beam at the first iris. The spherical mirror should be angled slightly upwards such that the beam after reflection is parallel with the table.

At this point the SLM position can be roughly adjusted so that liquid crystal elements are in the focus of the beam and roughly centered such that pixel number $\sim$160 corresponds to the center wavelength. It is normal for the full spectrum at the SLM to be rotated about the propagation direction such that each wavelength is at a slightly different height, this is due to the different heights at which the wavelengths are reflected from the pickoff mirror. One half of the shaper should be roughly aligned after this procedure and the output half can be aligned in the same fashion to be a mirror image.

After the previous rough alignment is completed the beam should exit the pulse shaper at a fixed height through the alignment iris. Assuming all the distances were initially set properly the interference filtered beam should be collimated, if it is not the second spherical mirror should be adjusted via micrometer.

The final step in the pulse shaper alignment is to reduce the spatial chirp of the output mode. This is best accomplished by walking the vertical and horizontal angles of the second grating and pickoff mirrors with the full spectrum passing through the shaper. To assist in this step and fine tune the spatial chirp it is very useful to observe the mode via a CCD camera in the focus of a lens. We simply picked off the beam after the lens used to focus into the MOT and diverted it to a camera. The idea is to walk the vertical and horizontal angles of the second pickoff mirror and grating, it may be necessary to adjust the last flat mirror to

ensure the beam exits the center of the iris. With this adjustment combination it should be possible to obtain a Gaussian mode on the CCD. Prior to alignment it generally appears as a larger rotated ellipsoid due to astigmatism.

Once a small round spot is obtained, check for spatial chirp by blocking narrow spectral regions directly in front of the SLM. For example, as a screwdriver is passed through the spectrum generally a tilted dark line will appear on the camera, this is due to spatial chirp. Using the same degrees of freedom it should be possible to make the entire mode on the camera dim uniformly as different spectral regions are blocked, meaning all wavelengths focus to approximately the same spot. Although we never tried this idea, it might be best to use a frame grabber with the camera and check the overlap of the modes corresponding to different wavelengths. This could be done using the SLM directly between crossed polarizers to select different spectral regions.

6.1.2 Calibration Procedure

We used a Jenoptik SLM-S320 SLM with a near-IR anti-reflection coating in our pulse shaper. This SLM consists of 320 separately addressable liquid crystal elements. Each element is a a rectangle of 97 μm width and 13 mm height. There is a gap between each element of 3 μm width, in this region there is always a constant phase retardation. Both the input and exit faces of each liquid crystal element are coated with thin optically transparent electrodes. When there is no voltage applied to the electrodes the liquid crystals are all aligned vertically, meaning the long crystal axis is vertical. Under an applied voltage these crystals rotate, the higher the applied electric field the more they align to the DC electric field direction. This rotation causes a change in birefringence of the crystal, and thus a change in the phase retardation a vertically polarized optical field experiences. There are two voltage operating ranges for the SLM voltage, low is from 0 to 5

volts and high is 0 to 8 volts. Each voltage range is divided into 4096 steps called the voltage count, so 0 to 4095 voltage count covers the entire range. Within just the low range the phase retardation may be varied approximately 12 radians over the entire spectral width of our pulses, however, 2π radians is of course sufficient. So we set the SLM, via software, to the low range for our experiments to give a higher phase step resolution.

In the alignment section the SLM position was roughly adjusted such that the middle of the pixels corresponds to the center of the Ti:Sapphire spectrum. Next we use the repump laser to align the position of pixel 160 (middle pixel) with respect to the input beam spectrum. The repump laser is conveniently locked to the ^{87}Rb $5S_{1/2}F{=}1$ to $5P_{3/2}F{=}2$ transition at approximately 780.25 nm, so it serves as a frequency reference. For this calibration the repump laser was diverted into the pulse shaper colinearly with the Ti:Sapphire. It is not necessary to mode match the two lasers, the repump laser need only be collimated and have a diameter large enough that the focal spot is ideally less than a pixel width.

Although normally the SLM is operated as a phase mask with no wavelength dependent attenuation, it is possible to use the voltage controlled birefringence to operate as amplitude mask. This is done simply by placing crossed polarizers around the SLM element, one at $+45^o$ with respect to vertical and the other at -45°. Note that the polarizers should be placed directly before and after the SLM to avoid any polarization rotation due to reflections from other optics. The transmitted repump laser power is monitored on a power meter at any point after the second polarizer, and the Ti:Sapphire is blocked for this calibration.

Using a simple LabVIEW program written for this purpose the phase of a variable width region of the SLM pixels can be controlled. It is generally best to determine the voltage counts corresponding to maximum transmission and attenuation by setting all pixels to a uniform voltage, this will determine the

best case scenario for operating the entire SLM as an on/off switch. Once these voltages are known a narrow region of the mask around pixel 160, for example pixels 145-175, should be set to attenuate while all other pixels set to transmit. By repeatedly adjusting the SLM position via the micrometer and reducing the width of the attenuating region the majority of the repump power can be blocked by only pixel number 160. This procedure allows one to determine that pixel number 160 corresponds to a wavelength of 780.25 nm.

The position of the SLM with respect to the focal plane of the spherical mirror is not yet calibrated. There are two ways to do this, either by adjusting the SLM distance from the spherical mirror by hand or adjusting the mirror via micrometer. Generally it was sufficient to adjust the SLM position by hand, this also avoids misalignment of the pulse shaper when adjusting the mirror position. When the SLM is positioned at the focus of the spherical mirror the attenuation will be maximum, because more of the focused repump laser mode fits on pixel number 160. It may be necessary to do one more iteration of the previous calibration to ensure that pixel 160 still corresponds to 780.25 nm after the SLM has been moved by hand.

One of the most important calibrations is to determine the phase retardation versus voltage count at the operating wavelength. The manufacturer provides this data measured at a wavelength of 633 nm. I feel it is necessary to point out for future users of this SLM that the operating manual states the phase retardation at any wavelength is calculable given the measurement data at 633 nm. The argument proceeds as follows. Clearly for a given index of refraction different wavelengths have varying retardations given by,

$$\Delta\phi(V, \lambda) = \frac{2\pi d}{\lambda} \Delta n(V, \lambda) \tag{6.1}$$

where V is the voltage applied to the pixel that wavelength λ passes through,

and d is the thickness of the liquid crystal element, 10 μm in our case. The ITO electrodes, glass plates, and anti-reflection coating of course cause an extra phase retardation, however, it is constant versus voltage. The manufacturer claims the birefringence of the crystal has approximately constant wavelength dependence, so the change in refractive index may be rewritten as,

$$\Delta n(V, \lambda) = \Delta n(\lambda) f(V) \tag{6.2}$$

where the function $f(V)$ contains all the voltage dependence. At a voltage of 0 all the liquid crystals are oriented vertically and the resulting refractive index is a maximum, at this voltage $f(V)$ is taken to be unity. From measurements of the index of refraction versus wavelength an empirical formula for the index dispersion is found to be,

$$\Delta n(\lambda) = \frac{\Delta n_o \lambda}{\sqrt{\lambda^2 - \lambda_o^2}} \tag{6.3}$$

with Δn_o=0.2002 and λ_o=327.44 nm. It is then possible to calculate the retardance at any voltage and wavelength using,

$$\Delta \phi(V, \lambda) = \Gamma(V)_m \frac{\lambda_m}{\lambda} \frac{\Delta n(\lambda)}{\Delta(\lambda_m)} \tag{6.4}$$

where $\Gamma(V)$ is the given measurement of phase versus voltage at 633 nm, λ_m is the calibration wavelength of 633 nm, and λ is the wavelength of interest. We found that using this method to calibrate the SLM phase versus voltage at our wavelength of 780 nm is too inaccurate.

Determining the phase retardation at 780 nm directly via measurement proved to be a much more accurate calibration technique. This was done by operating the SLM as an attenuator between crossed polarizers. Unlike the previous calibration of the pixel versus wavelength, for this measurement high quality polarizers must be used and oriented at exactly $\pm 45^o$ from vertical. We conducted this calibration two ways. The first was to use the repump laser again and mea-

sure the transmitted power via a single photodiode, giving a calibration at one wavelength.

To check for variations over the bandwidth of our Ti:Sapphire spectrum a second technique was used in which the attenuation versus voltage was measured via an optical spectrum analyzer. Software was written to measure the spectrum power versus voltage and extract the full phase retardation across the pulse bandwidth. In principle we could have used this data directly to calibrate the SLM, however, we found using Eq.(6.4) in conjunction with the repump laser measurement was sufficient over the 55 nm bandwidth of our spectrum. The measured transmission curve, normalized to unity, and the extracted phase dependence versus voltage count using the repump laser technique is shown in Fig. (6.2). Note that this was measured with SLM operating in low voltage mode. A specific example illustrating the necessity of this calibration is shown in Fig. (6.8) of section (6.2) using the results of the coherent control experiment directly.

We have discussed some of the calibration necessary to change the spectral phase of the Ti:Sapphire pulses with the SLM based pulse shaper. However, for our coherent control experiment we wish to know the actual spectral phase of the pulses at the Rb atoms. Dispersion due to optical components such as lenses, the Pockels cell, and the pulse shaper must be compensated for by the SLM phase mask to ensure the pulses at the MOT have a flat spectral phase. The amount of dispersion possible with the SLM phase mask is much less than the grating pulse stretcher used in section (5.2). It is limited by the use of a pixelated phase mask to approximate a smooth dispersion function. For example, if the phase versus wavelength varies by 2π radians between adjacent pixels the approximation completely breaks down.

The two-photon photocurrent was measured on a GaAsP photodiode versus the second, third, and fourth order dispersion applied to the SLM. More specifi-
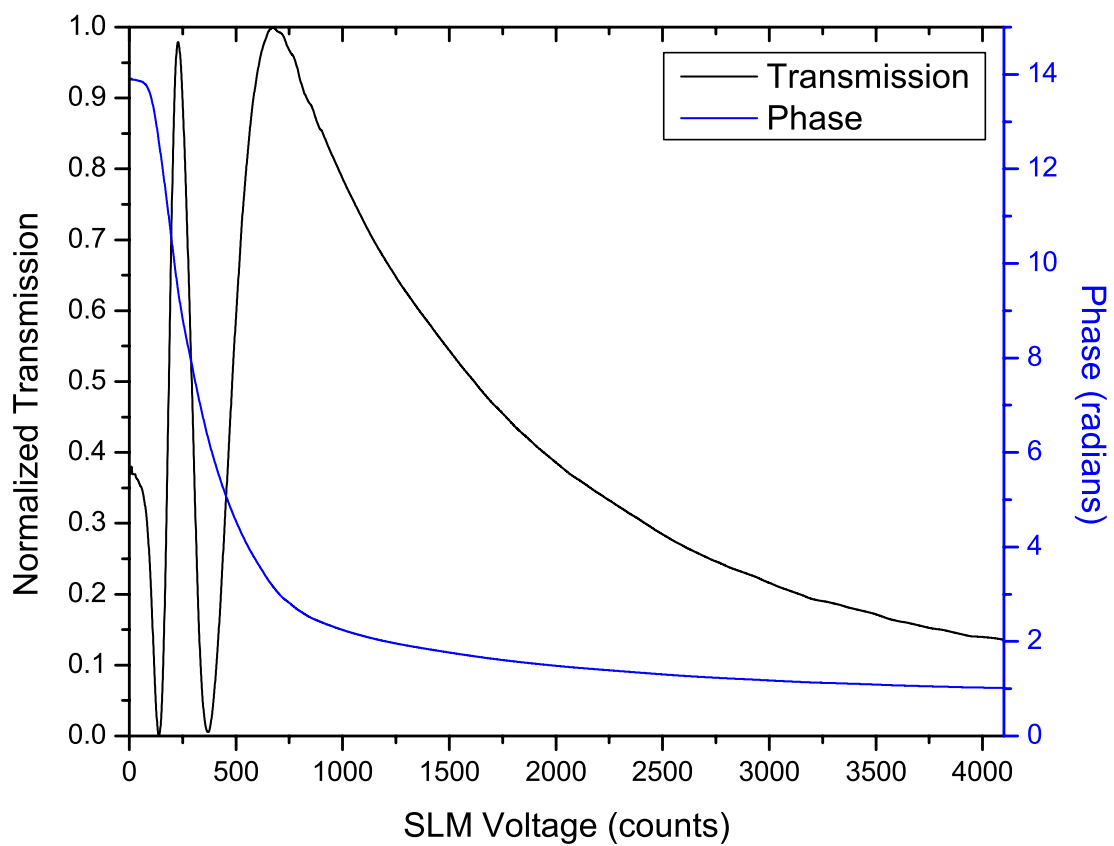
Figure 6.2: Measured transmission and extracted phase versus SLM voltage count using the repump laser at 780.2 nm.

cally, to search for a global maximum in the photocurrent and thus the shortest pulse, a two dimensional map versus both the second and third order dispersion was measured. Figure (6.3) is an image constructed from the two-dimensional scan, the lighter areas correspond to higher photocurrent. One particularly important feature is that there are local maxima, so it is necessary to survey a sufficiently large region to find a global maximum with high confidence. In our case we varied the second order dispersion from about 1000 fs^2 to -8000 fs^2 and the third order from 100,000 fs^3 to -250,000 fs^3. The global maximum was found and set on the SLM to be -4350 fs^2 and -74,000 fs^3. We also checked for fourth order dispersion and found an optimum value of -37,500 fs^3 with the second and third orders fixed. Considering the negligible amount of fourth order dispersion we can conclude that this method is sufficient to find the shortest pulse. Note that this calibration neglects any spectrally sharp dispersion that may occur, for example due to the rubidium atoms themselves.

Once the spectral phase of the pulses is adjusted to be nearly flat at the MOT the spectral amplitude must be calibrated as well. One of the calibration techniques is to use the SLM as a variable attenuator by placing the liquid crystal element between crossed polarizers and varying the birefringence. Nominally the input polarization is vertical, this is set by the PBS at the exit of the Pockels cell. However, due to the fact some of the grating and mirror reflections in the pulse shaper occur with both s- and p-polarizations there is some ellipticity induced in the polarization, due to slightly different phase shifts between the two polarization projections upon reflection. This is particularly true for the dielectric pickoff mirror. The slightly elliptic polarization of the Ti:Sapphire light will become more elliptic after passing through the liquid crystal of the SLM and in general any subsequent optics before the MOT.

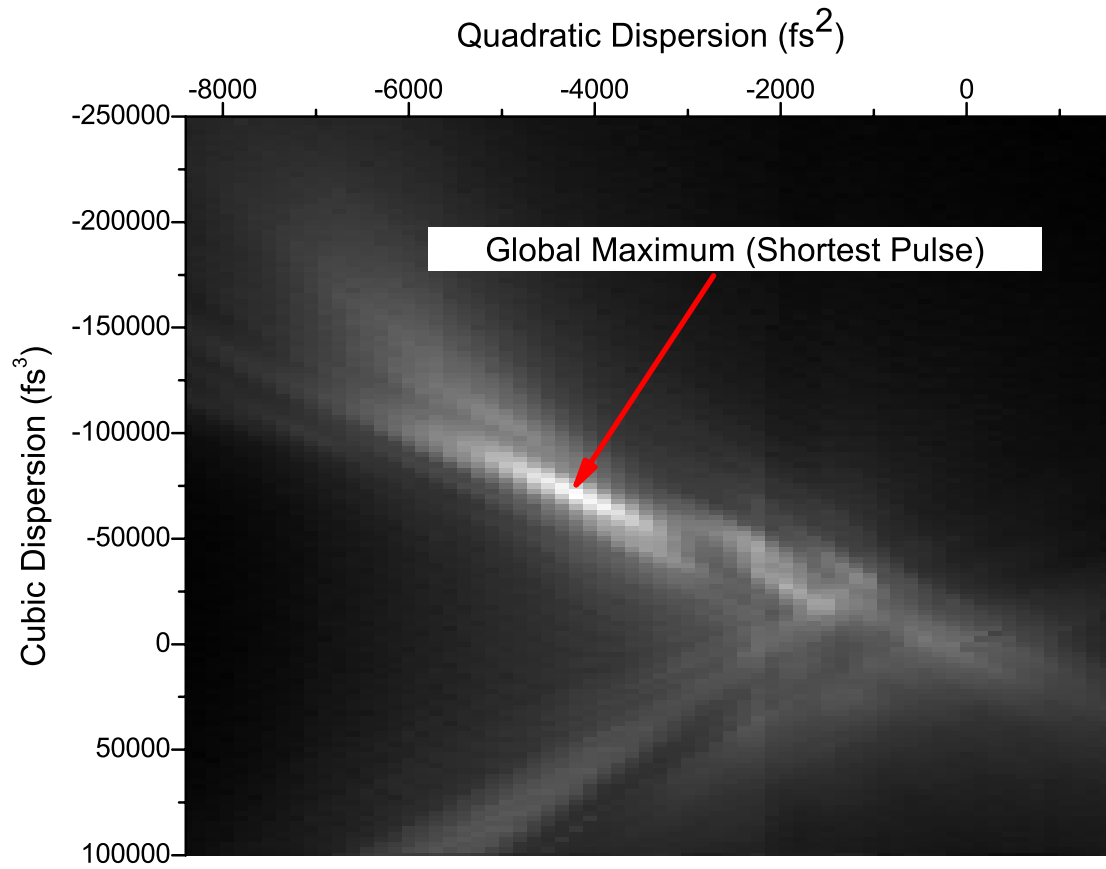For this experiment we used a PBS cube as a beam splitter in conjunction

Figure 6.3: Map of two-photon photocurrent versus second and third order dispersion applied to the SLM.

with a zero order half-wave plate before the MOT two create two equally balanced probe beams. Recall that to obtain a flat spectral phase at the MOT requires dispersion compensation, which is done via a spectral phase mask on the SLM. Figure (6.4)(a) shows the spectrum measured on an OSA placed in one output port of the PBS before the MOT with just dispersion compensation applied to the SLM and one of the phase masks used in section(6.2). The details of the phase mask are not important at this point, only the fact that the spectrum changes when the phase mask applied to the SLM is changed. This is of course a problem for conducting a coherent control experiment in which we desire to change only the spectral phase of the pulses. Placing a polarizer before the half-wave plate remedies this problem to a large extent, see Fig. (6.4)(b). There is some residual reshaping of the spectrum that occurs due to the pulse shaper, for example the plateau at 770 nm, however we were unable to determine the cause. One remaining unavoidable source of spectral amplitude modulation as a function of the SLM phase mask is due to diffraction. Diffraction occurs for wavelengths that have a focal spot covering two adjacent pixels with different phases. For example, if half the mode undergoes 0 phase shift and half π radians phase shift the wavefront will be distorted from that of a Gaussian mode and therefore diffract differently.
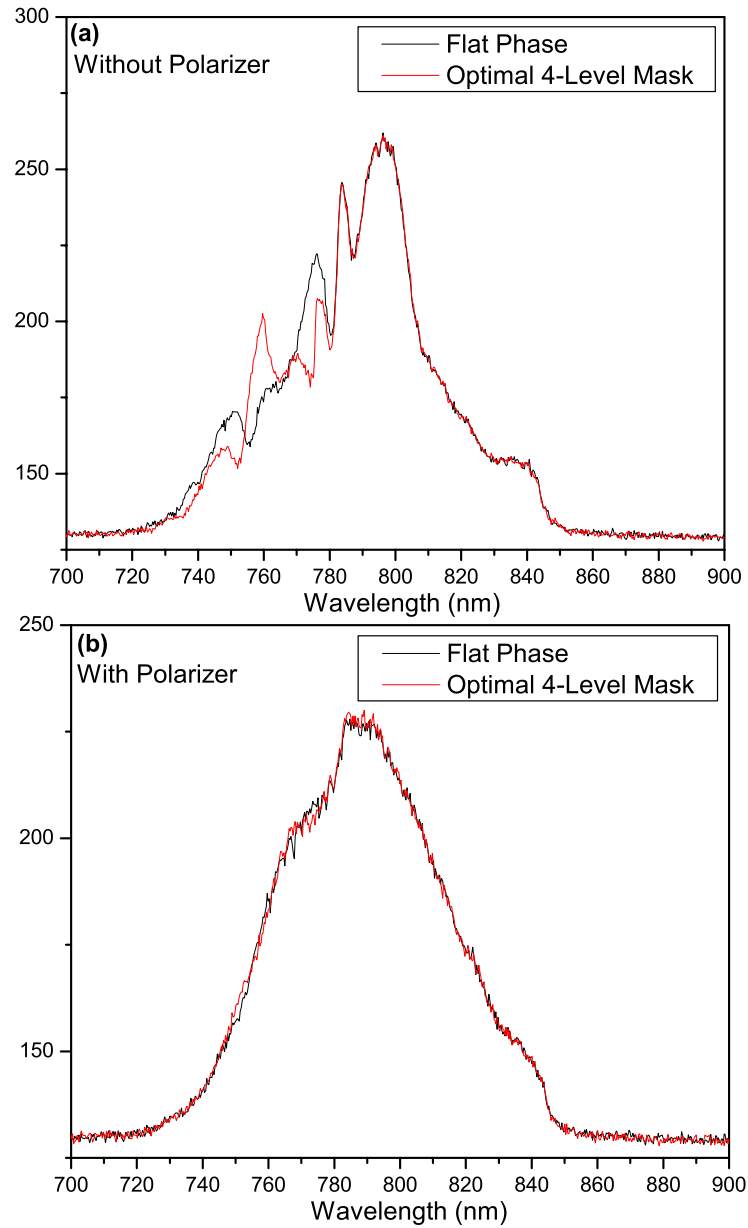
Figure 6.4: (**a**) Power spectrum of Ti:Sapphire measured on one exit port of the PBS before the MOT versus applied SLM phase mask (no polarizer between SLM and PBS) (**b**) Power spectrum measured the same as in (**a**) with a polarizer between the SLM and PBS before the MOT.

6.2   Four-Level Interference Experiment

In our first coherent control experiment we demonstrated the effects of frequency chirp on a three-level system. The quantum interference that occurred was due only to the different optical modes of the comb. In this experiment we use the high-resolution of the comb to excite two different two-photon transitions to the same final state with different resonant intermediate states. This type of level structure is referred to as a closed-loop diamond configuration, see Fig. (6.5). There have been several theoretical studies of close-loop four-level systems predicting the optical phase sensitive response of the excited population in double-Λ [90, 91] and diamond configurations [92, 93, 94]. Applications of close-loop four-level systems have been proposed to enhance and control four-wave mixing [95, 96], amplification without inversion [97], and lasing without inversion [98] for cw-VUV lasers. This type of level sub-structure can also be of importance to studies of molecules, for example the sign of the product of dipole moments is of importance for two-dimensional spectroscopy [99], for which there are molecular states excited in a closed-loop configuration. Controlling the interference of two two-photon transitions can also be used for changing molecular dissociation pathways [100].

There have been a limited number of experiments done using cw-lasers to excite a closed-loop four-level system. For example, to control population trapping [101], and to phase correlate independent lasers [102]. However, these previous experiments were severely limited by the optical bandwidth of their lasers. The bandwidth was limited by the phase modulation frequency of a cw-laser via an electro-optic modulator. In our comb experiment we demonstrate phase control of the two-photon absorption with a visibility of 69% using resonant wavelengths spanning 32 nm, far surpasing the bandwidth of previous experiments.
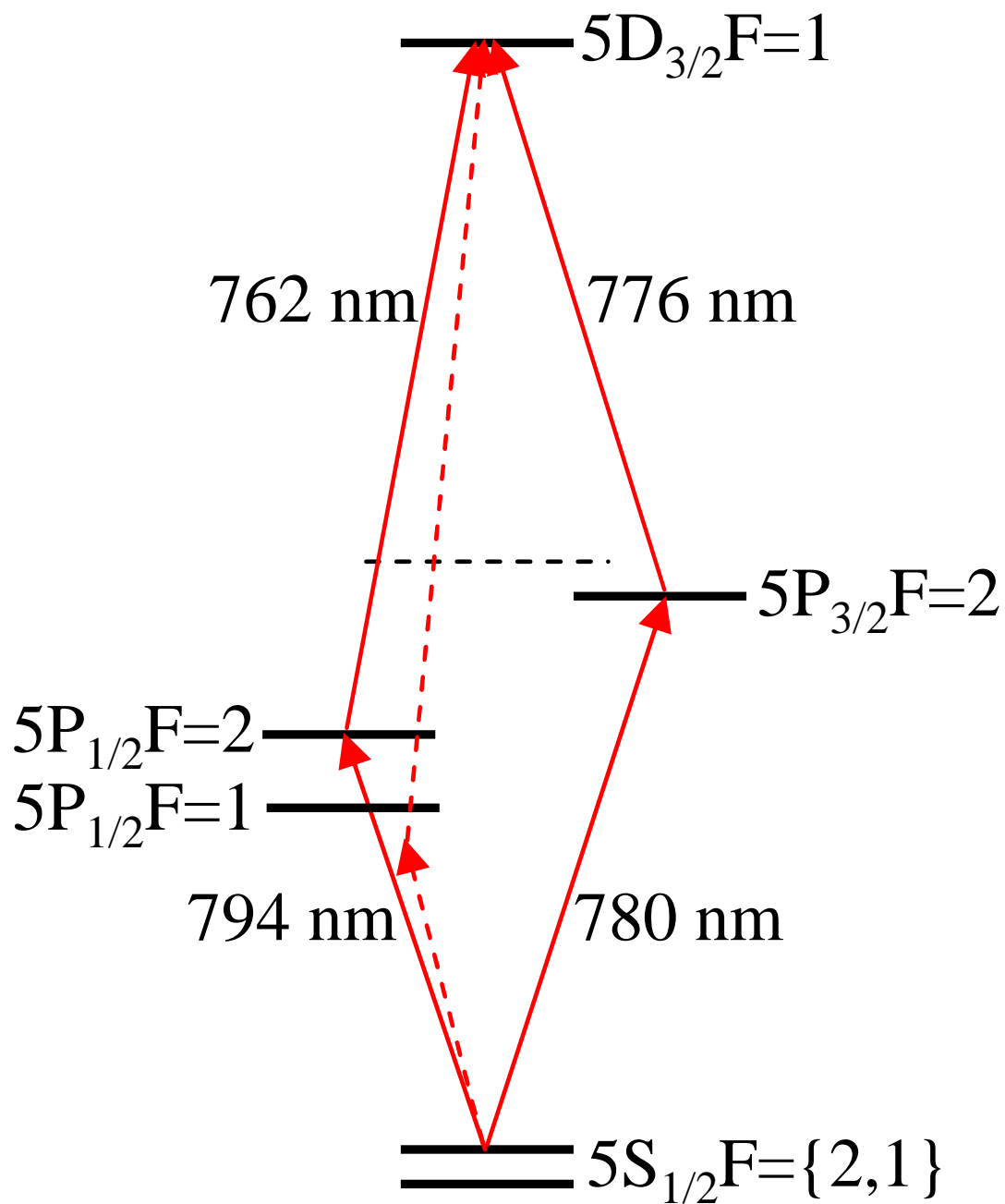
Figure 6.5: Relevant ^{87}Rb level subsystem for the diamond coherence experiment. The dotted lines indicate an extra off-resonant transition via the 5P$_{1/2}$F=1 state.

It is possible to find two combinations of f_r and f_o, both resonant with a four-level diamond configuration subset of ^{87}Rb levels. In particular, by tuning f_r=100.59660605 MHz and f_o=+16.94 MHz the four resonant states are: $5S_{1/2}F=2$, $5P_{1/2}F=2$, $5P_{3/2}F=2$, and $5D_{3/2}F=1$. This choice of levels is well suited for our coherent control experiment because the different transition wavelengths are easily resolved with our SLM pulse shaper. Furthermore these two resonant two-photon transitions can be nearly equal in amplitude for a sufficiently broad pulse spectrum. Figure (6.5) shows a simplified energy level diagram of the resonant four levels with the corresponding transition wavelengths indicated by solid red lines. This figure also shows the intermediate state $5P_{1/2}F=1$; the nearest comb mode is detuned about two linewidths from this state, however, the importance of this transition path will be demonstrated in our subsequent calculations.

A slightly shifted value of f_r=100.59660525 MHz with the same f_o creates a different four-level diamond consisting of the same intermediate and excited states but from the $5S_{1/2}F=1$ ground state. All 7S and 5D states with the exception of $5D_{3/2}F=1$ are detuned at least 6 MHz for either choice of f_r. For both four-level subsystems the corresponding resonant wavelengths are approximately: 794 nm, 762 nm, 780 nm, and 776 nm. The first two wavelengths correspond to the transition via $5P_{1/2}F=2$ and the second two via $5P_{3/2}F=2$. So the largest separation between resonant wavelengths is 32 nm, the difference between the wavelengths resonant with the $5P_{1/2}F=2$ transition. We would like the electric fields strength of the resonant modes to be approximately equal so for this experiment the Ti:Sapphire was operated with a spectrum centered at 778 nm with a spectral width of about 63 nm FWHM, the largest we could achieve. Recall that the pulse shaper reshapes the spectrum somewhat, as seen in Fig.(6.4). So in our calculations we used electric field values derived from this reshaped spectrum measured directly before the MOT.

The data collection procedure and general experiment setup is very similar to our previous experiments. Rubidium atoms are cooled and trapped in a MOT for 6.5 ms. The trap and repump lasers, and magnetic field, are then switched off. To allow sufficient time for the magnetic field to turn off there is a 3 ms delay. After 3 ms the Pockels cell is switched on and transmits the Ti:Sapphire laser pulses through the pulse shaper and to the Rb atoms for 0.5 ms. This sequence results in a total MOT operation plus probing cycle time of 10 ms, and is repeated continuously so that we retrap and probe the atoms 100 times per second. During the 0.5 ms probing time the cascade fluorescence at 420 nm is measured via a PMT and counted using a SR430 multi-channel photon counter. The SR430 multi-channel photon counter was operated with 1024 separate channels (or bins), each with a temporal width of 640 ns and triggered simultaneously with the Pockels cell. All data points presented in this section were accumulated over 4000 MOT cycles, or 40 s per point in terms of experiment operation time.

The Ti:Sapphire probe beam was split into two paths using a PBS cube and a zero-order half wave plate just before the MOT. This allowed us to either transmit all the power into one probe beam, or balance the power between two counter-propagating probe beams. A second zero-order half wave plate was placed in one of the two paths to rotate the polarization 90°, so that the atoms are excited by two horizontally polarized, equal intensity, counter-propagating probe beams. For this experiment one of the two probe beam paths passes through an adjustable optical delay line, this was set such that the optical path from the PBS to the center of the MOT is equal with an estimated uncertainty of about ± 5 mm.

We demonstrate coherent control of the excited state, $5D_{3/2}F=1$, population by adjusting the phase of one resonant path of the diamond with respect to the other. This demonstration was accomplished using the phase mask shown in Fig.(6.6) to apply a variable phase, denoted as $\Delta\Phi$, to the spectral region from

772 nm to 784 nm. The phase shifted spectral region covers the comb mode pair resonant with the $5S_{1/2}F=2$ to $5P_{1/2}F=2$ to $5D_{3/2}F=1$ transition. It also covers the spectral region up to 4 nm shorter than the resonant wavelength 776 nm and 4 nm longer than 780 nm. By choosing a large region over which to adjust the phase we can assume all comb mode pairs with an intermediate state detuning of up to $\sim$4 nm acquire the same phase, $\Delta\Phi$. This is important for this experiment because we would like to neglect the comb mode pairs detuned from an intermediate resonance, which can only be done if the net amplitude from these pairs cancels to zero. Note that although it is not shown in Fig.(6.6) the SLM is always operated with the necessary dispersion to compensate for the optics in the beam path from our previous calibration. So the actual spectral phase of the pulses at the Rb atoms is ideally just due to the phase mask shown in Fig.(6.6).

It is useful to cover some of the initial results of this experiment to demonstrate how we arrived at our final data. For this experiment, in particular the road to the final results is most useful to an experimentalist. One of the first aspects of the data to optimize is the fringe visibility as we varied the phase step $\Delta\Phi$. Initially we used a two-channel photon counter and integrated the counts for relatively long durations, between 100 μs and 500 μs per MOT cycle. During this time we also only probed the atoms from one direction, so that all atoms are excited by the same exact pulse shape, something we will discuss later. The important point is that when probing from one direction the atoms are pushed off of resonance, as we expected from our experience with radiation pressure. However, we noticed that the fringe visibility varied dramatically as a function of our photon counting window width. The reason for this proved to be a surprise.

Figure (6.7) shows the signal versus phase step $\Delta\Phi$ versus time, acquired using the SR430 multi-channel photon counter. At short times, less than 100 μs, we measure a clear fringe with a peak near $\Delta\Phi=0$ radians. At slightly longer
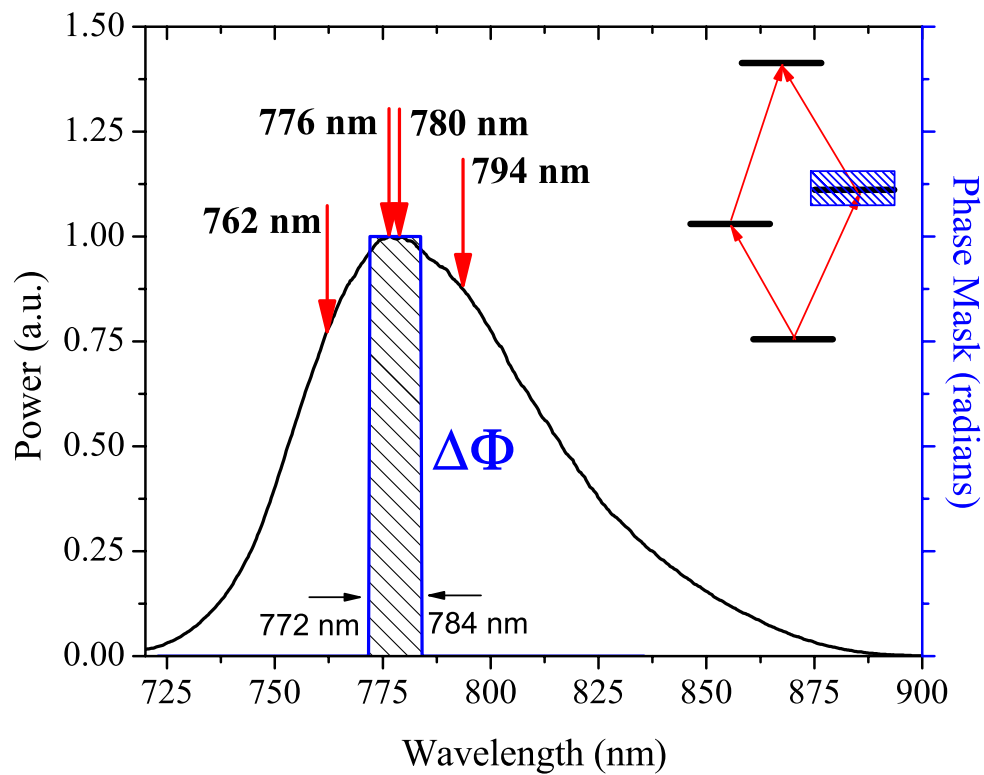
Figure 6.6: Spectrum of a pulse (directly from Ti:Sapphire) and the phase mask used in the four-level coherent control experiment. Red arrows indicate the positions of the resonant transition wavelengths with respect to the phase step of $\Delta\Phi$ radians.

times the signal rapidly drops to near zero and remains there for about 150 μs, as expected. The surprising feature is that at about 300 μs we again measure a fringe with a smaller signal but clearly shifted in phase, by almost $\Delta\Phi=90^o$. Clearly integrating the signal versus time will result in a reduced fringe visibility for times longer than about 300 μs, because it is in fact two separate fringes that are completely out of phase. Keeping in mind that we are accelerating the atoms in one direction as we scatter photons the comb f_r in the frame of the atoms appears on average to be reducing versus time, or more accurately versus velocity. This is how we discovered the second f_r resonance condition mentioned previously, which happens to correspond to excitation from the $5S_{1/2}F=1$ ground state. However, this does not explain the obvious phase shift between the two fringes, we defer that discussion until we present the final fringe results and a more complete analysis of the transitions.

Still with the intention of increasing the fringe visibility we considered the effect of the hot Rb vapor in the MOT chamber. Although the comb is tuned to be resonant with a specific subset of four Rb levels, this is only true for the atoms that are cooled in the MOT to have negligible velocity in the lab frame. Due to the fact that the comb mode spacing of 100 MHz is much less than the Doppler width of the hot Rb atoms, all allowed transitions within the bandwidth of the comb will in general be excited in these hot atoms. For example, the strongest two-photon transition in terms of dipole moments is the $5S_{1/2}F=2$ to $5P_{3/2}F=3$ to $5D_{5/2}F=4$ transition. In terms of the product of dipole moments, meaning the dipole moment from 5S to 5P multiplied by the dipole from 5P to 5D, this transition is about 9 times as strong as either transition path in the intended four-level system.

The transitions in the hot atoms will in general yield a constant background signal that does not vary as a function of the applied $\Delta\Phi$. For example, none of the

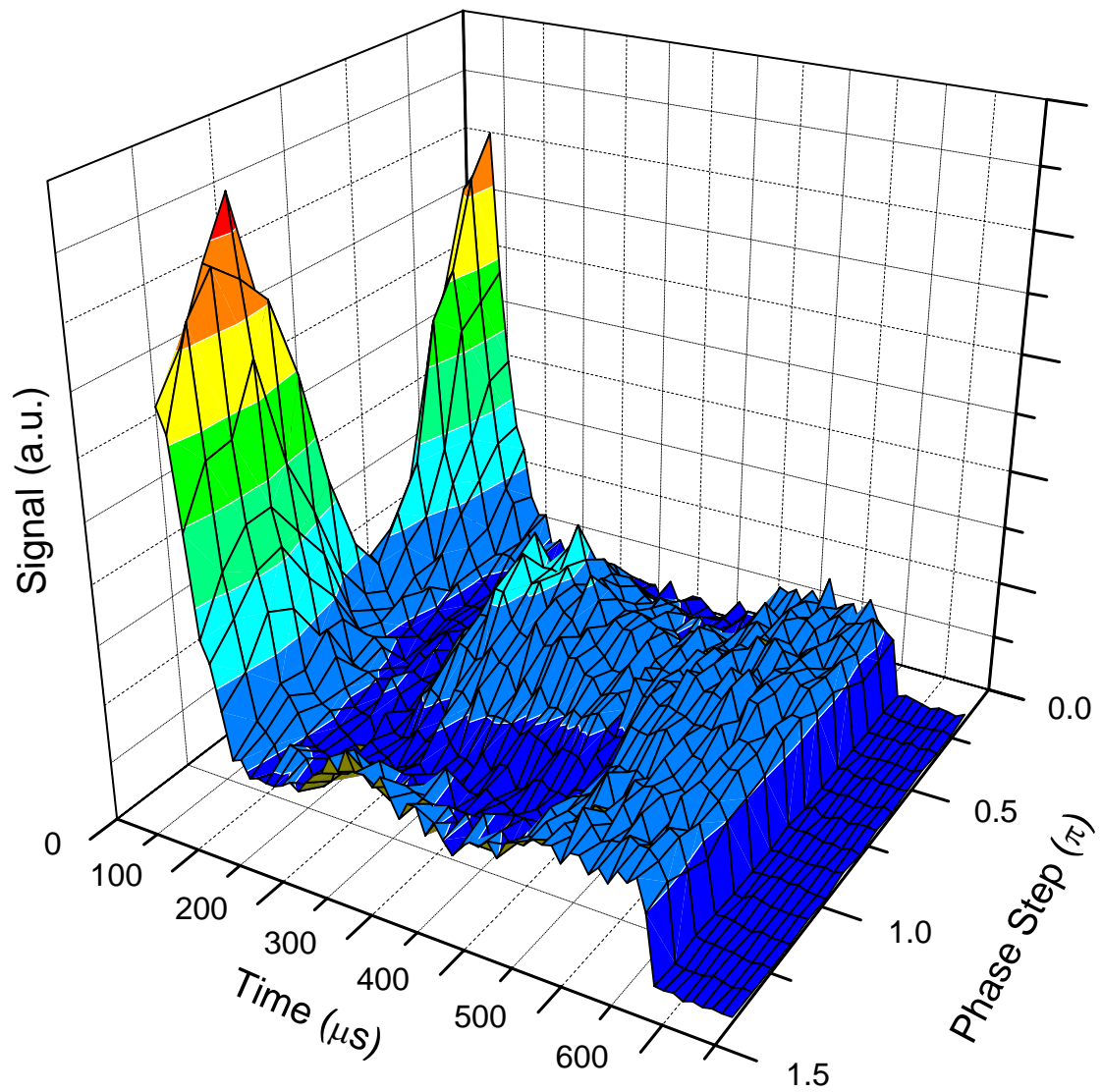Figure 6.7: Measured single beam signal versus SLM phase step versus excitation time. The initial fringe is due to transitions from $5S_{1/2}F=2$. At longer times the atoms are Doppler shifted onto resonance with the same transition but from the $5S_{1/2}F=1$ ground state. Notice the clear phase shift between the two fringes, clearly averaging the signal too long can reduce the fringe contrast.

transitions to $5D_{5/2}$ states can be accessed via the $5P_{1/2}$ intermediates states, and therefore will not be affected by shifting the phase of the $5P_{3/2}$ transition paths. It was easily verified that indeed the hot atoms were contributing a significant background signal to our initial results by simply measuring the signal without ever forming a MOT.

We tried to reduce the signal due to these hot atoms by two methods. First, we modified the optics before the PMT to form an image of the cooled atomic cloud onto an aperture that was adjustable via micrometers, thus blocking light originating from outside the cooled atom cloud. This was only moderately successful due to the fact that in the 3 ms after cooling the atoms, but before probing them, the hot atoms have ample time to redistribute throughout the chamber. So when we actually probe there are hot atoms distributed throughout the cold atomic cloud. This forced us to operate the Rb getter at a significantly lower current, thus lowering the density of hot Rb vapor. At a getter current of about 2.5 Amps, really only relevant for our specific setup, we were able to reduce the signal from the hot atoms. At this getter current the signal from the hot atoms was not the dominant contribution to the fringe minimum, and there was sufficient signal from the reduced number of trapped atoms.

Now that we have an understanding of how to increase the fringe visibility we turn our attention to the fringe period. Due to the fact the phase mask covers both resonant wavelengths of the transition through $5P_{3/2}F=2$ the fringe period in terms of $\Delta\Phi$ is expected to be π radians. Ruling out any physics of the light-matter interaction that could give rise to a period other than π, we attribute any measured deviation from this periodicity to miscalibration of the SLM. Figure (6.8) shows the fringe measured with two different SLM phase versus voltage calibrations. The details of this calibration procedure were discussed in section (6.1.2). Initially we used the manufacturers SLM calibration done at 633 nm and

used Eq. (6.4) to determine the phase versus voltage at our desired wavelengths centered around 778 nm. With this calibration technique the measured fringe period was approximately $1.15 \times \pi$ radians. Using direct calibration of the SLM at 780 nm with the repump laser we repeated the measurement and recovered a much improved fringe period of $(1 \pm 0.01) \times \pi$ radians.

We now proceed to discuss our final data sets demonstrating the ability to control the excited $5D_{3/2}F=1$ population via our SLM phase mask. Figure (6.9) shows four fringes taken under different experimental conditions to demonstrate some of the relevant physics. The fringes in the top two panels labeled as (**a**) and (**b**) were measured using traveling wave excitation, meaning the atoms were probed from only one direction with the Ti:Sapphire. The bottom two panels labeled as (**c**) and (**d**) present the results under what we refer to multi-mode standing wave excitation, meaning if we probe the atoms with counter-propagating beams.

As mentioned previously, there are two different resonance conditions obtained using slightly shifted values of f_r. The left panels were taken with f_r corresponding to excitation from the $5S_{1/2}F=2$ ground state and the right panels using the f_r for excitation from the $5S_{1/2}F=1$ ground state. In the case of traveling wave excitation we have discussed the reduced fringe visibility versus probing time, due to the radiation pressure Doppler shifting the comb to another resonance. For this reason we only show the signal accumulated during the first 20.48 μs of probing time, short enough to avoid significant Doppler shifting.

After aligning the counter-propagating probe beams very well, we found that the atoms remain on resonance for about 250 μs, much longer than the $\sim$40 μs for the traveling wave data. So in the case of excitation via counter-propagating beams the atoms may be probed longer with essentially no reduction in fringe visibility. Despite this fact, the data presented in the bottom two panels for
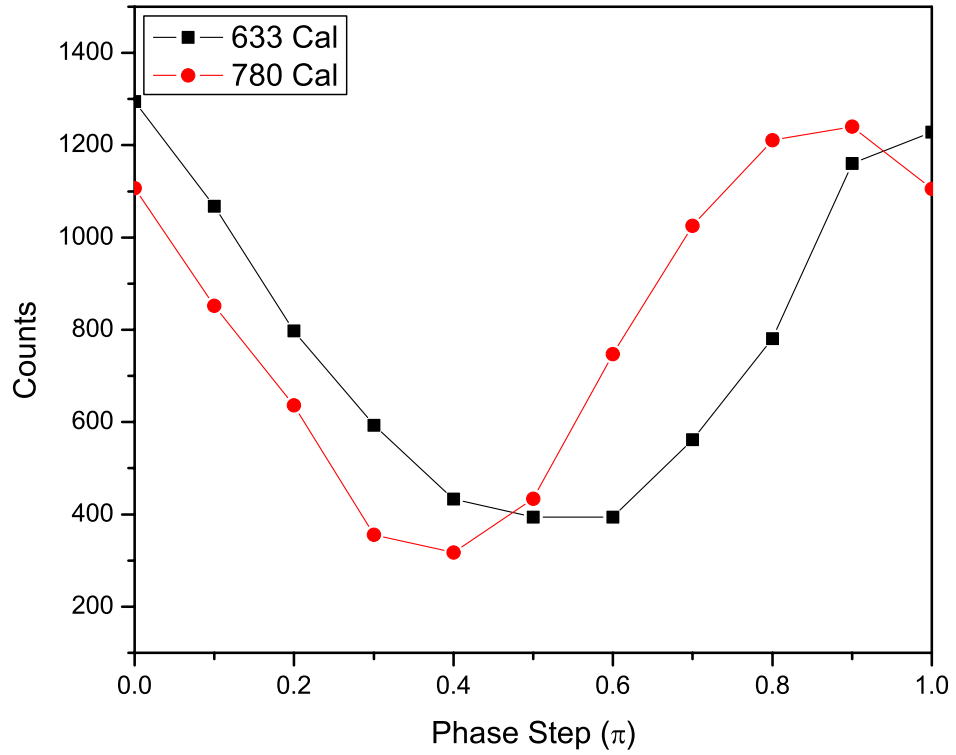
Figure 6.8: Measured fringe versus phase step, corresponding to $\Delta\Phi$ in Fig. (6.6), using SLM phase vs. voltage calibrations at 780 nm and 633 nm. The period of the fringe using the 633 nm calibration is too long, 1.15π radians. Using calibration at our operating wavelength of 780 nm produced a much better $1.0\pm0.01\pi$ radians period.

counter-propagating excitation correspond to only the first 20.48 μs of excitation for consistency. To avoid changing anything about the experiment except the excitation scheme the traveling wave data was measured simply by blocking the counter-propagating beam. So the Ti:Sapphire probe power used in the traveling wave case is half of the 75 mW used in the counter-propagating case. Both probe beams were focused into the MOT by the same 750 mm focal length lens mounted before the PBS cube used to split the probe beams. This results in about a 180 μm diameter focal spot at the center of the cold atom cloud. In general we measure the MOT atom number stability with a photodiode setup to image the MOT, it is not necessary to calibrate for the absolute number of atoms. This photodiode measures the scattered trap and repump laser light during the last 1 ms of MOT formation, and is a useful tool for normalizing any slow drift in atom number.

Each fringe in Fig. (6.9) is shown with a fitting function of the form $c_1 + c_2 cos(\Phi + c_3)^2$, with the free variable Φ, which is the phase step applied via our SLM mask. After determining that the observed period was very nearly π, we dropped any dependence in the fit function on the period. The parameter c_1 represents the fringe minimum, c_2 is simply the magnitude of variation due to the interference, and c_3 is the fringe offset phase from zero. Combining the c_1 and c_2 parameters we can write the fringe visibility, defined $\frac{max-min}{max+min}$, as $\frac{c_2}{2c_1+c_2}$. In each panel of Fig. (6.9) the extracted fringe offset and visibility is shown. Our best measured fringe visibility is 69%. This is a significant improvement from our intial results which were as low as 25%, clearly the previously mentioned techniques for improving fringe contrast were successful.

We have used two theoretical approaches to understand our results and compare them with the predicted fringe visibility and phase offset. The first and significantly more complicated approach is to directly solve the Liouville equation for the density matrix of the system under shaped pulse excitation. To this end
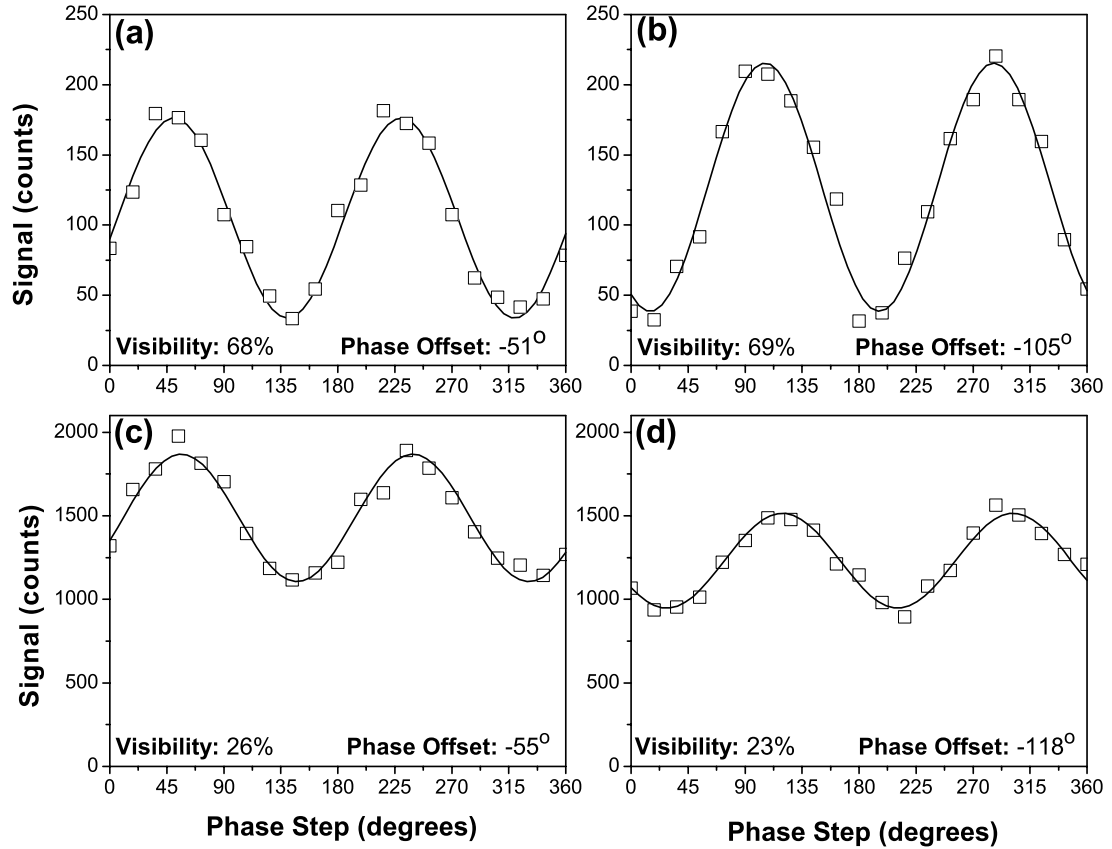
Figure 6.9: Measured signal fringes versus SLM phase for four excitation configurations. (**a**) Traveling wave excitation from F=2, (**b**) traveling wave excitation from F=1, (**c**) multimode standing wave excitation from F=2, and (**d**) multimode standing wave excitation from F=1.

we initially developed a four-level model which incorporated only the four resonantly excited states. The driving field in this model was constructed by taking the Fourier transform of the measured spectrum, shown in Fig. (6.4), with a spectral phase given by the applied SLM mask mask. As a practical side note the sharp steps in the pixelated phase mask were smoothed, this is a necessary step to ensure the time domain field falls off to zero in a reasonable amount of time for our simulation. The results of this simulation were only partially successful. In particular the predicted fringe visibility was nearly perfect, approximately 99%, and the difference in phase offset between excitation from $5S_{1/2}F=2$ versus $5S_{1/2}F=1$ was 90°. We will come back to the source of this phase offset in the context of second-order perturbation theory.

Based on our prior observation of the fringe visibility being reduced when accumulating data from both ground states, due to the Doppler shift of the comb, it stands to reason that both ground states should be included in the model. To try and account for the reduced fringe visibility we observed compared to theory we expanded our density matrix simulation to include five-levels. The fifth level being the second ground state. First it must be pointed out that when the comb is tuned to be resonant from the $5S_{1/2}F=2$ ground state, transitions from the other ground state to the same intermediate states are only 6 MHz detuned, slightly off-resonance. So a non-perturbative model which takes into account power broadening may predict some effects only in the presence of both ground states. In fact this five-level model does predict a reduction in fringe visibility as a function of field strength, however, this occurs at slightly higher fields than used in our experiment. To check this we measured the traveling wave fringes with reduced powers, but the fringe visibility was not improved. At this point we determined that perhaps other intermediate states needed to be included in the model and turned to using a treatment based on second-order perturbation

theory.

The simplicity of using second-order perturbation theory makes it an ideal method to model many different simultaneous two-photon transitions. In our experiment this is particularly true due to the fact that we are far from saturating the $5D_{3/2}F=1$ population. Furthermore the majority of the incoherent optical pumping that occurs is due to relaxation of the population in the intermediate states, and is therefore not phase sensitive. As a reminder the resonant two-photon amplitude for absorption from two modes with one intermediate state is given by,

$$c_{gf} \propto \frac{|E_n||E_m|e^{i(\phi_n+\phi_m)}\mu_{gi}\mu_{if}}{i(\omega_{gf}-(m+n)2\pi f_r - 4\pi f_o)+\pi\Delta\nu_f} \times$$
$$\left[\frac{1}{i(\omega_{gi}-2\pi(nf_r+f_o))+\pi\Delta\nu_i} + \right.$$
$$\left.\frac{1}{i(\omega_{gi}-2\pi(mf_r+f_o))+\pi\Delta\nu_i}\right], \tag{6.5}$$

where $|E_{N(1,2)}|$ and $\phi_{N_{1,2}}$ are the magnitude and phase of the N_1 and N_2 modes, $\omega_{gf}(\omega_{gi})$ are the transition frequencies from ground to final(intermediate) states, and $\Delta\nu_{i(f)}$ are the intermediate(final) state linewidths in Hertz. Equation (6.5) is valid only for mode pairs that are two-photon resonant. The total two-photon amplitude is then reasonably approximated by the summation of two-photon amplitudes for each transition path, for example in the four-level diamond there are only two main transition paths corresponding to each intermediate state. Note that we refer to these as the main transitions, it is also possible to have much weaker transitions, for example absorption from $5P_{3/2}F=2$ to $5D_{3/2}F=1$ followed by stimulated emission to $5P_{1/2}F=2$.

One of the benefits of using a comb for coherent control is that there are many modes; in this experiment it allowed us to use four phase coherent modes to excite the four-level diamond system. The remaining hundreds of thousands of modes can lead to complications and must be considered. In particular we

show the $5P_{1/2}F=1$ level in Fig. (6.5) and two modes resonant from either ground state to the $5D_{3/2}F=1$ excited state via this intermediate state. In our initial analysis of the physics the two-photon amplitude due to this transition pathway was disregarded because the closest modes to this state are detuned by nearly two linewidths, about 12 MHz. Due to the fact this transition path has larger dipole moments than the other two resonant paths it may not be neglected.

The information necessary for estimating a fringe phase offset and visibility, assuming no residual pulse chirp, is tabulated in table (6.10). The top section is for transitions from the $5S_{1/2}F=2$ ground state and the bottom for transitions from the $5S_{1/2}F=1$. It is important to notice that the angular part of the dipole moment matrix elements for the 5S to 5P transitions are a function of the particular ground state. Corresponding to each single photon transition step the angular part of the dipole moment matrix element is given by $\langle Lm_F F||\hat{\mathbf{r}}||L'm'_F F'\rangle$, these are labeled as μ'_{gi} and μ'_{if} in Table (6.10), for the 5S to 5P, and 5P to 5D transitions respectively. The next column in the table denoted $\Delta(\text{MHz})$ is the detuning of the nearest comb mode for that particular transition from the intermediate state. Using the dipole moments, intermediate state detuning, and measured pulse spectrum, we calculated the corresponding two-photon amplitude. The last two columns of the table are the magnitude (only relative values) and phase of the amplitude, assuming excitation by a transform limited pulse. Each intermediate state is labeled by its m_F quantum number, since we are exciting with linearly polarized light with nominally zero magnetic field we use q=0 selection rules. Noting that transitions in which $\Delta F=0$ there can be no $m_F=0$ transition for q=0 we only need to include $m_F=0$ states for excitation from $5S_{1/2}F=1$. We do not tabulate the $m_F=-1$ transitions because, although each step may have different dipole moment signs, the two-photon amplitude is the same as for $m_F=1$ transitions. Concerning estimates of the fringe properties for transitions from $5S_{1/2}F=1$,

in which $m_F=0,\pm1$, we assume an equal population distribution between all m_F ground states.

Using the two-photon amplitudes in Table (6.10) we can estimate the total two-photon amplitude due to transitions through the $5P_{1/2}$ states. For example, in the case of transitions from the $5S_{1/2}F=2$ ground state, the total two-photon amplitude due to transitions through $5P_{1/2}$ states is given by,

$$c_{5P_{1/2}} = 3.4e^{i(-7.6\pi/180)} + 4.3e^{i(75.4\pi/180)}. \tag{6.6}$$

The phase of this amplitude is 39.8^o, the phase of the transition through $5P_{3/2}F=2$ is -3.8^o, so even for a transform limited pulse we expect the fringe peak to be shifted by $\Delta\Phi = \frac{39.8^o+3.8^o}{2}$, or 21.8^o. We attribute the extra phase shift beyond this value, as seen in Fig. (6.9)(**a**), to residual pulse chirp. Within the scope of this theoretical model the visibility is given by,

$$\frac{2|c_{5P_{1/2}}c_{5P_{3/2}}|}{|c_{5P_{1/2}}|^2 + |c_{5P_{3/2}}|^2} \tag{6.7}$$

Again using the values from Table (6.10) the predicted visibility is 82%, clearly much larger than the observed 69%. We do not know what sets the limit on the measured fringe visibility, however we have determined that is not a trivial background source such as stray light or hot atoms, due to the fact that the background level is present only with the Ti:Sapphire probing cold atoms. We have also used our theory model based on four-order perturbation and all the Rb 5S, 5P, and 5D states to estimate the population exited to all other 5D levels. However, this yields only a very small background contribution at our experimental field strength.

We can use the same estimation procedure for transitions starting from the $5S_{1/2}F=1$ ground state. In this case the total two-photon amplitude for the different m_F states do not interfere and therefore are only added incoherently.

	Intermediate	μ'_{gi}	μ'_{if}	Δ (MHz)	$|c'_f|$	θ
$5S_{1/2}\ F=2$	$5P_{3/2}F=2$, $m_F=1$	-0.17	-0.07	0.2	3.0	-3.8°
	$5P_{1/2}F=2$, $m_F=1$	-0.17	-0.09	0.4	3.4	-7.6°
	$5P_{1/2}F=1$, $m_F=1$	-0.29	-0.26	-11.5	4.3	75.4°
$5S_{1/2}\ F=1$	$5P_{3/2}F=2$, $m_F=1$	0.29	-0.07	-2.6	3.9	-139.1°
	$5P_{1/2}F=2$, $m_F=1$	-0.29	-0.09	-2.5	4.8	39.8°
	$5P_{1/2}F=1$, $m_F=1$	0.17	-0.26	-14.4	2.1	-101.8°
	$5P_{3/2}F=2$, $m_F=0$	0.33	-0.08	-2.6	5.1	-139.1°
	$5P_{1/2}F=2$, $m_F=0$	-0.33	-0.11	-2.5	6.6	39.8°

Figure 6.10: Relevant reduced dipole moments, detunings, and two-photon amplitudes for the 5-level system from both hyperfine ground states.

One unknown quantity is the population distribution between the different m_F states. If we neglect population in the $m_F=0$ states we calculate a fringe visibility of 99% and a phase offset of $\Delta\Phi=78.2^o$. The majority of this phase shift is due to sign of the angular part of the dipole moment matrix elements. More specifically the dipole moments for the resonant transitions from $5S_{1/2}F=2$ are all negative. However, in the case of excitation from $5S_{1/2}F=1$ one of the four dipole moments is positive. This is an example of the importance in considering not only the magnitude but also the sign of the dipole moments in closed-loop excitation schemes.

As mentioned previously there is an overall phase shift regardless of ground state due to the chirp. However, we can make a comparison with experiment in terms of the difference in phase offsets between excitation from $5S_{1/2}F=2$ and $5S_{1/2}F=1$. In this case the agreement between our model and experimental results is quite good. The theory prediction is 56° and the measured difference in the case of traveling wave excitation is 54°. If we include the $m_F=0$ transitions and assume equal population distribution the fringe is shifted by about 8° and the visibility is reduced to 92%. So the analysis based on second-order perturbation theory gives quite a good understanding of the relative phase shifts between fringes.

So far we have only discussed the fringes measured under traveling wave excitation. Panels (**c**) and (**d**) in Fig. (6.9) show the fringe measured using counter-propagating beams. The fringe visibility in both data sets is clearly reduced from the case of traveling wave excitation. Panel (**c**) corresponds to excitation from the $5S_{1/2}F=2$ ground state and shows a fringe with a visibility of 26%, compared to 68% for travling wave excitation. Similarly, panel (**d**) corresponds to excitation from the $5S_{1/2}F=1$ ground state and shows a visibility of only 23%. Generally we only use counter-propagating probe beams to balance the radiation pressure on the atoms and reduce the net Doppler shift, which usually results in an increased

signal to noise ratio.

Unlike our previous spectroscopy experiments, we must now consider the effect of standing wave electric fields within the atom cloud. Recall that we aligned the path lengths of the two probe beams to be equal such that the pulses overlap temporally and spatially in the center of the atom cloud. Figure (6.11) illustrates the standing waves created by the two resonant frequencies for transitions via $5P_{3/2}$, and similarly for $5P_{1/2}$, as a function of position from the center of the cloud. At the point in space where the pulses overlap temporally the average intensity of each comb mode is a maximum. In either direction along the probe beams the average intensity of a particular comb mode will vary spatially, just like a single frequency standing wave. The important point is that the resonant wavelengths used in our experiment have significantly different standing wave periods. So the electric field driving an atom is a function of the atom position with respect to the point in space where the pulses overlap temporally. For example, there are spatial regions of the atom cloud in which there is no average electric field at 780 nm. In this four-level experiment we wish to observe the interference produced by all four resonant comb modes, so if the average electric field corresponding to any of the four modes is zero the interference will not occur. However, it is still possible to excite population to $5D_{3/2}F{=}1$ if the electric fields for a pair of two-photon resonant modes is non-zero. In spatial regions where this occurs, the $5D_{3/2}F{=}1$ population, and thus the fluorescence at 420 nm, will not be phase sensitive.

To expand our theory model to include the multi-mode standing wave effect we simply average predicted the signal over the spatial dimension of the atom cloud. We did this over a distance of 0.5 mm corresponding to the atom cloud diameter, and assumed a uniform atom number spatially. The electric field strengths used in Eq. (6.5) were modulated spatially with a standing wave period appropriate to the particular comb mode. Again using the information from Table (6.10)
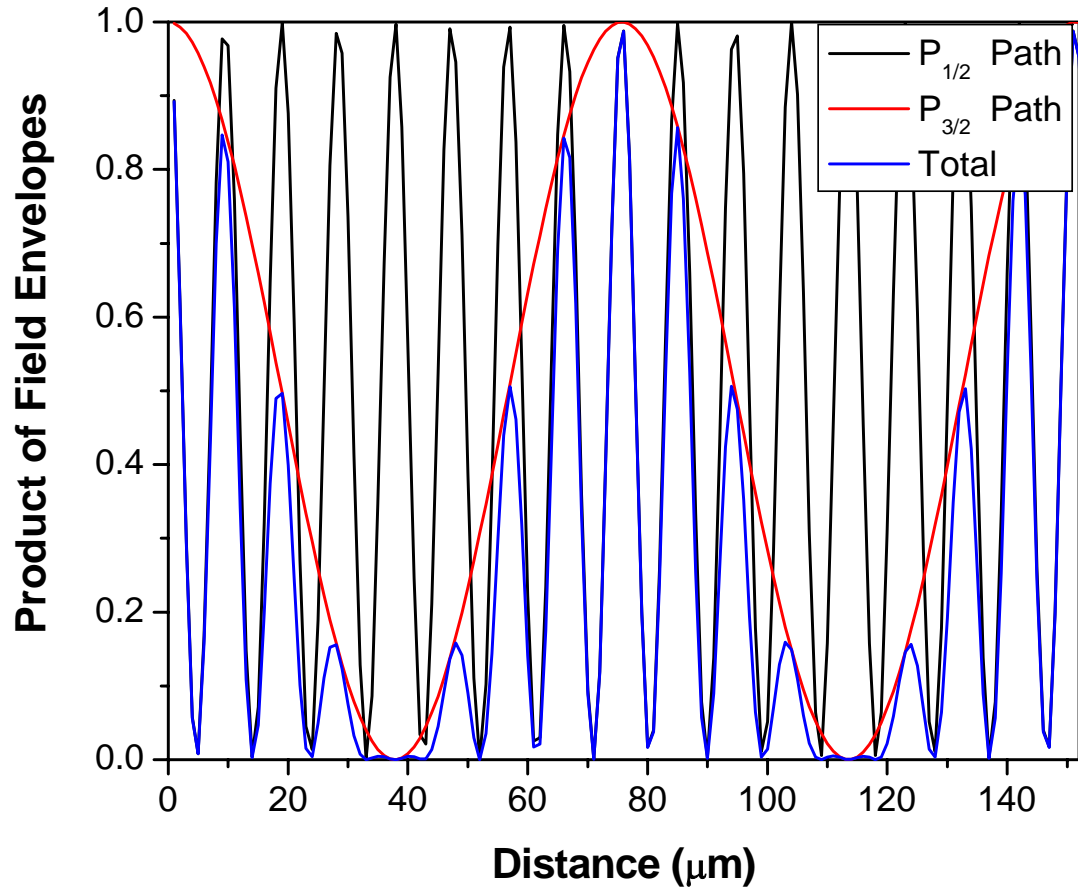
Figure 6.11: The black line is the average product of electric fields two-photon resonant via the $5P_{1/2}$ intermediate state, corresponding to wavelengths 795 nm and 762 nm. Similarly, the red line is for transitions via the $5P_{3/2}$ intermediate state and corresponds to wavelengths 780 nm and 776 nm. Notice that the two standing waves generated (black and red) have very different periods, due to the larger difference in wavelengths for the transition via $5P_{1/2}$. The blue line is the product of the red and black lines, this represents the spatial regions, and extent to which, all four resonant wavelengths are present. Clearly there is a spatial dependence not only on the expected 5D population (only two wavelengths required), but also on the phase dependence of this population (all four wavelengths required).

we calculated fringe visibilities of 36% for excitation from the F=2 ground state and 44% for the F=1 ground state.

This concludes the discussion of the four-level interference experiment. We have demonstrated coherent control of the $5D_{3/2}F=1$ population by tuning the interference between two different two-photon transition pathways. This interference is nominally due to only those comb mode pairs that are resonant or near-resonant with an intermediate state. The relative phase shift of the interference fringes can be explained within second-order perturbation theory using three intermediate states and six comb modes. This general scheme of enhancing and controlling a two-photon transition rate via multiple resonant or near-resonant pathways can in principle be extended to incorporate many more intermediate states. For example, this forms the basis of a proposal from our group to enhance a Raman type two-photon transition between highly excited and deeply bound molecular vibrational states [103]. The proposal relies on forcing constructive interference between two-photon amplitudes, due to different intermediate states, to a specific target state.

6.3 Four-level Enhancement Experiment

In the previous four-level interference experiment, the two-photon transition rate was solely due to the comb mode pairs near an intermediate state resonance. The goal of this experiment is to enhance the total two-photon transition rate by incorporating the many thousands of comb mode pairs detuned from an intermediate resonance. Recall that for a transform limited pulse the two-photon amplitudes from these modes pairs detuned from an intermediate state tend to cancel out, see Eq. (5.17) and the following explanation. This cancellation is due to a relative phase shift of 180° in the two-photon amplitudes for mode pairs detuned above versus below an intermediate state. To compensate for this 180°

phase shift we use the SLM phase mask shown in Fig. (6.12).

This experiment follows closely the experiment in reference [104] in which it was shown that the two-photon transition rate could be increased by pulse shaping if a resonant intermediate state is present. In that experiment a single femtosecond pulse from a Ti:Sapphire laser was used to excite all of the allowed 5S to $5P_{3/2}$ to 5D transitions in a Rb vapor cell. Due to the fact that the spectral resolution in that experiment is limited by the single pulse bandwidth any intermediate state covered by the spectrum is considered resonant. They show a seven fold increase in the measured fluorescence from the 5D states by applying a $\frac{\pi}{2}$ phase step between the resonant wavelengths of 780.2 nm and 776.0 nm. Clearly a signal increase by a factor of 7 is significant and could potentially be used to improve the signal to noise ratio in DFCS experiments. Especially because this outweighs the loss in signal incurred due to the power attenuation in the pulse shaper.

In our experiment, we use pulse shaping in a similar manner to increase the two-photon transition rate of the four-level system shown in Fig. (6.5), particularly from the $5S_{1/2}F=2$ ground state. The fact we use a comb to resonantly excite only the $5D_{3/2}F=1$ hyperfine level changes the physics significantly from the single pulse case. This is due to selection rules and dipole moments, analogous to our discussion of two-photon selection rules in chapter (4.3), subsection (4.3.3). In the single pulse excitation of Rb the dominant transition is to the $5D_{5/2}F=4$ hyperfine level due to the fact the dipole moments are larger than any other two-photon transition. Compared to either of the resonant transitions in our experiment, the product of the angular part of the dipole moments for the first and second steps to $5D_{5/2}F=4$, is a factor of 10 larger. Therefore the signal due to a single pulse is primarily from the $5D_{5/2}F=4$ population. Furthermore, the only transition path to $5D_{5/2}F=4$ is via $5S_{1/2}F=2$ to $5P_{3/2}F=3$, due to the $\Delta F=0,\pm 1$ selection rule. So in the application of Eq.(6.5) to calculate the total two-photon amplitude only
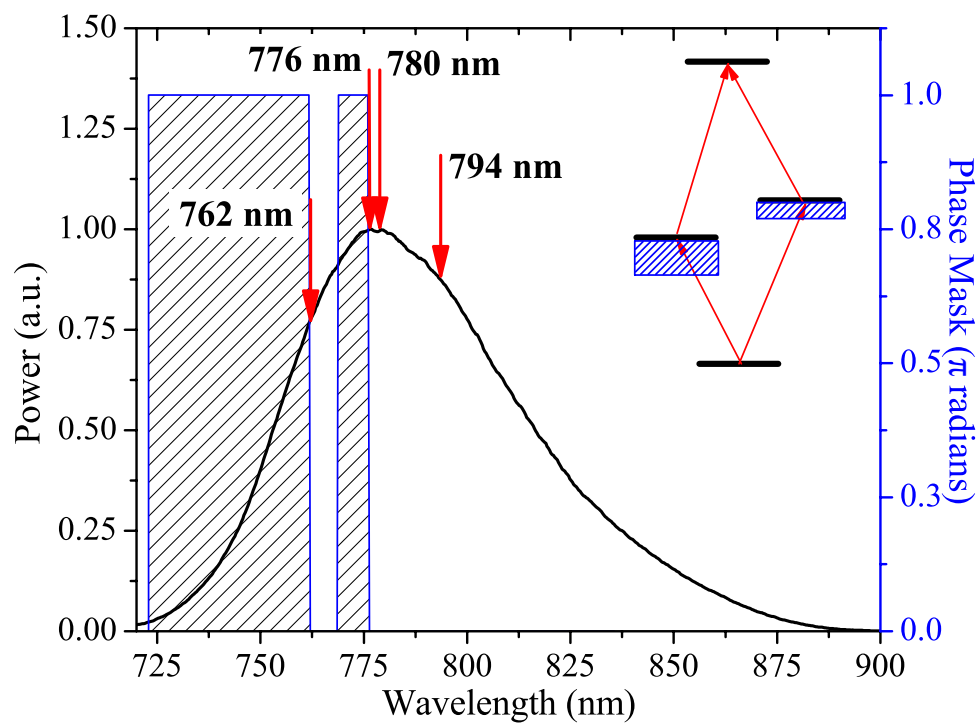
Figure 6.12: Spectrum of a single pulse (directly from Ti:Sapphire) and the phase mask used to enhance the two-photon transition rate (optimal 4-level mask). Red arrows roughly indicate the positions of the resonant transition wavelengths with respect to the phase steps of π radians.

one intermediate state is necessary regardless of detuning, when only $5D_{5/2}F=4$ is resonantly excited. In other words a three-level model with the corresponding dipole moments for the transition to $5D_{5/2}F=4$ correctly predicts a two-photon transition rate enhancement by a factor of 7 for the single pulse experiment. This is not the case for all two-photon transitions as we will show below.

In our comb experiment the number of possible intermediate states is four. Table (6.1) shows the angular part of the relevant reduced dipole matrix elements denoted μ'_{gi} and μ'_{if} for the ground to intermediate and intermediate to final state transitions. Equation (6.5) can be used to sum over all possible two-photon transition pathways using the dipole moments and states in this table. In the calculation of the two-photon amplitude the correct (measured) electric field strength and phase of each mode must be used.

Intermediate State	μ'_{gi}	μ'_{if}	$\mu'_{gi}\mu'_{if}$
$5P_{3/2}F=2$	$\frac{1}{6}$	$\frac{-\sqrt{\frac{2}{15}}}{5}$	-0.0122
$5P_{3/2}F=1$	$\frac{-1}{2\sqrt{15}}$	$\frac{1}{15\sqrt{2}}$	-0.0061
$5P_{1/2}F=2$	$\frac{1}{6}$	$\frac{-1}{2\sqrt{30}}$	-0.0152
$5P_{1/2}F=1$	$\frac{-1}{2\sqrt{3}}$	$\frac{\sqrt{\frac{5}{2}}}{6}$	-0.0761

Table 6.1: Angular part of the reduced dipole matrix elements for the four possible transitions from $5S_{1/2}F=2$ to $5D_{3/2}F=1$, the final column is the product of the given dipole moments.

In our previous experiment with the SLM pulse shaper the resolution was not important because we used a broad phase mask covering the resonant wavelengths for the transition via $5P_{3/2}F=2$, so knowing the exact wavelengths of each phase step was not essential. However, in this experiment we would like the π phase steps to occur as close as possible to $5P_{3/2}F=2$ and $5P_{1/2}F=2$. Our pulse shaper has a per pixel resolution of approximately 150 GHz at 780 nm, meaning each pixel corresponds to about 150 GHz of spectral width. This corresponds to the

resolution at which we can set the phase steps in Fig. (6.12) via software.

For finer resolution we mounted the entire SLM on a micrometer driven translation stage. By translating the SLM through the spectrally dispersed beam we are able to fine tune the frequencies at which the π phase steps occur, however not independently. The focal spot diameter with our given 3.5 mm input beam diameter and mirror focal length of 22 cm is about 60 μm. This is about half the pixel width so roughly speaking we may fine tune the frequency of one phase step with about a 75 GHz resolution. Given the fixed per pixel resolution of the pulse shaper once the frequency of one phase step is fine tuned the frequency of the second step is fixed for a set phase mask. Unfortunately this means that if we optimize the position of the phase step, around $5P_{1/2}$ for example, the position of the step near $5P_{3/2}$ is also fixed.

Using the phase mask shown in Fig. (6.12) the phase of the mode pairs that are detuned below either the $5P_{3/2}$ or $5P_{1/2}$ sets of states gain an extra π phase shift. We used the repump laser method described in section (6.1.2) to calibrate the wavelength corresponding to the center of pixel number 160. This results in the phase step near $5P_{3/2}$ occurring at λ=775.984 nm and the resonant wavelength effected is $\lambda_{res,1}$=776.157 nm. Similarly for the phase step near $5P_{1/2}$ we have λ=761.706 nm and the resonant wavelength effected is $\lambda_{res,2}$=762.103 nm. The difference in frequency offsets between the phase steps and resonant wavelengths is about 111 GHz, so this places a limit on how well we can optimize around the two fine-structure sets of states simultaneously.

The experiment was run similarly to our resonant four-level coherent control experiment. We used the same MOT timings, 6.5 ms load time, 3 ms for magnetic and MOT optical fields to be turned off, then probed for 0.5 ms. The full Ti:Sapphire power of 70 mW was focused into the atoms with a 750 mm focal length lens and used to probe the atoms from one direction only. Because we

are only interested in the enhancement of the two-photon transition rate due to the phase mask, we used a differential measurement technique. The atoms were probed for 1000 MOT cycles with the phase mask in Fig. (6.12) applied, then for 1000 MOT cycles with only dispersion compensation on the phase mask. Using the two-channel photon counter we measured probing times of 0-25 μs and 0-500 μs. Figure (6.13) shows the ratio of the signals with and without the phase mask, versus an arbitrary frequency offset. Each frequency offset corresponds to a different micrometer setting, or equivalently position of the SLM within the dispersed spectrum. Using the fact that each pixel center is separated by 100 μm and corresponds to a 150 GHz different frequency we were able to calibrate the frequency versus position.

We achieved a maximum enhancement ratio of 2.56 using the short probing time data from 0 to 25 μs. Using a simple theoretical model which summed all the possible two-photon amplitudes for each comb pair and intermediate state we estimated the enhancement versus frequency offset. The theoretical enhancement is shown in Fig. (6.14), it has a peak value of 2.85 using the phase mask from Fig. (6.12) and the measured power spectrum from Fig. (6.4) with no diffraction loss. There are two peaks in the theory results corresponding to enhancement of the $5P_{1/2}$ transitions (larger peak), and offset by 120 GHz, the transitions through the $5P_{3/2}$ states are enhanced. We tried including diffraction loss to account for the dip below unity enhancement seen in our measurements at about 300 GHz, however this only reduced the peak enhancement ratio and did not change the characteristic shape significantly. As seen in our results for longer probing times from 0 to 500 μs the dip below unity is no longer present. The only difference that we can attribute this to is the radiation pressure Doppler shifting the atoms onto resonance from the $5S_{1/2}F=1$ state. Why this would change the characteristic shape of the enhancement versus frequency though is unknown.
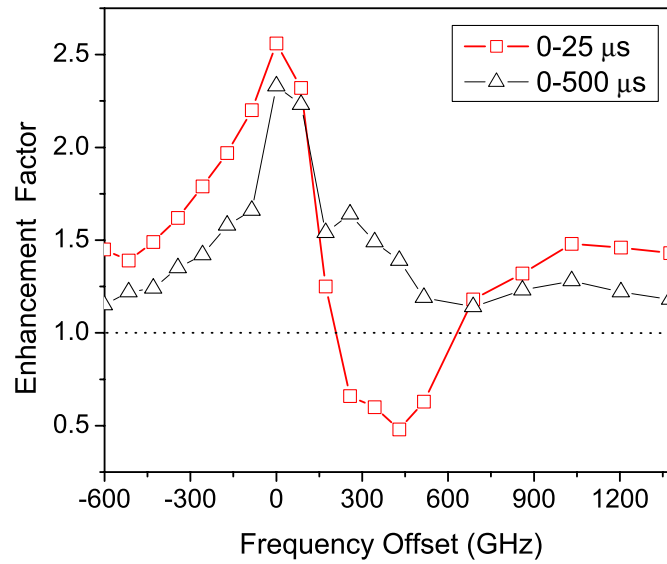
Figure 6.13: Measured signal enhancement ratio versus SLM position for short and long integration times. The x-axis is the frequency offset of the SLM pixels from some reference value.
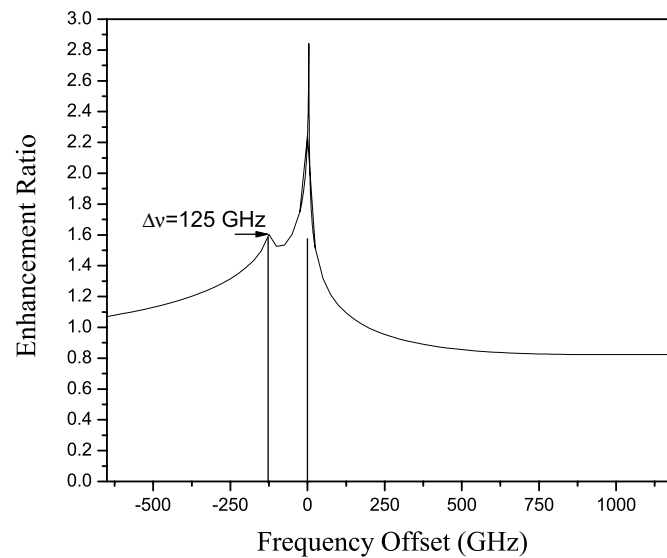

Figure 6.14: Theoretically predicted enhancement ratio assuming no diffraction loss using second-order perturbation theory.

In this experiment we have demonstrated the ability to increase the two-photon transition rate from $5S_{1/2}F=2$ to $5D_{3/2}F=1$. This was done by using a phase mask to force constructive interference between the two-photon amplitudes from comb modes pairs detuned from an intermediate state. Unlike the single pulse excitation we have the ability to select a specific excited hyperfine level, which in turn determines the possible intermediate states due to selection rules. In our experiment we must consider four possible intermediate states.

This type of coherent control can be extended much like the previous resonant experiment in section (6.2) to optimize the total two-photon transition rate with many intermediate states, for example in a molecule. One of the limitations of our experiment is the SLM pulse shaping resolution. To truly optimize the SLM phase mask for a specific transition would require the ability to control the phase of each individual comb mode. The ideal phase mask would compensate for the phase shift due to intermediate state detuning of each two-photon amplitude, which varies from 0° for a comb pair on intermediate resonance, to $\pm 90^o$ for pairs detuned $\pm f_r$ and further. Due to the limited per pixel resolution of our SLM pulse shaper, we are not able to make the phase of the amplitudes from mode pairs detuned from intermediate resonance the same as those that are resonant. Therefore with the phase mask used in this experiment the two-photon amplitude via only intermediate resonant transitions is 90° out of phase with the two-photon amplitudes from mode pairs detuned from intermediate resonance. For this reason future experiments of this type would benefit from using a pulse shaper with per-mode resolution, a feat that is already possible with high-repetition rate combs [105].

Chapter 7

Future Directions

In this thesis we have demonstrated the ability to use an optical frequency comb to conduct absolute frequency measurements. All of the transitions were excited directly by the frequency comb. Although the range of wavelengths used in our experiments was quite wide, $\sim$50 nm, it is possible to vastly extend the bandwidth of the comb.

Due to the extremely high peak intensities possible with a femtosecond laser it is well suited for non-linear frequency conversion. For example, the super-continuum generation in a micro-structured nonlinear fiber is a result of four-wave mixing. The super-continuum spectrum is far wider than the original Ti:Sapphire spectrum, recall we used two wavelengths separated by one octave for our f_o measurement. This is just one simple example of how the frequency comb spectrum may be extended for spectroscopic use at wavelengths that are difficult to reach with cw-lasers.

There has already been some experiments conducted using the principle of DFCS at very short wavelengths. Using traditional non-linear frequency conversion techniques the group of Eikema has conducted spectroscopy of two-photon transitions in krypton and xenon with a burst of up to six phase-coherent pulses. The first demonstration of this technique used two-photon absorption at 212 nm in krypton by a pair of phase coherent pulses [68]. The most recent example demon-

strates multi-pulse DFCS of the $5p^6$ $^1S_o \to 5p^5$ ($^2P_{3/2}$)$5d[\frac{1}{2}]_1$ transition in xenon at 125 nm, see reference [106]. The required VUV wavelengths were generated by first doubling a series of amplified Ti:Sapphire pulses in BBO, and subsequently tripling them in either oxygen or krypton. Using this technique the authors were able to scan f_r and recover a transition linewidth as narrow as 7.5 MHz FWHM after excitation by six pulses. One of the drawbacks of this technique is that only a limited number of pulses were generated, limiting the comb mode linewidths.

In an effort to extend the number of phase coherent pulses generated at very short wavelengths researchers in the group of Ye have turned to using high-harmonic generation. Instead of amplifying the phase-coherent pulse they are coupled into a broad-band optical cavity to increase the peak intensity. Within the cavity there are two spherical mirrors to focus the pulses into a xenon gas jet. In the intense peak electric field of the femtosecond pulses the xenon atoms undergo high-harmonic generation. Using this technique it was possible to generate wavelengths as short as 114 nm, and could in principle be extended to shorter wavelengths by increasing the peak intensity [107], also see reference [108]. We have published a theoretical study on the use of short wavelength optical combs for high-resolution two-photon helium spectroscopy [109]. An interesting proposal that is closely related to DFCS, is to Doppler cool atoms at traditionally hard to reach wavelengths using a femtosecond frequency comb [110].

In the context of coherent control we have mentioned the possibility of extending our technique to molecules. The idea is to combine pulse shaping with the comb, to enhance and control a Raman transition between a highly excited vibrational state and a deeply bound vibrational state. Instead of forcing the constructive interference between only a few intermediate states like in our research, we proposed to use many intermediate vibrational states [103]. On a more general note, the combination of very-broad-bandwidth frequency combs with the possi-

bility of line-by-line pulse shaping allows for very complicated coherent control experiments. I'm sure many imaginative experiments will utilize this technology in the future.

Bibliography

[1] D. J. Jones, S. A. Diddams, J. K. Ranka, A. Stentz, R. S. Windeler, J. L. Hall, and S. T. Cundiff, Carrier-envelope phase control of femtosecond mode-locked lasers and direct optical frequency synthesis, *Science* **288**, 635 (2000).

[2] S. A. Diddams, D. J. Jones, J. Ye, S. T. Cundiff, J. L. Hall, J. K. Ranka, R. S. Windeler, R. Holzwarth, T. Udem, and T. W. Hänsch, Direct link between microwave and optical frequencies with a 300 THz femtosecond laser comb, *Phys. Rev. Lett.* **84**, 5102 (2000).

[3] H. Schnatz, B. Lipphardt, J. Helmcke, F. Riehle, and G. Zinner, First Phase-Coherent Frequency Measurement of Visible Radiation, *Phys. Rev. Lett.* **76**, 18 (1996).

[4] J. L. Hall, Nodel lecture: Defining and measuring optical frequencies, *Rev. Mod. Phys.* **78**, 1279 (2006).

[5] T. W. Hänsch, Nobel lecture: Passion for precision, *Rev. Mod. Phys.* **78**, 1297 (2006).

[6] T. Udem, J. Reichert, R. Holzwarth, and T. W. Hänsch, Absolute opitcal frequency of the Cesium D-1 line with a mode-locked laser, *Phys. Rev. Lett.* **82**, 3568 (1999).

[7] L.-S. Chen and J. Ye, Extensive, high-resolution measurement of hyperfine interactions: Precise investigations of molecular potentials and wave functions, *Che. Phys. Lett.* **381**, 777 (2003).

[8] S. A. Diddams, T. Udem, J. C. B. E. A. Curtis, R. E. Drullinger, L. Hollberg, W. M. Itano, W. D. Lee, C. W. Oates, K. R. Vogel, and D. J. Wineland, An optical clock based on a single trapped ^{199}Hg$^+$ ion, *Science* **293**, 825 (2001).

[9] J. Ye, L. S. Ma, and J. L. Hall, Molecular Iodine Clock, *Phys. Rev. Lett.* **87**, 270801 (2001).

[10] A. D. Ludlow, T. Zelvinsky, G. K. Campbell, S. Blatt, M. M. Boyd, M. H. de Miranda, and M. J. Martin, Sr lattice clock at $1 \times 10(-16)$ fractional uncertainty by remote optical evaluation with a Ca clock, *Science* **319**, 1805 (2008).

[11] T. W. Hänsch, in *Tunable Lasers and Applications*, edited by A. Mooradian, T. Jaeger, and P. Stokseth (Springer-Verlag, New York, 1976), Chap. 8, p. 326.

[12] M. M. Salour and C. Cohen-Tannoudji, Observation of Ramsey's Interference Fringes in the Profile of Doppler-Free Two-Photon Resonances, *Phys. Rev. Lett.* **38**, 757 (1977).

[13] M. M. Salour, Quantum interference effects in two-photon spectroscopy, *Rev. Mod. Phys.* **50**, 667 (1978).

[14] R. Teets, J. Eckstein, and T. W. Hänsch, Coherent Two-Photon Excitation by Multiple Light Pulses, *Phys. Rev. Lett.* **38**, 760 (1977).

[15] J. N. Eckstein, A. I. Ferguson, and T. W. Hänsch, High-Resolution Two-Photon Spectroscopy with Picosecond Light Pulses, *Phys. Rev. Lett.* **40**, 847 (1978).

[16] M. J. Snadden, A. S. Bell, E. Riis, and A. I. Ferguson, Two-photon spectroscopy of laser-cooled Rb using a mode-lcoked laser, *Opt. Commun.* **125**, 70 (1996).

[17] J. Mlynek, W. Lange, H. Harde, and H. Burggraf, High-resolution coherence spectroscopy using pulse trains, *Phys. Rev. A* **24**, 1099 (1981).

[18] A. M. Weiner, D. E. Leaird, G. P. Wiederrecht, and K. A. Nelson, Femtosecond multiple-pulse impulsive stimulated Raman scattering spectroscopy, *J. Opt. Soc. Am. B* **8**, 1264 (1991).

[19] J. Ye and S. T. Cundiff, *Femtosecond optical frequency comb technology: Principle, Operation and Applications* (Springer, New York, 2005).

[20] M. C. Stowe, M. J. Thorpe, A. Pe'er, J. Ye, J. E. Stalnaker, V. Gerginov, and S. A. Diddams, in *Advances in Atomic, Molecular, and Optical Physics*, edited by E. Arimondo, P. R. berman, and C. C. Lin (Academic Press, London, 2008), Chap. 1, pp. 1–60.

[21] J. Reichert, R. holzwarth, T. Udem, and T. Hansch, Measuring the frequency of light with mode-locked lasers, *Opt. Comm.* **172**, 59 (1999).

[22] S. M. Foreman, Femtosecond Frequency Combs for Optical Clocks and Timing Transfer, Ph.D. thesis, University of Colorado, Boulder, Colorado, 2007.

[23] H. R. Telle, G. Steinmeyer, A. E. Dunlop, J. Stenger, D. H. Sutter, and U. Keller, Carrier-envelope offset phase control: A novel concept for absolute optical frequency measurement and ultrashort pulse generation, *App. Phys. B* **69**, 327 (1999).

[24] J. K. Ranka, R. S. Windeler, and A. J. Stenz, Visible continuum generation in air-silica microstructure optical fibers with anamolous dispersion at 800 nm, *Opt. Lett.* **25**, 25 (2000).

[25] J. M. Dudley, G. Genty, and S. Coen, Supercontinuum generation in photonic crystal fiber, *Rev. Mod. Phys.* **78**, 1135 (2006).

[26] A. Apolonski, A. Poppe, G. Tempea, C. Spielmann, T. Udem, T. Holzwarth, T. W. Hansch, and F. Krausz, Controlling the phase evolution of few-cycle light pulses, *Phys. Rev. Lett.* **85**, 740 (2000).

[27] T. M. Fortier, D. J. Jones, and S. T. Cundiff, Phase stabilization of an octave-spanning Ti:sapphire laser, *Opt. Lett.* **28**, 2198 (2003).

[28] T. M. Ramond, S. A. Diddams, and L. Holberg, Phase-coherent link from optical to microwave frequencies by means of the broadband continuum from a 1-GHz Ti:sapphire femtosecond oscillator, *Opt. Lett.* **27**, 1842 (2002).

[29] K. W. Holman, R. J. Jones, A. Marian, S. T. Cundiff, and J. Ye, Intensity-related dynamics of femtosecond frequency combs, *Opt. Lett.* **28**, 851 (2003).

[30] H. J. Metcalf, *Laser Cooling and Trapping* (Springer, New York, 1999).

[31] C. Wieman, G. Flowers, and S. Gilbert, Inexpensive laser cooling and trapping experiment for undergraduate laboratories, *Am. J. of Phys.* **63**, 317 (1995).

[32] J. Dalibard and C. Cohen-Tannoudji, Atomic motion in laser light: connection between semiclassical and quantum descriptions, *J. Phys. B: At. Mol. Phys.* **18**, 1661 (1985).

[33] R. J. Cook, Atomic motion in resonant radiation: An application of Ehrenfest's theorem, *Phys. Rev. A* **20**, 224 (1979).

[34] C. Gabbanini, A. Evangelista, S. Gozzini, A. Lucchesini, A. Fioretti, J. M. Muller, M. Colla, and E. Arimondo, Scaling laws in magneto-optical traps, *Euro. Phys. Lett.* **37**, 251 (1997).

[35] X. Xu, T. H. Loftus, M. J. Smith, J. L. Hall, A. Gallagher, and J. Ye, Dynamics in a two-level atom magneto-optical trap, *Phys. Rev. A* **66**, 011401(R) (2002).

[36] C. Monroe, W. Swann, H. Robinson, and C. Wieman, Very cold trapped atoms in a vapor cell, *Phys. Rev. Lett.* **65**, 1571 (1990).

[37] A. Marian, Direct Frequency Comb Spectroscopy For Optical Frequency Metrology and Coherent Interactions, Ph.D. thesis, University of Colorado, Boulder, Colorado, 2005.

[38] C. E. Wieman and L. Hollberg, Using diode lasers for atomic physics, *Rev. Sci. Inst.* **62**, 1 (1991).

[39] K. B. MacAdam, A. Steinbach, and C. Wieman, A narrow-band tunable diode laser system with grating feedback, and a saturated absorption spectrometer for Cs and Rb, *Am. J. Phys.* **60**, 1098 (1992).

[40] G. C. Bjorklund, Frequency-moulation spectroscopy: a new method for measuring weak absorptions and dispersions, *Opt. Lett.* **5**, 15 (1980).

[41] J. L. Hall, L. Hollberg, T. Baer, and H. G. Robinson, Optical heterodyne saturation spectroscopy, *Appl. Phys. Lett.* **39**, 680 (1981).

[42] J. Dalibard and C. Cohen-Tannoudji, Laser cooling below the Doppler limit by polarization gradients: simple theoretical models, *J. Opt. Soc. Am. B* **6**, 2023 (1989).

[43] P. D. Lett, R. N. Watts, C. I. Westbrook, W. D. Phillips, P. L. Gould, and H. J. Metcalf, Observation of atoms laser cooled below the Doppler limit, *Phys. Rev. Lett.* **61**, 169 (1988).

[44] P. D. Lett, W. D. Phillips, S. L. Rolston, C. E. Tanner, R. N. Watts, and C. I. Westbrook, Optical molasses, *J. Opt. Soc. Am. B* **6**, 2084 (1989).

[45] L. W. Casperson, Few-cycle pulses in two-level media, *Phys. Rev. A* **57**, 609 (1998).

[46] G. M. Genkin, Rabi frequency and nonlinearity of a two-level atom for a ultrashort optical pulse, *Phys. Rev. A* **58**, 758 (1998).

[47] R. W. Ziolkowski, J. M. Arnold, and D. M. Gogny, Ultrafast pulse interactions with two-level atoms, *Phys. Rev. A* **52**, 3082 (1995).

[48] S. Hughes, Breakdown of the Area Theorem: Carrier-Wave Rabi Flopping of Femtosecond Optical Pulses, *Phys. Rev. lett.* **81**, 3363 (1998).

[49] N. V. Vitanov and P. L. Knight, Coherent excitation of a two-state system by a train of short pulses, *Phys. Rev. A* **52**, 2245 (1995).

[50] P. T. Greenland, Resonances excited by a train of delta function pulses, *J. Phys. B: At. Mol. Phys.* **16**, 2515 (1983).

[51] R. G. Brewer and E. L. Hahn, Coherent two-photon processes: Transient and steady-state cases, *Phys. Rev. A* **11**, 1641 (1975).

[52] N. V. Vitanov, Analytic model of a three-state system driven by two laser pulses on two-photon resonance, *J. Phys. B: Mol. Opt. Phys.* **31**, 709 (1998).

[53] C. E. Carroll and F. T. Hioe, Three-state model driven by two laser beams, *Phys. Rev. A* **36**, 724 (1987).

[54] R. Loudon, *The quantum theory of light* (Clarendon Press, Oxford, 1973).

[55] T. H. Yoon, A. Marian, J. L. Hall, and J. Ye, Phase-coherent multilevel two-photon transitions in cold Rb atoms: Ultrahigh-resolution spectroscopy via frequency-stabilized femtosecond laser, *Phys. Rev. A* **63**, 011402(R) (2000).

[56] S. Chang and V. Minogin, Density-matrix approach to dynamics of multi-level atoms in laser fields, *Phys. Rep.* **365**, 65 (2002).

[57] R. W. Boyd, *Nonlinear Optics* (Academic Press, San Diego, 2003).

[58] P. Balling, D. J. Maas, and L. D. Noordam, Interference in climbing a quantum ladder system with frequency-chirped laser pulses, *Phys. Rev. A* **50**, 4276 (1994).

[59] J. Dalibard, Y. Castin, and K. Molmer, Wave-Function Approach to Dissipative Processes in Quantum Optics, *Phys. Rev. Lett.* **68**, 580 (1992).

[60] D. Felinto, L. H. Acioli, and S. S. Vianna, Accumulative effect in the coherence of three-level atoms excited by femtosecond-laser frequency combs, *Phys. Rev. A* **70**, 043403 (2004).

[61] U. Voltz and H. Schmoranzer, Precision Lifetime Measurements on Alkali Atoms and on Helium by Beam-Gas-Laser Spectroscopy, *Phys. Scripta* **T65**, 48 (1996).

[62] B. R. Bulos, R. Gupta, and W. Happer, Lifetime measurements in the excited S states of K, Rb, and Cs by the cascade Hanle effect, *J. Opt. Soc. Am.* **66**, 426 (1976).

[63] A. D. Ludlow, X. Huang, M. Notcutt, T. Zanon-Willette, S. M. Foreman, M. M. Boyd, S. Blatt, and J. Ye, Compact, thermal-noise-limited optical cavity for diode laser stabilization at 1×10^{-15}, *Opt. Lett.* **32**, 641 (2007).

[64] S. A. Diddams, L. Hollberg, L. S. Ma, and L. Robertsson, Femtosecond-laser-based optical clockwork with instability $\leq 6.3 \times10^{-16}$ in 1 s, *Opt. Lett.* **27**, 58 (2002).

[65] P. F. Liao and J. E. Bjorkholm, Direct observation of atomic energy level shifts in two-photon absorption, *Phys. Rev. Lett.* **34**, 1 (1975).

[66] M. S. Ko and Y. W. Liu, Observation of the $5S_{1/2}$ - $7S_{1/2}$ two-photon transitions with a diode laser, *Opt. Lett.* **29**, 1799 (2004).

[67] R. Holzwarth *et al.*, Absolute frequency measurement of iodine lines with a femtosecond optical synthesizer, *Appl. Phys. B* **73**, 269 (2001).

[68] S. Witte, R. T. Zinkstok, W. Ubachs, W. Hogervorst, and K. S. E. Eikema, Deep-Ultraviolet quantum interference metrology with ultrashort laser pulses, *Science* **307**, 400 (2005).

[69] F. Nez, F. Biraben, R. Felder, and Y. Millerioux, Optical frequency determination of the hyperfine components of the $5S_{1/2}$ - $5D_{3/2}$ two-photon transitions in Rubidium, *Opt. Commun.* **102**, 432 (1993).

[70] H. C. Chui, M. S. Ko, Y. W. Liu, J. T. Shy, J. L. Peng, and H. Ahn, Absolute frequency measurement of rubidium 5S7S two-photon transitions with a femtosecond laser comb, *Opt. Lett.* **30**, 842 (2005).

[71] H. T. Duong, S. Liberman, J. Pinard, and J. L. Vialle, Measurement of the hyperfine structure of the $5^2S_{1/2}$ state of ^{23}Na by two-step excitation using two cw dye lasers, *Phys. Rev. Lett.* **33**, 339 (1974).

[72] B. Cagnac, G. Grynberg, and F. Biraben, Spectroscopie D'absorption multiphotonique sans effet doppler, *Journal de Physique* **34**, 845 (1973).

[73] J. Ye, S. Swartz, P. Junger, and J. L. Hall, Hyperfine structure and absolute frequency of the ^{87}Rb $5P_{3/2}$ state, *Opt. Lett.* **21**, 1280 (1996).

[74] G. P. Barwood, P. Gill, and W. R. C. Rowley, Frequency Measurement on Optically Narrowed Rb-Stabilised Laser Diodes at 780 nm and 795 nm, *Appl. Phys. B* **53**, 142 (1991).

[75] E. B. Treacy, Optical Pulse Compression With Diffraction Gratings, *IEEE J. Quantum Elec.* **QE-5**, 454 (1969).

[76] O. E. Martinez, 3000 Times Grating Compressor with Positive Group Velocity Dispersion: Application to Fiber Compensation in 1.3-1.6μm Region, *IEEE J. Quantum Elec.* **QE-23**, 59 (1987).

[77] D. Strickland and G. Mourou, Compression of amplified chirped optical pulses, *Opt. Commun.* **56**, 219 (1985).

[78] O. E. Martinez, J. P. Gordon, and R. L. Fork, Negative group-velocity dispersion using refraction, *J. Opt. Soc. Am. A* **1**, 1003 (1984).

[79] O. E. Martinez, Grating and prism compressors in the case of finite beam size, *J. Opt. Soc. Am. B* **3**, 929 (1986).

[80] K. Varju, A. P. Kovacs, K. Osvay, and G. Kurdi, Angular dispersion of femtosecond pulses in a Gaussian beam, *Opt. Lett.* **27**, 2034 (2002).

[81] K. Osvay, A. P. Kovacs, Z. Heiner, G. Kurdi, J. Klebniczki, and M. Csatari, Angular Dispersion and Temporal Change of Femtosecond Pulses From Misaligned Pulse Compressors, *IEEE J. Sel. Top. Quant.* **10**, 213 (2004).

[82] S. Chelkowski, A. D. Bandrauk, and P. B. Corkum, Efficient Molecular Dissociation by a Chirped Ultrashort Infrared Laser Pulse, *Phys. Rev. Lett.* **65**, 2355 (1990).

[83] J. S. Mellinger, S. R. Gandhi, A. Hariharan, J. X. Tull, and W. S. Warren, Generation of narrowband inversion with broadband laser pulses, *Phys. Rev. Lett.* **68**, 2000 (1992).

[84] D. Oron, N. Dudovich, D. Yelin, and Y. Silberberg, Narrow-Band Coherent Anti-Stokes Raman Signals from Broad-Band Pulses, *Phys. Rev. Lett.* **88**, 063004 (2002).

[85] B. W. Shore, K. Bergmann, A. Kuhn, S. Schiemann, J. Oreg, and J. H. Eberly, Laser-induced population transfer in multistate systems: A comparative study, *Phys. Rev. A* **45**, 5297 (1992).

[86] J. R. Kuklinski, U. Gaubatz, F. T. Hioe, and K. Bergmann, Adiabatic population transfer in a three-level system driven by delayed laser pulses, *Phys. Rev. A* **40**, 6741 (1989).

[87] B. Broers, H. B. van Linden van den Heuvell, and L. D. Noordam, Efficient population transfer in a three-level ladder system by frequency-swept ultrashort laser pulses, *Phys. Rev. Lett.* **69**, 2062 (1992).

[88] B. Chatel, J. Degert, S. Stock, and B. Girard, Competition between sequential and direct paths in a two-photon transition, *Phys. Rev. A* **68**, 041402(R) (2003).

[89] B. Chatel, J. Degert, and B. Girard, Role of quadratic and cubic spectral phases in ladder climbing with ultrashort pulses, *Phys. Rev. A* **70**, 053414 (2004).

[90] E. A. Korsunsky and D. V. Kosachiov, Phase-dependant nonlinear optics with double-Λ atoms, *Phys. Rev. A* **60**, 4996 (1999).

[91] D. V. Kosachiov, B. G. Matisov, and Y. V. Rozhdestvensky, Coherent phenomena in multilevel systems with closed interaction countour, *J. Phys. B-At. Mol. Opt.* **25**, 2473 (1992).

[92] G. Morigi, S. Franke-Arnold, and G. Oppo, Phase-dependant interaction in a four-level atomic configuration, *Phys. Rev. A* **66**, 053409 (2002).

[93] S. J. Buckle, S. M. Barnett, P. L. Knight, M. A. Lauder, and D. T. Pegg, Atomic interferometers: Phase-dependence in multilevel atomic transitions, *Opt. Acta.* **33**, 1129 (1986).

[94] M. D. Lukin, S. F. Yelin, M. Fleischauer, and M. O. Scully, Quantum interference effects induced by interacting dark resonances, *Phys. Rev. A* **60**, 3225 (1999).

[95] X. Yan, H. Qiong-Yi, G. C. LaRocca, M. Artoni, X. Ji-Hua, and G. Jin-Yue, Dynamic control of four-wave-mixing enhancement in coherently driven four-level atoms, *Phys. Rev. A* **73**, 013816 (2006).

[96] H. Shpaisman, A. D. Wilson-Gordon, and H. Friedmann, Efficient parametric amplification in double-Λ systems without maximal two-photon coherence, *Phys. Rev. A* **70**, 063814 (2004).

[97] O. Kocharovskaya and P. Mandel, Amplification without inversion: The double-Λ scheme, *Phys. Rev. A* **42**, 523 (1990).

[98] E. S. Fry, M. D. Lukin, T. Walther, and G. R. Welch, Four-level atomic coherence and cw VUV lasers, *Opt. Comm.* **179**, 499 (2000).

[99] S. M. Gallagher and D. M. Jonas, Phase-resolved time-domain nonlinear optical signals, *Phys. Rev. A* **62**, 033820 (2000).

[100] Z. Chen, P. Brumer, and M. Shapiro, Multiproduct coherent control of photodissociation via two-photon versus two-photon interference, *J. Chem. Phys.* **98**, 6843 (1993).

[101] W. Maichen, F. Renzoni, I. Mazets, E. Korsunsky, and L. Windholz, Transient coherent population trapping in a closed loop interaction scheme, *Phys. Rev. A* **53**, 3444 (1996).

[102] A. F. Huss, R. Lammegger, C. Neureiter, E. A. Korsunsky, and L. Windholz, Phase Correlation of Laser Waves with Arbitrary Frequency Spacing, *Phys. Rev. Lett.* **93**, 223601 (2004).

[103] A. Pe'er, E. A. Shapiro, M. C. Stowe, M. Shapiro, and J. Ye, Precise control of molecular dynamics with a femtosecond frequency comb, *Phys. Rev. Lett.* **98**, 113004 (2007).

[104] N. Dudovich, B. Dayan, S. G. Faeder, and Y. Silberberg, Transform-limited pulses Are Not Optimal for Resonant Multiphoton Transitions, *Phys. Rev. Lett.* **86**, 47 (2001).

[105] Z. Jiang, D. E. Leaird, C. Huang, H. Miao, M. Kourogi, K. Imai, and A. M. Weiner, Spectral Line-by-Line Pulse Shaping on an Optical Frequency Comb Generator, *IEEE J. Quantum Elec.* **43**, 1163 (2007).

[106] R. T. Zinkstok, S. Witte, W. Ubachs, W. Hogervorst, and K. S. E. Eikema, Frequency comb laser spectroscopy in the vacuum-ultraviolet region, *Phys. Rev. A* **73**, 061801 (2006).

[107] R. J. Jones, K. D. Moll, M. J. Thorpe, and J. Ye, Phase-Coherent Frequency Combs in the Vacuum Ultraviolet via High-Harmonic Generation inside a Femtosecond Enhancement Cavity, *Phys. Rev. Lett.* **94**, 193201 (2005).

[108] C. Gohle, T. Udem, M. Hermann, J. Rauschenberger, R. Holzwarth, H. A. Schuessler, and F. Krausz, A frequency comb in the extreme ultraviolet, *Nature* **436**, 234 (2005).

[109] E. E. Eyler, D. E. Chieda, M. C. Stowe, M. J. Thorpe, T. R. Schibli, and J. Ye, Prospects for precision measurements of atomic helium using direct frequency comb spectroscopy, *Eur. Phys. J. D* **10**, 1140 (2007).

[110] D. Kielpinski, Laser cooling of atoms and molecules with ultrafast pulses, *Phys. Rev. A* **73**, 063407 (2006).